Dynamics of Electronic Transport in Spatially-extended Systems with Negative Differential Conductivity

by

Huidong Xu

Department of Physics
Duke University

Date: ____________________

Approved:

____
Stephen Teitsworth, Advisor

____
Harold Baranger

____
Steffen Bass

____
Daniel Gauthier

____
Adrienne Stiff-Roberts

Dissertation submitted in partial fulfillment of the requirements for the degree of
Doctor of Philosophy in the Department of Physics
in the Graduate School of Duke University
2010

Abstract

(Condensed Matter)

Dynamics of Electronic Transport in Spatially-extended Systems with Negative Differential Conductivity

by

Huidong Xu

Department of Physics
Duke University

Date: ____________________

Approved:

____
Stephen Teitsworth, Advisor

____
Harold Baranger

____
Steffen Bass

____
Daniel Gauthier

____
Adrienne Stiff-Roberts

An abstract of a dissertation submitted in partial fulfillment of the requirements for
the degree of Doctor of Philosophy in the Department of Physics
in the Graduate School of Duke University
2010

Copyright © 2010 by Huidong Xu
All rights reserved except the rights granted by the
Creative Commons Attribution-Noncommercial Licence

Abstract

Negative differential conductivity (NDC) is a nonlinear property of electronic transport for high electric field strength found in materials and devices such as semiconductor superlattices, bulk GaAs and Gunn diodes. In spatially extended systems, NDC can cause rich dynamics such as static and mobile field domains and moving charge fronts. In this thesis, these phenomena are studied theoretically and numerically for semiconductor superlattices. Two classes of models are considered: a discrete model based on sequential resonant tunneling between neighboring quantum wells is used to described charge transport in weakly-coupled superlattices, and a continuum model based on the miniband transport is used to describe charge transport strongly-coupled superlattices.

The superlattice is a spatially extended nonlinear system consisting a periodic arrangement of quantum wells (e.g., GaAs) and barriers (e.g., AlAs). Using a discrete model and only considering one spatial dimension, we find that the boundary condition at the injecting contact has a great influence on the dynamical behavior for both fixed voltage and transient response. Static or moving field domains are usually inevitable in this system. In order to suppress field domains, we add a side shunting layer parallel to the growth direction of the superlattice. In this case, the model includes both vertical and lateral spatial degrees of freedom. We first study a shunted weakly-coupled superlattice for a wide range of material parameters. The field domains are found to be suppressed for superlattices with small lateral size and good connection between the shunt and the quantum wells of the superlattice. As the lateral size of the superlattice increases, the uniform field configuration loses its stability to either static or dynamic field domains, regardless of shunt properties. A lower quality shunt generally leads to regular and chaotic current oscillations and complex spatio-temporal dynamics in the field profile. Bifurcations separating static and dynamic behaviors are characterized and found to be dependent on the shunt properties. Then we adopt the model to study the shunted strongly-coupled superlattice with the continuum model. Key structural parameters associated with both the shunt layer and SL are identified for which the shunt layer stabilizes a uniform electric field profile. These results support the possibility to realize a SL-based THz oscillator with a carefully designed structure.

Another important behavior of the static field domains in the weakly-coupled superlattice is bistability, i.e., two possible states (i.e., electric field configurations) for a single voltage. Noise can drive the system from one of these states (the metastable state) to the other one (the globally stable state). The process of escape from the metastable state can be viewed as a stochastic first-passage process in a high-dimensional system that possesses complex stability eigenvalues and for which a global potential energy function does not exist. This process is simulated using a stochastic differential equation system which incorporates shot noise. The mean switching time τ is fitted to an exponential expression $e^{\frac{1}{D}(V_{\mathrm{th}}-V)^{\alpha}}$, where V_{th} denotes the voltage at the end of the current branch. The exponent α in the fitting curve deviates from 1.5 which is predicted for a generic one dimensional system. We develop an algorithm to determine an effective locally valid potential. Principal component analysis is applied to find the most probable path for switching from the metastable current state.

Contents

Abstract **iv**

List of Tables **x**

List of Figures **xi**

Acknowledgements **xv**

1 Introduction **1**

2 Vertical electronic transport in superlattices **8**

2.1 Electronic transport in nanostructures 8

2.2 The semiconductor superlattice 11

2.3 Electronic states in superlattices 12

2.4 Electronic transport in superlattices 15

2.5 The sequential tunneling model for weakly-coupled superlattices . . . 17

2.6 Miniband transport 24

2.6.1 Gain 27

3 Dependence of front dynamics on contact conductivity in weakly-coupled superlattices **30**

3.1 The model for one-dimensional superlattices 31

3.2 Contact conductivity vs. doping density 32

3.3 Dependence of time-averaged $I-V$ curves on contact conductivity . 35

3.3.1 Current branches and field domains at high σ 36

3.3.2 Current self-oscillation 38

3.3.3 Extremely low σ 41

3.4 Dependence of Relocation Type on contact conductivity and Voltage Step 44

3.5 Conclusion 53

4 The weakly-coupled superlattice with a shunting side layer 54

4.1 Laterally extended model of the superlattice with shunt layer 55

4.1.1 The laterally extended model for superlattice 55

4.1.2 The shunt 58

4.1.3 Connectivity 60

4.1.4 Doping density in the shunt 61

4.1.5 The total current 62

4.2 Parameters and Time scales 63

4.3 Numerical method 65

4.4 Dependence of shunting dynamics on the lateral size of the Superlattice 66

4.4.1 High quality shunting layer with small L_x 67

4.4.2 High quality shunting layer with large L_x 70

4.5 Dependence of dynamical behavior on the shunt properties 76

4.5.1 Dynamical behavior vs. connectivity parameter a for large contact conductivity 77

4.5.2 Dynamical behavior for small contact conductivity 86

4.5.3 Dynamical behavior vs. shunt conductivity parameter b 87

4.6 Conclusion 88

5 The superlattice-based THz oscillator 90

5.1 Overview 91

5.2 The shunted strongly-coupled superlattice model 93

5.3 Results 97
5.4 Discussion 100

6 Stochastic switching in weakly-coupled superlattices 102

6.1 Stochastic switching between bistable states 102
    6.1.1 Background and the Wiener process 103
    6.1.2 Langevin equation 104
    6.1.3 Fokker-Planck equation 105
    6.1.4 First passage time for a double well potential 106
    6.1.5 Saddle node bifurcation 109
6.2 Sequential tunneling model with shot noise 110
    6.2.1 Fluctuation due to single noise sources 113
6.3 Scaling behavior of the lifetime of the metastable state 113
    6.3.1 Switching time distribution 113
    6.3.2 3/2 scaling law 117
    6.3.3 The statistical model 119
    6.3.4 Bayesian nonlinear curve fitting 120
6.4 Projection onto saddle-node trajectory 126
6.5 Analysis of the ensemble 130
    6.5.1 Multivariate statistics 132
    6.5.2 Introduction to PCA 136
    6.5.3 Results 137

7 The tunnel diode model 143

7.1 The tunnel diode circuit 143
7.2 The tunnel diode model 146
7.3 Results 150

7.3.1 Current branches 150

7.3.2 Field inhomogeneity parameter 153

7.4 Connection between the weakly-coupled superlattice and the tunnel diode array 160

7.5 Conclusion 162

8 Summary **164**

Bibliography **168**

Biography **178**

List of Tables

2.1 GaAs and AlAs parameters 12

3.1 Doping density values equivalent to contact conductivity σ values. . . 35

4.1 Parameters used for the shunted weakly-coupled superlattice. 63

5.1 Parameters used for the shunted strongly-coupled superlattice. 97

List of Figures

1.1 Schematic of NDC 4

2.1 Schematic of the superlattice 13

2.2 The Kronig-Penney model 15

2.3 Different approaches for electronic transport in superlattices 16

2.4 Sequential tunneling current density 22

2.5 Schematic of energy and velocity versus Bloch vector. 25

2.6 $J-F$ characteristics for miniband transport. 28

2.7 Real part of conductivity 28

3.1 Contact current characteristics 34

3.2 Effective contact conductivity versus N_c. 34

3.3 Time-averaged $I-V$ curves for different σ values. 37

3.4 Field domains. 39

3.5 Current oscillations for $\sigma = 0.016(\Omega\mathrm{m})^{-1}$. 40

3.6 Field and charge density profile for $\sigma = 0.00168(\Omega\mathrm{m})^{-1}$. 43

3.7 Initial and final voltages for switching. 44

3.8 Injected dipole relocation mechanism 46

3.9 Shortened injected dipole relocation mechanism 47

3.10 Single monopole shift 48

3.11 Injected monopole relocation mechanism 50

3.12 Measured current response for large voltage step switching 51

3.13 Dependence of relocation time on V_{step} and σ. 52
4.1 Schematic of the shunted superlattice 56
4.2 Evolution of a shunted superlattice with $L_x = 20$ μm 68
4.3 The steady state for a shunted superlattice with $L_x = 20$ μm 69
4.4 Steady states for shunted superlattices with $L_x = 160$ μm and 640 μm 71
4.5 Evolution of a shunted superlattice with $L_x = 0.8$ mm 72
4.6 Evolution of a shunted superlattice with $L_x = 1.28$ mm 73
4.7 Evolution of a shunted superlattice with $L_x = 2.56$ mm 74
4.8 Evolution of a shunted superlattice with $L_x = 5.12$ mm 75
4.9 Bifurcation for $\sigma = 0.04$ $(\Omega\text{m})^{-1}$, $L_x = 20$ μm 78
4.10 Evolution of a shunted superlattice with $L_x = 20$ μm, $a = 1.00 \times 10^{-3}$ and $U = 1.46$ V 80
4.11 Subcritical Hopf bifurcation at point A_l 82
4.12 Saddle node bifurcation of limit cycles at point A_u 83
4.13 SNIPER bifurcation at point B 84
4.14 Chaotic oscillations 85
4.15 Bifurcation for $\sigma = 0.016$ $(\Omega\text{m})^{-1}$ 87
5.1 Schematic of the shunted strongly-coupled superlattice. 94
5.2 Snapshots for Structure 1, 2 and 3 99
5.3 Snapshots for Structure 4, 5 and 6 100
5.4 The energy band lineups of the 6.1 Å family semiconductor.[102] . . . 101
6.1 Double well potential 108
6.2 Illustration of saddle node bifurcation. 109
6.3 Fluctuation due to single noise sources 114
6.4 Stochastic switching between bistable states 115
6.5 Switching time distribution at $V = 0.5388$ V 115

6.6 Switching time distributions at other V values 117

6.7 Schematic of the potential for the saddle-node bifurcation 119

6.8 Mean switching time vs. applied voltage using pulsed scheme. 120

6.9 The posterior distributions for pulsed scheme by direct integration . . 123

6.10 Mean switching time for metastable scheme. 123

6.11 The posterior distributions for metastable scheme by direct integration 124

6.12 Mean switching time for metastable scheme with more data points. . 125

6.13 The posterior distributions for metastable scheme with nine points by direct integration 125

6.14 The marginal posterior distributions for metastable scheme with nine points by direct integration 126

6.15 Eigenvalue spectrum and eigenvectors of the Jacobian matrix 128

6.16 Effective potential 130

6.17 Operation points at $V = 0.539$V (left) and 0.47V (right) 131

6.18 Histogram of F_{36}, F_{37} 131

6.19 Most probable path 132

6.20 Alignment of the switching processes. 133

6.21 The two time windows to apply PCA. 138

6.22 The first principal components at t_1 and t_2 139

6.23 The first principal components for sub-ensembles 139

6.24 Histogram of the first and the second z-scores at t_2 140

6.25 Histogram of the first z-scores at t_1 140

6.26 Latents 141

6.27 Variance of F_i 141

6.28 pc of correlation matrix 142

7.1 Band diagram for tunnel diodes under different bias. 144

7.2 Schematic of circuit measuring $I-V$ curve of tunnel diode. 145

7.3 The $I-V$ curve of tunnel diode 145

7.4 Circuit of tunnel diode array 146

7.5 Measured $I-V$ curve of eight tunnel diode connected in series. 147

7.6 Coupling mechanism of the tunnel diode circuit model 150

7.7 $I-V$ curve of eight tunnel diode model 151

7.8 Voltage evolution of each element in the eight tunnel diode model . . 152

7.9 $I-V$ curve and voltage distribution for different ramping speed. . . . 155

7.10 The field inhomogeneity parameter r_{max}. 157

7.11 Circuit schematic of a circuit based on tunnel diodes to simulate the superlattice. 162

Acknowledgements

This thesis would not have been possible without the help of other people. First, I want to thank my advisor Prof. Stephen Teitsworth for his guidance, constant enthusiastic support of my ideas and helpful discussions.

In dealing with the shunted superlattices, the model is based on a laterally extended superlattice model developed by Dr. Andreas Amann who kindly offered his code. The discussions with my co-authors Andreas and Prof. Eckehard Schöll lead to a full story of the shunted weakly-coupled superlattices.

The stochastic switching part is also a project for my master's thesis in statistics, which is supervised by Prof. Scott Schmidler who guided me in statistical techniques that are not familiar to most physicists.

In my work on contact conductivity effects on superlattice dynamics, I would like to thank helpful discussions with Prof. Luis Bonilla and Dr. Ramon Escobedo.

I also want to acknowledge Dr. Yuriy Bomze for his experimental work whose results confirm some of my theoretical predictions. Those superlattice samples were grown by Prof. Holger Grahn and Rudolf Hey at the Paul-Drude-Institute.

Dr. Matthias Heymann of the group of Prof. Jonathan Mattingly tackled the switching time problem using another approach. The discussion with them provided another perspective to the problem.

I also thank my PhD committee (Prof. Harold Baranger, Steffen Bass, Daniel Gauthier, Adrienne Stiff-Roberts and Stephen Teitsworth) for their support and advice.

Lastly, I want to thank my parents who know nothing about physics, but provided me with infinite support and encouragement. I dedicate this thesis to them.

1

Introduction

Nonequilibrium dissipative systems, which constitute an important subset of complex systems, have been attracting increased attention in the past several years. Nonequilibrium states of a dissipative system can only be maintained by a continuous flux of energy and possibly matter. The dissipation of energy leads to the shrinkage of volume of a set of state points in the phase space - the space of dynamical variables that describes the state of the system. In contrast, the volume of a set of state points of a Hamiltonian system is conserved.

The inherent nonlinear properties of these systems often cause them to display complex spatio-temporal structures when they are driven, also known as pattern formation[1]. A famous example of pattern formation is provided by the Belousov-Zhabotinsky (BZ) reaction. This family of chemical reactions not only can show oscillation in time but also develops rich spatial patterns such as stationary waves, moving fronts and spiral waves[2]. Systems like the BZ reaction give rise to the concept of an excitable medium, which has the capability of propagating some kind of nonlinear wave excitation. Other examples of pattern forming systems are fluid convection[3], combustion[4], turbulence[5], signal transmission in nerves[6], vegetation fronts in ecological system[7] and galaxy formation in the universe[1].

Pattern formation is a *self-organization* phenomenon, which does not fall under the purview of the second law of thermodynamics. In other words, the emergent patterns are typically not understood as a manifestation of a maximum entropy state. Self-organization is a feature of complex systems which are composed of interconnected parts, but the behavior of complex systems is not obvious from the individual composing parts. Other interesting phenomena emerge from complex systems, such as self-organized criticality[8] and synchronization[9, 10]. More recently, the study of complex systems has reached the areas of biology and social science. Specific examples include genetic networks[11], neural networks[11] and social networks[12].

Although great efforts have been made to develop general theories about nonequilibrium dissipative systems[13, 14], a unifying theory still does not exist. Understanding these systems is critical to answer many fundamental questions in fields as diverse as biology, social sciences and physical sciences. So this is a very important area of scientific inquiry for which the methods of equilibrium statistical mechanics can not provide an adequate explanation, and a lot of research is currently focused on such problems.

Semiconductors may be considered as nonequilibrium dissipative systems when they are driven electrically and/or optically far from equilibrium. Nonlinear electronic transport in semiconductors often results in rich dynamics and self-organization as the Ohm's Law breaks down under high electric field. The development of semiconductor science and technology over the last sixty years has not only brought us a myriad of devices that significantly revolutionized our lives, but also provided us excellent systems to study nonequilibrium phenomena. Some remarkable features of semiconductors are: 1) High-quality materials. The most important semiconductors, silicon and gallium arsenide, are made with astonishing structural and compositional perfections, i.e., low defect densities and great control over impurity doping profiles. These perfections are achieved not only in bulk material, but also at interfaces where different materials meet. 2) Precise fabrication. Semiconductor can be grown with precision of a single atomic layer and patterned with sub-micro resolution. 3) Simplicity. The microscopic complication of materials can be greatly simplified by treating the carriers and the media with effective parameters such as effective mass and dielectric constants. 4) Sensitivity. The dynamics in semiconductors is sensitive to changes of material and structure parameters and external driving forces. These features make semiconductors robust and ideal to study nonequilibrium phenomena.

From the semiclassical perspective, the state of a semiconductor can be described by space and time dependent density of charge carriers and local electric field. The dynamics of carrier transport is largely determined by the current density j as a function of local electric field E, the $J-E$ curve, which is the constitutive relation of the media. In most cases, when the electric field is low, the current density increases as the electric field strength increases linearly(Ohm's Law). However, as the electric field increases, deviations from this linear behavior inevitably occur. In certain special materials or structures, the current density may actually decrease as electric field strength increases for high field intensity. This nonlinear phenomenon is called negative differential conductivity (NDC). There are two major categories of NDC[15]: S-shaped NDC (SNDC) and N-shaped NDC (NNDC), shown in Fig 1.1. Negative differential conductivity, a simple nonlinear local property usually causes spatio-temporal instability in semiconductors as systems driven far from equilibrium. The S-shaped NDC typically causes current filaments, an inhomogeneity in the current density distribution lateral to the direction of the current flow. Examples of systems that exhibit SNDC are heterostructure hot-electron diodes (HHED)[16] and certain types of double barrier resonant tunneling (DBRT) diodes[17]. The N-shaped NDC is often associated with field domains and charge accumulation and depletion fronts. In this thesis, we will mainly study NNDC in superlattices (SLs). Examples of systems

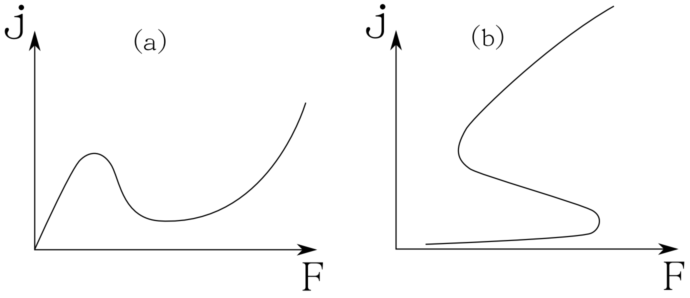

Figure 1.1: Schematic of negative differential conductivity (NDC): The current density j versus the electric field F for (a) NNDC and (b) SNDC.

that have the NNDC property are tunnel diodes, Gunn diodes and superlattices.

The tunnel diode is a specially designed $p{-}n$ junction whose static current-voltage characteristics show NNDC. It was first invented in 1957 [18] and earned its inventor, Leo Esaki, the Nobel prize. After its invention, much research was carried out to exploit its NNDC property. The NNDC property can cause instability and generate oscillation in a tunnel diode circuit[19]. However, after the failure of the attempt to achieve widespread application, they were soon replaced by other semiconductor devices and are only used in certain niche applications nowadays[20].

The Gunn diode, invented in 1963 [21], has local N-shaped drift velocity vs. field characteristics due to the scattering of electrons to upper k-space valleys in the conduction band under high field. This is a bulk property of the semiconductor, which is also called the bulk negative differential conductivity effect. This bulk NNDC often gives rise to traveling field domains along the direction of current flow. A lot of work has been performed to model and analyze these traveling fronts. Gunn diodes are now widely used to generate signals at microwave frequencies from a few GHz to 100 GHz[22].

The superlattice was first proposed in 1970 by Esaki and Tsu [23]. It is an artificial structure composed of alternating layers of two different semiconductor materials, forming a periodic arrangement of quantum wells and barriers. Superlattices can be grown using single crystal depositing techniques such as molecular beam epitaxy (MBE) and metal organic chemical vapor deposition (MOCVD). These sophisticated techniques are capable of depositing layers as thin as a single atomic layer. A loose category of weakly- and strongly-coupled superlattices is based the degree of coupling of electrons in different quantum wells, which provides different mechanisms that give rise to NNDC. Accordingly, transport models that treat space as a continuous variable are developed for strongly-coupled superlattices while spatially discrete models are used to describe weakly-coupled superlattices. Thus, weakly-coupled superlattices have relatively thick barrier layers so that the electron gases in neighboring quantum wells can be viewed as only weakly-coupled to one another. On the other hand, strongly-coupled superlattices have relatively thin barriers and generally reveal the formation of mini-bands.

Although the mechanisms behind NNDC are different, the continuum model successfully predicts moving fronts inside the strongly-coupled superlattices similar to those in the Gunn diode. The continuum model can be viewed as a continuum limit of the discrete model. However, the discrete model is successful in predicting static current branches in the $I-V$ curves that are only observed in weakly-coupled superlattices. The moving wave fronts in superlattices are associated with current self-oscillation which can serve as a source of Gigahertz oscillation[24]. The quantum cascade laser which operates at far infrared and Terahertz regime is a specially designed superlattice that operates without field domains. Its rapid development and success in the last decade attracted renewed interest in superlattice structures.

Another remarkable feature of weakly-coupled superlattices is the presence of bistable states, i.e., for a range of fixed applied voltage, two distinct current states are possible. In regimes of bistability, the dynamics of the superlattice may be particularly sensitive to shot noise which may cause switching from the metastable state to the globally stable state. Stochastic switching between coexisting metastable states driven by noise is an important phenomena found in diverse nonlinear systems such as Josephson junctions [25], mechanical oscillators [26], genetic regulatory networks [27], chemical reactions [28], and protein folding [29]. Among the preceding examples, chemical reactions and protein folding are exceptional in that they are typically studied using thermal equilibrium theory; however, most of the preceding systems are far-from-equilibrium and also non-conservative, i.e., these are systems for which a global potential energy function cannot be defined. Stochastic switching phenomena are typically understood as an example of a noise-driven first-passage process [30]. For general stochastic systems, an expression for the mean first-passage time can be defined in terms of a backward Fokker-Planck equation. However, this equation can be analytically solved in closed form only for one-dimensional systems [30]. In potential energy systems with higher dimension, useful approximations can be defined by straightforward projection onto minimum energy escape paths [31]. But, for non-potential systems, analytical approximate forms for mean escape times are generally not available. In this thesis, I have addressed these questions in the weakly-coupled superlattice and the approaches I have implemented might be carried over to other non-conservative systems.

This thesis is organized as follows: In Chapter 2, the semiconductor superlattice is introduced. The sequential tunneling model for weakly-coupled superlattices and the miniband transport model for strongly-coupled superlattices are reviewed. In Chapter 3, the dependence of the front dynamics for weakly-coupled superlattices on the boundary condition - the contact conductivity, is investigated. Especially when the applied voltage is suddenly switched from one value to another, also known as transient response, the system shows different behavior depending on the contact conductivity and size and polarity of the switching voltage step. In Chapter 4, the model of the weakly-coupled superlattice with a shunting side layer is studied. It is found that a uniform field with high strength in the NDC region can be stabilized provided that the sample cross section is sufficiently narrow. In Chapter 5, the shunting idea is further tested on the strongly-coupled superlattice and the possibility of a superlattice based THz oscillator is discussed. In Chapter 6, stochastic switching from the metastable state to the stable state is simulated for the weakly-coupled superlattice. The scaling behavior of the mean switching time versus applied voltage is studied by fitting to a function of the applied voltage. In Chapter 7, a model of an array of tunnel diodes connected in series and its connection to superlattices is investigated and analogies with superlattice transport are studied. In the last Chapter, the thesis is summarized and some interesting future directions are discussed.

2

Vertical electronic transport in superlattices

In this chapter, we will discuss electronic transport theory in superlattices. Two major regimes of transport, sequential resonant tunneling and miniband transport, which are applied in weakly-coupled and strongly-coupled superlattices respectively, will be introduced. They are essential to understand the subsequent chapters. Other approaches will also be briefly discussed. The modeling of electronic transport in superlattices was recently reviewed by Wacker[32] and, separately, by Bonilla[33]. In addition, various advanced texts have a broad coverage of the different theoretical and modeling approaches to electronic transport in nanostructures, see, for example, Ref. [34].

2.1 Electronic transport in nanostructures

Nanostructures possess variation in some material property on the length scale of 100 nanometer or smaller in at least one dimension (1 nm = 10^{-9} m). Electrical currents can be generated by methods such as applying a potential difference between two electrodes of the structure or by immersing the system in an oscillating electric field. Due to the nanoscale feature of these systems, the phenomena of electronic transport can be very different from those systems with much larger characteristic dimensions.

Let's step back and consider electrical current carefully. Electrical current is a macroscopic phenomenon of collective behavior of all microscopic electrons under external forces. Thus, electronic transport is a non-equilibrium statistical problem. Many well-established equilibrium approaches, such as use of an equilibrium thermodynamic ensemble or quantum statistical theories, may not be fully applicable in non-equilibrium problems. To be more elaborate, in quantum mechanics, the whole system can be represented by a many-body state wave function $|\Phi(t)\rangle$ satisfying the time-dependent Schrodinger equation

$$i\hbar\frac{|\Phi(t)\rangle}{dt} = \hat{H}\,|\Phi(t)\rangle\,, \qquad |\Phi(t_0)\rangle = |\Phi_0\rangle\,, \tag{2.1}$$

where $\hat{H}$ is the many-body electron Hamiltonian. Since the exact state of the system is generally not known, the current is an ensemble average of all possible states $|\Phi_i(t)\rangle$ each with probability p_i. Thus, the observation (expectation value) of any operator $\hat{A}$ can be written as

$$\langle\hat{A}\rangle_t = \mathrm{Tr}\{\hat{\rho}(t)\hat{A}\}, \tag{2.2}$$

where $\hat{\rho}(t)$ is the density matrix

$$\hat{\rho}(t) = \sum_i p_i\,|\Phi_i(t)\rangle\,\langle\Phi_i(t)| \tag{2.3}$$

which evolves according to the Liouville-von Neumann equation for *closed* quantum systems

$$i\hbar\frac{d\hat{\rho}(t)}{dt} = [\hat{H}, \hat{\rho}(t)]. \tag{2.4}$$

By contrast, the *equilibrium* density matrix ρ^{eq} may be calculated within canonical or grand-canonical ensembles.

Notice that the state of the system $|\Phi\rangle$ can include information besides the electronic degrees freedom. When phonons are also considered $|\Phi_{e,ph}\rangle = |\Phi_e\rangle\,|\Phi_{ph}\rangle$, the Hamiltonian also includes electron-phonon interaction:

$$\hat{H} = \hat{H}_e + \hat{H}_{ph} + \hat{H}_{e-ph}, \tag{2.5}$$

where H_e and H_{ph} denote the electronic and phonon parts of the Hamiltonian, and H_{e-ph} denotes the electron-phonon interaction. One common approach to this many-body problem is via Green's functions which describe how a system evolves from a state q' at initial time t' to a state q at a later time t. Within the framework of second quantization, the Green's function can be written in terms of creation and annihilation operators. While the Green's function approach can deal with strong scattering processes, it results in integro-differential equations difficult to solve either numerically or theoretically.

Various theories have been developed to calculate current without directly solving equations such as Eq. 2.4 under different assumptions and approximations. We will develop our superlattice models based on the following two approaches:

One approach is the Kubo formalism, which models the system initially in global equilibrium subject to an small external perturbation by an electromagnetic field [35]. This formalism will be used to derive the tunneling current in weakly-coupled superlattices. The use of the Kubo formalism requires a few assumptions. For example, the system is assumed to evolve under Hamiltonian dynamics, i.e, closed quantum systems. However, it is subject to external forces, thus, not isolated. Also, the system is assumed to be initially in global equilibrium with a bath at temperature T. In weakly-coupled superlattices, electrons relax quickly due to phonon scattering (order of picoseconds) after tunneling, and this gives a local equilibrium in each quantum well of the superlattice, while the tunneling process is relatively slower depending on the miniband width (order of nanoseconds). This means perturbations are weak because the overlap of wave functions in neighboring quantum wells are very small.

Another approach is to simplify the scattering processes of electrons to some relaxation time τ, the average time between two successive collisions and this approach is inherently semiclassical in the sense that the electron is treated as a classical particle. As the collision can be either elastic or inelastic, two different relaxation times τ_E and τ_p can be defined, respectively. A classical model based on this assumption is the Drude model, which uses Newtonian dynamics. The Boltzmann transport equation is a semiclassical equation of motion for the non-equilibrium single particle distribution function and can be used to derive the miniband transport in strongly-coupled superlattices. The Boltzmann equation approach can also be derived fairly rigorously from microscopic quantum dynamics using the Wigner equation[36].

The above approaches are based on the viewpoint that the electronic current flows in response to an electric field. Yet there is another viewpoint: the field may be viewed as a consequence of carrier flow [34] - the Landauer approach that we will not use in this thesis. The idea is that the conductance between electrodes is a result of transmission, which can be calculated from Green's functions[34] or other methods[37]. Scatterers can induce self-consistent local fields, which then appear as self-energy terms in calculating the Green's functions.

2.2 The semiconductor superlattice

The remarkable progress of crystal growth technology has made possible to grow semiconductor structures composed of different semiconductor materials with astonishing precision at the level of one atomic layer at a time. These structures are called heterostructures. The sharp transitions between the composing materials cause abrupt changes of the conduction band and valence band, forming spatially varying potential energy for charge carriers in semiconductors, i.e., electrons and

	m_c	E_g	E_c
GaAs	$0.067m_e$	1.52 eV	0 eV
AlAs	$0.15m_e$	3.13 eV	1.05 eV

Table 2.1: GaAs and AlAs parameters at Γ point.

holes. The spatial structure of the potential energy can be designed by carefully choosing the composing materials, which is often referred to as *band engineering.* A myriad of devices have been fabricated based on semiconductor heterostructures.

The semiconductor superlattice was first proposed by Esaki and Tsu in 1970. It has a periodic arrangement of quantum wells and barriers, made of alternating layers of two different semiconductors deposited on each other along the growth direction z, illustrated in Fig. 2.1. One of the best-studied and most used systems is GaAs/$\mathrm{Al}_x\mathrm{Ga}_{1-x}\mathrm{As}$ because $\mathrm{Al}_x\mathrm{Ga}_{1-x}\mathrm{As}$ is always lattice matched with GaAs for any composition of Al, x. GaAs is always direct gap and $\mathrm{Al}_x\mathrm{Ga}_{1-x}\mathrm{As}$ is also direct for $x < 0.45$. They are widely used in optical devices for their direct bandgap. They form a type I heterostructure, where the material that has the higher conduction band edge has the lower valence band edge than the other material. This is clearly shown in Fig. 2.1(b), where $\mathrm{Al}_x\mathrm{Ga}_{1-x}\mathrm{As}$ forms barriers for both electrons and holes and GaAs is the quantum well material. The height of the barrier can be varied by changing the composition of Al, x. Some key parameters of GaAs and AlAs are listed in Table 2.1.

2.3 Electronic states in superlattices

In this thesis, I will only study electronic transport in n-doped superlattices, where the hole densities are negligible. At low temperature, the electrons are mostly trapped in the quantum wells. In order to study any quantum processes in the superlattices, one has to find a set of basis states formed by the electrons. For a

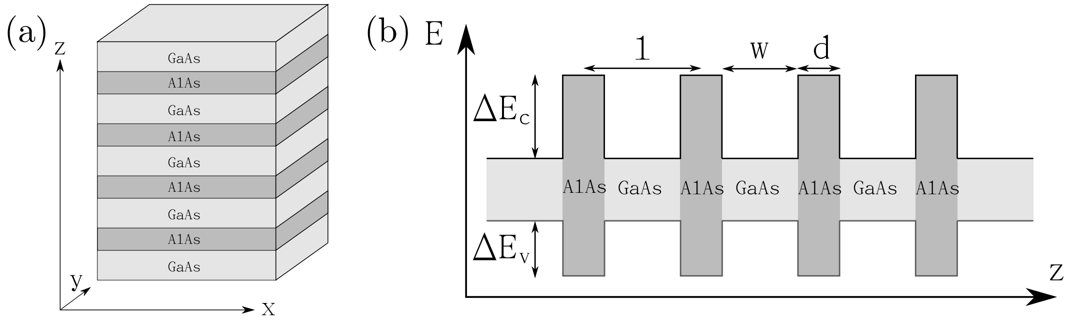

FIGURE 2.1: (a) Schematic of the superlattice structure. (b) Schematic of the band structure of the conduction band the valence band of the GaAs/AlAs superlattice with well width w, barrier width d and period $d = w + d$. The conductance band offset is ΔE_c and the valance band offset is ΔE_v.

single quantum well, the electron can only stay on discrete levels which can be obtained by solving the Schrödinger Equation. However, when many such wells are placed close enough to each other forming a superlattice, the states in different wells start to overlap and energy bands will form, similar to those in single crystals. In a superlattice, this can be described by the Kronig-Penney model [37].

Using the effective-mass approximation [37], which incorporates the effects of the ion potential to the conduction band and effective mass, the Hamiltonian of electrons in the superlattice can be written as

$$H = -\nabla \frac{\hbar^2}{2m^*(z)} \nabla + E_c(z) \tag{2.6}$$

where $E_c(z)$ is the conduction band edge seen by electrons as potential and $m^*(z)$ is the effective mass. The z dependence in these two variables is due to the periodic structure of the superlattice. The vertical and the lateral dynamics can be decoupled with eigenfunctions of the form

$$\psi_{\mathbf{k}_\perp}(\mathbf{r}_\perp, z) = e^{i\mathbf{k}_\perp \cdot \mathbf{r}_\perp} \psi(z) \tag{2.7}$$

where $\mathbf{r}_\perp$ and $\mathbf{k}_\perp$ lie in the lateral (x, y) plane. The vertical part obeys the one-dimensional Hamiltonian

$$H_z = -\frac{\partial}{\partial z}\frac{\hbar^2}{2m^*(z)}\frac{\partial}{\partial z} + E_c(z) \tag{2.8}$$

Hence the Bloch's theorem applies and the eigenfunctions have the form of

$$\psi_k(z) = e^{ikz}u_k(z) \tag{2.9}$$

where $u_k(z)$ is a rapidly varying function with period of the underlying superlattice structure, i.e., $u_k(z + nl) = u_k(z)$ for any integer n, while the Bloch wave vector k along z direction gives the phase shift of the wave function from one period to the next. It also can be viewed as the free electron wavefunction e^{ikz} modulated by $u_k(z)$.

Using the transfer or T-matrix, it can be shown [37] that the Bloch wave vector k satisfies

$$\cos kl = \cos k_W w \cosh \kappa_B b - \frac{(k_W/m_W^*)^2 - (\kappa_B/m_B^*)^2}{2(k_W/m_W^*)(\kappa_B/m_B^*)}\sin k_W w \sinh \kappa_B b \tag{2.10}$$

where m_W^* and m_B^* are the effective mass of electron in the wells and in the barriers, respectively; $k_W = \sqrt{2m_W^* E_k}/\hbar$ and $\kappa_B = \sqrt{2m_B^*(\Delta E_C - E_k)}/\hbar$ are the wave numbers in the quantum wells and barriers, respectively; E_k is the energy of the electron. The right hand side of this equation is a function of E_k and the value must lie in $[-1, 1]$. Thus, the allowed energy state of electrons form energy bands, called minibands with bandwidth Δ^ν, where $\nu = 1, 2, ...$ The corresponding states are called Bloch states $\phi_k^\nu(z)$ and can be specified with band number ν and Bloch vector k. The example shown in Fig. 2.2 has relatively wide minibands. These are called strongly-coupled superlattices. As the barrier becomes thicker, the miniband width becomes narrower. For very thick barriers, the electrons are localized within each well. This is called the weakly-coupled superlattice. When the coupling lies between

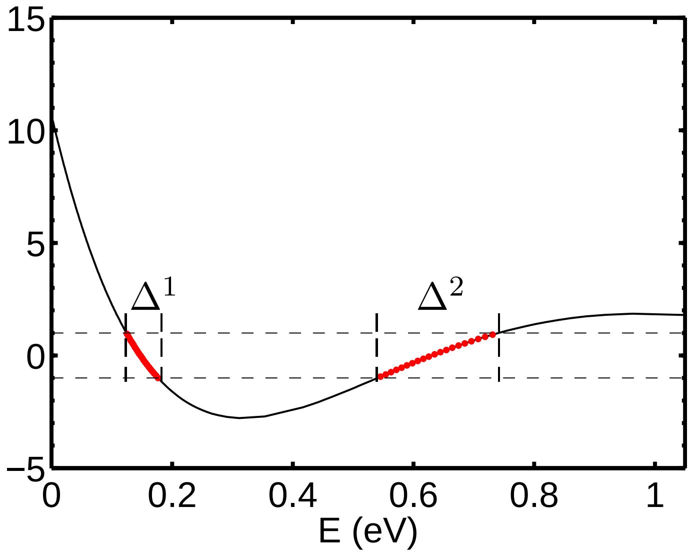

FIGURE 2.2: the Kronig-Penney model for a GaAs/AlAs 4/1 superlattice with $w = 4$ nm and $b = 1$ nm. The first miniband width Δ^1 is 55 meV. See also Ref. [38].

these two extreme cases, the tight-binding approach can be used[32]. A particular and special superposition of Bloch states allows one to define the Wannier states as follows

$$\Phi^\nu(z) = \sqrt{\frac{l}{2\pi}} \int_{-\pi/l}^{\pi/l} dk \phi_k^\nu(z). \tag{2.11}$$

This is a localized wave function with exponentially decaying extension into neighboring wells.

2.4 Electronic transport in superlattices

Different types of superlattices lead to different approaches of electronic transport such as miniband transport, Wannier-Stark hopping and sequential tunneling. Wacker [32] proposed ranges of validity for the different approaches for superlattice transport. This is shown in Fig. 2.3, where $\Gamma = \hbar/\tau$ is the broadening of the individual energy levels due to scattering and τ is the scattering time, the average time the electron stays in one Bloch state before scattered to another Bloch state. We may

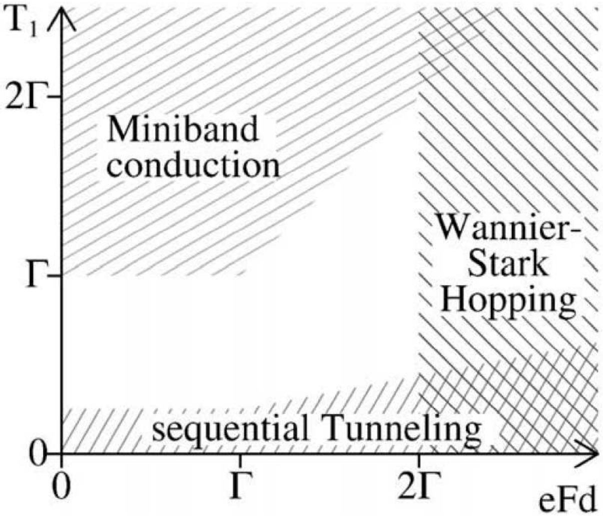

FIGURE 2.3: Different approaches for electronic transport in superlattices (reproduced from Ref. [32]).

expand the miniband structure $E^\nu(k)$ calculated from the Kronig-Penney method as

$$E^\nu(k) = E^\nu + \sum_{h=1}^{\infty} 2T_h^\nu \cos(hkz), \tag{2.12}$$

where T_h^ν are coupling strength in the Hamiltonian of the superlattice within the Wannier basis

$$H_{\text{superlattice}} = \sum_{n,\nu} \left[E^\nu a_n^{\nu\dagger} a_n^\nu + \sum_{h=1}^{\infty} T_h^\nu (a_{n+h}^{\nu\dagger} a_n^\nu + a_{n-h}^{\nu\dagger} a_n^\nu) \right]. \tag{2.13}$$

where $a_{n+h}^{\nu\dagger}$ and a_n^ν are creation and annihilation operators of the state ν at position n associated with the Wannier functions, respectively. It has been shown that the first component, i.e, the nearest neighbour coupling strength $T_1^\nu \approx \Delta^\nu/4$ [32].

So Fig. 2.3 suggests that miniband transport applies to the case where the voltage drop across a period is smaller than one fourth of the miniband width and the miniband width is larger than four times the scattering broadening. As the fields becomes large, the electronic transport is treated as hopping between elements of the

Wannier-Stark ladder, which are the eigenstates of the Hamiltonian with energies $E_j = E_0 - jeFl$ and, similar to Wannier states, extends over several periods. Finally, if the bandwidth is extremely narrow for thick barriers, the electrons are localized in each well. The transport in this case is due to the residual coupling between neighboring wells leading to tunneling through barriers, which is called sequential tunneling from well to well.

In the next two sections, we will review the sequential tunneling model and the miniband transport model which correspond to the weakly- and the strongly-coupled superlattices, respectively, the two types of superlattices that we study in this thesis.

2.5 The sequential tunneling model for weakly-coupled superlattices

The discrete rate equation model that we employ for the simulations below has been developed over the past several years and has proved useful to model experimental results with good accuracy for parameters so far studied (for a review, see Ref. [33]). A heuristic derivation of the model using Fermi's golden rule has also been presented in Ref. [33]. Here we present an alternative derivation of the discrete rate equation model starting from a microscopic tunneling Hamiltonian that aptly characterizes the weakly-coupled superlattice. Among the advantages of this approach are that it is relatively straightforward to generalize to include additional physical effects, such as phonon scattering, phonon- or photon-assisted tunneling, or electron-electron interaction.[39] Additionally, this approach makes clear that the derived rate equation model is the result of a consistent first-order perturbation theory; such an approach could also serve as a starting point for calculations that are higher order in tunnel coupling as would be needed, e.g., if one were to consider somewhat thinner barriers.

The tunneling Hamiltonian is written as follows:[40, 41]

$$\begin{aligned} H_{total} &= H + H_T \qquad (2.14) \\ &= \sum_{i=0}^{N+1} H_i + \sum_{j=0}^{N} H_{Tj} \\ &= \sum_{i=0}^{N+1} \sum_{\mathbf{k}_i} E_{i\mathbf{k}_i} c^{\dagger}_{i\mathbf{k}_i} c_{i\mathbf{k}_i} + \sum_{j=0}^{N} \sum_{\mathbf{k}_j \mathbf{k}_{j+1}} (T_{\mathbf{k}_{j+1}\mathbf{k}_j} c^{\dagger}_{j+1\mathbf{k}_{j+1}} c_{j\mathbf{k}_j} + \text{h.c.}). \qquad (2.15) \end{aligned}$$

Here the summation over i extends over the left lead ($i = 0$), the quantum wells ($i = 1$ to N) and the right lead ($i = N+1$). The operators $c^{\dagger}_{i\mathbf{k}_i}$ ($c_{i\mathbf{k}_i}$) denote creation (annihilation) operators for electrons in the i-th well or lead with three-dimensional momentum $\mathbf{k}_i$, and satisfy standard fermionic commutation rules: $\{c_{i\mathbf{k}_i}, c_{j\mathbf{k}_j}\} = c_{i\mathbf{k}_i}c_{j\mathbf{k}_j} + c_{j\mathbf{k}_j}c_{i\mathbf{k}_i} = 0$, $\{c^{\dagger}_{i\mathbf{k}_i}, c^{\dagger}_{j\mathbf{k}_j}\} = 0$, $\{c_{i\mathbf{k}_i}, c^{\dagger}_{j\mathbf{k}_j}\} = \delta_{ij}\delta_{\mathbf{k}_i\mathbf{k}_j}$. The amplitude $T_{\mathbf{k}_{j+1}\mathbf{k}_j}$ denotes the tunneling matrix element between the j-th and $j+1$-th well/lead. In this model, the unperturbed Hamiltonian H denotes a sum of individual Hamiltonians for each quantum well or lead and assumes that they are uncoupled from one another. The unperturbed single-electron states have absolute energies denoted by $E_{i\mathbf{k}_i}$ which are defined such that, for all i, the zero of energy is taken as the conduction band edge in the left lead (i.e., the emitter contact). Below, it will be convenient to define an alternative quantity $\epsilon_{\mathbf{k}_i}$ as the energy of the single-particle states relative to the conduction band edge of the i-th well/lead. The relationship between these two ways of expressing energy is summarized in $E_{i\mathbf{k}_i} = \epsilon_{\mathbf{k}_i} + eV_i$ where $e < 0$ is the electron charge and V_i denotes the electric potential at the position of the i-th well/lead. Furthermore, each quantum well comprises a set of two-dimensional free electron gases - one for each subband. Each quantum well or lead is assumed to be characterized by a distinct *internal* chemical potential value μ_i and these are determined below using a self-consistency argument based on the classical Poisson equation. The entire system is assumed to have temperature T. The second term in Eq. 2.15, H_T, represents the effect of tunnel coupling between adjacent wells and/or leads and is treated as a small perturbation, expected to be appropriate for weakly-coupled superlattices. It should also be noted that when an energetic electron tunnels into a quantum well it is assumed to relax instantly to the ground state for that quantum well.

The tunneling current from the i-th period to $i+1$-th period in steady state may be expressed in terms of the rate of change of the number of particles in the i-th period.[35] This rate can be expressed in terms of a commutator of the number operator $N_i = \sum_{\mathbf{k}_i} c^{\dagger}_{i\mathbf{k}_i} c_{i\mathbf{k}_i}$ with the total Hamiltonian:

$$\begin{aligned} e\dot{N}_i &= \frac{i}{\hbar}\left[H_{total}, eN_i\right] \\ &= \frac{i}{\hbar}\left[H_{Ti-1}, eN_i\right] + \frac{i}{\hbar}\left[H_{Ti}, eN_i\right] \\ &= \hat{I}_{i-1\to i} - \hat{I}_{i\to i+1}. \end{aligned} \tag{2.16}$$

Here, $\hat{I}_{i-1\to i} = \frac{i}{\hbar}\left[H_{Ti-1}, eN_i\right]$ corresponds to the tunneling current operator from $i-1$-th period to i-th period and a similar definition applies for $\hat{I}_{i\to i+1}$. Going to the interaction representation, the operators transform according to $H_T(t') = \mathrm{e}^{iHt'} H_T \mathrm{e}^{-iHt'}$ and $\hat{I}_{i\to i+1}(t) = \mathrm{e}^{iHt}\hat{I}_{i\to i+1}\mathrm{e}^{-iHt}$, and we may express the tunneling current from i-th period to $i+1$-th period in terms of the following Kubo formula [35]

$$I_{i\to i+1}(t) = \int_{-\infty}^{t} dt' \langle \left[\hat{I}_{i\to i+1}(t), H_{Ti}(t')\right] \rangle. \tag{2.17}$$

Here it is understood that the expectation value is computed using the appropriate unperturbed thermodynamic ground states for the two electron gases in the i-th and $i+1$-th wells. Note that this expression is first order in the perturbation, H_T.

The evaluation of Eq. 2.17 is straightforward if somewhat lengthy, and the resulting current can be simply expressed as

$$I_{i\to i+1} = \frac{4\pi e}{\hbar}\sum_{\mathbf{k}_i\mathbf{k}_{i+1}} |T_{\mathbf{k}_{i+1}\mathbf{k}_i}|^2\,\delta(\epsilon_{\mathbf{k}_{i+1}} - \epsilon_{\mathbf{k}_i} - eF_i l)\left[n_F(\epsilon_{\mathbf{k}_{i+1}} - \mu_{i+1}) - n_F(\epsilon_{\mathbf{k}_i} - \mu_i)\right], \tag{2.18}$$

where $n_F(x) = [1 + exp(x/k_BT)]^{-1}$ denotes the Fermi function, and we have defined F_i as the average electric field between wells i and $i+1$ so that, in terms of electric potential, one writes $-F_i = (V_{i+1} - V_i)/l$. The tunneling matrix element is calculated using a method due to Bardeen:[42, 41]

$$|T_{\mathbf{k}_{i+1}\mathbf{k}_i}|^2 = \frac{\hbar^4}{4m^{*2}}\mathcal{T}_i(\epsilon_{i,z})\,\delta_{\mathbf{k}_{i\perp},\mathbf{k}_{i+1\perp}}, \tag{2.19}$$

where

$$\begin{aligned}
\mathcal{T}_i(\epsilon_{i,z}) &= \frac{16k_i^2k_{i+1}^2\alpha_i^2(k_i^2+\alpha_i^2)^{-1}(k_{i+1}^2+\alpha_i^2)^{-1}}{(w+\alpha_{i-1}^{-1}+\alpha_i^{-1})(w+\alpha_{i+1}^{-1}+\alpha_i^{-1})e^{2\alpha_i d}}, && (2.20)\\
\hbar k_i &= \sqrt{2m^*\epsilon_{i,z}}, && (2.21)\\
\hbar k_{i+1} &= \sqrt{2m^*[\epsilon_{i,z}+e(d+w)F_i]}, && (2.22)\\
\hbar\alpha_{i-1} &= \sqrt{2m^*\left[|e|V_b + e\left(d+\frac{w}{2}\right)F_i - \epsilon_{i,z})\right]}, && (2.23)\\
\hbar\alpha_i &= \sqrt{2m^*\left[|e|V_b - \frac{ewF_i}{2} - \epsilon_{i,z})\right]}, && (2.24)\\
\hbar\alpha_{i+1} &= \sqrt{2m^*\left[|e|V_b - e\left(d+\frac{3w}{2}\right)F_i - \epsilon_{i,z})\right]}. && (2.25)
\end{aligned}$$

Here, $\mathbf{k}_{i\perp}$ is the component of $\mathbf{k}_i$ perpendicular to the current flow, $\epsilon_{i,z}$ is the energy in the parallel direction - i.e., the z component of the total energy $\epsilon_{\mathbf{k}_i}$, d denotes the width of one barrier, w the width of one well, and m^* the electron effective mass (taken as 8.43×10^{-32} kg corresponding to an appropriately weighted average of GaAs and AlAs effective masses). Additionally, $|e|V_b$ is the barrier height in the absence of an applied potential drop (taken as 0.982 eV for the GaAs/AlAs interface).

In order to calculate the current $I_{i\to i+1}$, we carry out the summation in Eq. (2.18) in the parallel directions and sum over the subband energy levels by inserting a spectral function $A_\nu(\epsilon_z)$ which is centered at νth level $\mathcal{E}_\nu$ with a scattering width γ_ν

$$A_\nu(\epsilon_z) = \frac{\gamma_\nu/\pi}{(\epsilon_z - \mathcal{E}_\nu)^2 + \gamma_\nu^2}. \tag{2.26}$$

For transport between adjacent quantum wells, Eq. (2.18) can be written as

$$I_{i\to i+1} = \frac{\pi\hbar^3 e}{m^{*2}} \sum_{\nu=1}^{n_{max}} \sum_{\mathbf{k}_{i\perp}\mathbf{k}_{i+1\perp}} \int A_1(\epsilon_{i,z})d\epsilon_{i,z} \int A_\nu(\epsilon_{i+1,z})d\epsilon_{i+1,z}$$

$$\times \mathcal{T}_i(\epsilon_{i,z})\ \delta(\epsilon_{\mathbf{k}_{i+1}} - \epsilon_{\mathbf{k}_i} - eF_i l)\left[n_F(\epsilon_{\mathbf{k}_{i+1}} - \mu_{i+1}) - n_F(\epsilon_{\mathbf{k}_i} - \mu_i)\right]\ \delta_{\mathbf{k}_{i\perp},\mathbf{k}_{i+1\perp}}. \tag{2.27}$$

Carrying out the $\mathbf{k}_\perp$ summations and the integration over $\epsilon_{i+1,z}$, dividing by cross-sectional area, and replacing the remaining integration variable $\epsilon_{i,z}$ with ϵ, we can write the current *density* as

$$J_{i\to i+1} = e\frac{\hbar k_B T}{2m^*} \sum_{\nu=1}^{n_{max}} \int_0^{+\infty} A_1(\epsilon)A_\nu(\epsilon + eF_i l)\mathcal{T}_i(\epsilon) \ln\left(\frac{1+\mathrm{e}^{(\mu_i-\epsilon)/k_BT}}{1+\mathrm{e}^{(\mu_{i+1}-eF_il-\epsilon)/k_BT}}\right) d\epsilon, \tag{2.28}$$

which is identical to the tunneling current expression derived using a Fermi's golden rule approach as described, e.g., in Ref. [33].

The integral of Eq. (2.28) can be approximately calculated by assuming the scattering width is small compared to the subband energies and chemical potentials:

$$J_{i\to i+1} = \frac{ev^f(F_i)}{l}\left\{n_i - \frac{m^*k_BT}{\pi\hbar^2}\ln\left[1+\exp\left(-\frac{eF_il}{k_BT}\right)\times\left(\exp\left(\frac{\pi\hbar^2 n_{i+1}}{m^*k_BT}\right)-1\right)\right]\right\}, \tag{2.29}$$

where we have defined the two-dimensional electron density in the i-th well

$$n_i = \frac{m^*k_BT}{\pi\hbar^2}\ln\left[1+\mathrm{e}^{(\mu_i-\mathcal{E}_1)/k_BT}\right], \tag{2.30}$$

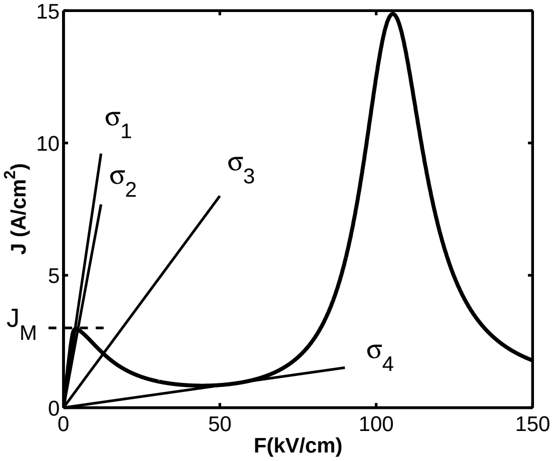

FIGURE 2.4: Tunneling current density for well-to-well transport vs. electric field under uniform electric field conditions $J_{superlattice}(F)$. The straight lines represent Ohmic contact characteristics for different σ values: $\sigma_1 = 0.08(\Omega\text{m})^{-1}$, $\sigma_2 = 0.064(\Omega\text{m})^{-1}$, $\sigma_3 = 0.016(\Omega\text{m})^{-1}$, and $\sigma_2 = 0.00168(\Omega\text{m})^{-1}$.

and the effective electron drift velocity

$$v^{(f)}(F_i) = \sum_{j=1}^{n_{max}} \frac{\frac{\hbar^3 l(\gamma_1+\gamma_j)}{2m^{*2}}\, \mathcal{T}_i(\mathcal{E}_1)}{(\mathcal{E}_1 - \mathcal{E}_j + eF_i l)^2 + (\gamma_1+\gamma_j)^2}. \tag{2.31}$$

Equation (2.29) above indicates that, in general, the tunneling current density depends on the variables n_i, n_{i+1}, and F_i and this dependence can be clarified by writing $J_{i\to i+1}(n_i, n_{i+1}, F_i)$. In Fig. 2.4 we plot the field dependence under the condition of uniform electric field (equiv., no net space charge) so that $n_i = n_{i+1} = N_D$, where N_D is the two-dimensional doping density in the i-th well; this defines the superlattice current-field characteristic which we denote as follows: $J_{superlattice}(F_i) \equiv J_{i\to i+1}(N_D, N_D, F_i)$.

The fundamental tunneling current expression, Eq. (2.18), can also be used to develop (generally nonlinear) current-field characteristics that describe transport from the emitter to the first quantum well or from the last well into the collector. A key ingredient is the structure of electronic states in the emitter/collector, typically different than the structure of states in the quantum wells. One plausible approach treats the emitter as a three-dimensional Fermi gas of electrons with local chemical potential determined by the donor concentration in the contact region.[40, 43] We have performed our calculations using both this microscopic boundary condition and an Ohmic boundary condition and we find good agreement, provided that the effective σ value is chosen so that the microscopically-based contact $J-F$ characteristic and the Ohmic characteristic both intersect the $J-F$ curve of the superlattice at the same point (cf. Fig. 2.4). A separate question of importance for experiment is to relate the effective value of σ to parameters that can be controlled in real superlattices, for example, the donor concentrations in the emitter and collector and the thicknesses of the first and last superlattice barriers. We will study these effects and the results in Chapter 3[44]. For the present study, we use the following Ohmic boundary conditions:[43, 45]

$$J_{0\to 1} = \sigma F_0, \tag{2.32}$$

$$J_{N\to N+1} = \sigma F_N \frac{n_N}{N_D}, \tag{2.33}$$

where σ denotes the effective contact conductivity.

Integrating over one superlattice period, the Poisson equation and the charge continuity equation are expressed as:

$$F_i - F_{i-1} = \frac{e}{\varepsilon}(n_i - N_D), \quad i = 1, ..., N. \tag{2.34}$$

$$e\frac{dn_i}{dt} = J_{i-1\to i} - J_{i\to i+1}, \quad i = 1, ..., N. \tag{2.35}$$

where ε is the dielectric constant. Equations (2.34) and (2.35) together with the boundary conditions, Eqs. (2.32) and (2.33), comprise the sequential tunneling model that we simulate, which takes the form of a rate equation model with the nonlinear drift-diffusion current of Eq. (2.29). The fundamental dynamical variables are the averaged field values in each quantum well plus the field values in the injecting and receiving contacts. Differentiating Eq. (2.34) with respect to time gives:

$$\varepsilon\frac{dF_i}{dt} + J_{i\to i+1} = J(t), \quad i = 0, ..., N. \tag{2.36}$$

in which the total current density $J(t)$ is the same for all periods. The bias condition is

$$\frac{1}{N+1}\sum_{i=0}^{N} F_i = \frac{V(t)}{(N+1)l}, \tag{2.37}$$

where $V(t)$ is the total voltage bias across the sample. This is a global coupling among all the field values.

For simulations reported in this thesis, the parameter values generally follow the experimental structure of Rogozia *et al.*[46] Thus, the number of superlattice periods is $N = 40$ while the doping density in each quantum well is $N_D = 1.5 \times 10^{11}$ cm^{-2}. The widths of each quantum well and barrier are 9 nm and 4 nm, respectively, which implies that the subband energies are $\mathcal{E}_1 = 44$ meV, $\mathcal{E}_2 = 180$ meV, and $\mathcal{E}_3 = 410$ meV. Additionally, we assume that the scattering widths are independent of subband index so that $\gamma = \gamma_j = 8$ meV. [45, 47]

2.6 Miniband transport

Miniband transport, also sometimes referred to as semiclassical transport, was first discussed by Esaki and Tsu in the paper where the superlattice was originally proposed[23]. The approach they followed is very simple and intuitive. Assume the dispersion relation of the miniband energy E and Bloch vector k is approximately given by the following form that can be derived for electrons in a weakly periodic potential [48]:

$$E(k) \approx E(0) - \frac{\Delta}{2}\cos(kl). \tag{2.38}$$

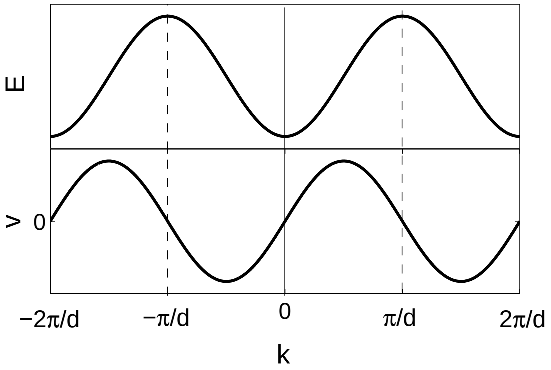

Figure 2.5: Schematic of energy and velocity versus Bloch vector.

The velocity of an electron moving in the potential is given by

$$v(k) = \frac{1}{\hbar}\frac{\partial E}{\partial k} = \frac{\Delta d}{2\hbar}\sin(kl). \tag{2.39}$$

This is illustrated in Fig. 2.5. Under an external electric field F, the electron is accelerated as

$$\frac{dk}{dt} = \frac{eF}{\hbar}. \tag{2.40}$$

Or, $k = eFt/\hbar$, i.e., the Bloch vector increases linearly in time. Substituting this result back in Eq. 2.39, we see that the velocity oscillates in time with the Bloch frequency $\omega_B = elF/\hbar$, which depends on the applied voltage. If there is no scattering, the electron will perform oscillation without drifting. This ideal oscillation is called the Bloch oscillation, but has never been observed in single crystals. This is because scattering processes tend to restore the electron to thermal equilibrium and, thus, before the Bloch vector can increase significantly, it is scattered back to near $k = 0$. So k can only explore a very narrow range near $k = 0$ in the first Brillouin space.

However, for the superlattice, the electron can explore a wider range in the first Brillouin space because the lattice constant, i.e., the period of the superlattice, is significantly larger than the lattice constant of a crystal. Equivalently, the size of the first Brillouin space $2\pi/d$ becomes much smaller, so the electron has a chance to explore a wider range in the first Brillouin space before being scattered. This effect is manifested in the following remarkable current-field characteristic, see Fig. 2.6. As the field becomes larger, the electron can explore a wider k space and possibly perform a few periods of Bloch oscillation. For an ensemble of electrons, this *reduces* the average drift velocity. So the drift velocity decreases as the field increases for high field. The drift velocity can be written as

$$v_d = v_m \frac{2eFd/\Gamma}{1 + (eFd/\Gamma)^2} = v_m \frac{2F/F_c}{1 + (F/F_c)^2} \tag{2.41}$$

Again, $\Gamma = \hbar/\tau$ is the broadening due to scattering. This is called the Esaki-Tsu characteristic and was derived by them using an elementary kinetic theory argument. [23]. When $F = F_c \equiv \hbar/ed\tau$, the drift velocity reaches a local maximum. For larger τ and fixed F, the electron can perform more periods of Bloch oscillation and thus v_d enters negative differential region more easily, i.e., smaller F_c.

This relation is derived more rigorously using the Boltzmann equation. Denote $f(k)$ as the steady-state distribution function of electrons in k space, which satisfies the one-dimentional Boltzmann equation [49].

$$\frac{\partial f}{\partial t} + \frac{eF}{\hbar}\frac{\partial f}{\partial k} = -\frac{1}{\tau}(f - f_0), \tag{2.42}$$

where f_0 is the equilibrium distribution without an external electric field. The current can be written as

$$j = 2e \int v(k)\, f(k) dk, \tag{2.43}$$

where $v(k) = \partial E(k)/\partial k$. We can solve Eq. 2.42 for f in the integral form and substitute f into Eq. 2.43. Then, we Fourier transform it into frequency domain and, in the low frequency limit, it can be shown the current has the form

$$j = j_0 \frac{2eFd/\Gamma}{1 + (eFd/\Gamma)^2}. \tag{2.44}$$

In the above equation, the peak current

$$j_0 = \frac{eN\Delta d}{4\hbar}\frac{I_1(\Delta/2k_BT)}{I_0(\Delta/2k_BT)}, \tag{2.45}$$

where $I_k(x)$ are modified Bessel functions. The factor $\frac{I_1(\Delta/2k_BT)}{I_0(\Delta/2k_BT)}$ accounts for the temperature effect. As the temperature increases such that k_BT is larger than the miniband width Δ, the electrons almost uniformly occupy the miniband although not fully. Thus, the electric field is unable to alter this momentum distribution and conductivity of the superlattice vanishes. This is called thermal saturation [50]. The miniband transport model forms the basis of a drift-diffusion transport model for strongly-coupled superlattices as discussed in detail in Chapter 5.

2.6.1 Gain

A remarkable property of this transport process in strongly-coupled superlattice concerns the behavior of the ac gain up to and near, but just below the Bloch frequency. Consider the applied field as a superposition of a dc field F and an ac field:

$$F(t) = F + F_1\cos(\omega t). \tag{2.46}$$

This is illustrated with the Esaki-Tsu characteristic in Fig. 2.6. The energy transferred from the alternating field to the medium is

$$P = \int j(t)F_1\cos(\omega t)dt. \tag{2.47}$$

If the increase of electric field causes decrease of the current, then $P < 0$, and the energy is transferred from the medium to the alternating field, causing amplification.

Ktitorov *et. al.* were the first to point out this gain in their seminal paper [51]. They linearized the Boltzmann equation with both the elastic and the inelastic scattering time constants and found the high-frequency conductivity of the form:

$$\sigma(\omega) = \sigma_0\frac{1-\omega_B^2\tau_e\tau_p - i\omega\tau_e}{(\omega_B^2-\omega^2)\tau_e\tau_p + 1 - i\omega(\tau_p+\tau_e)}. \tag{2.48}$$

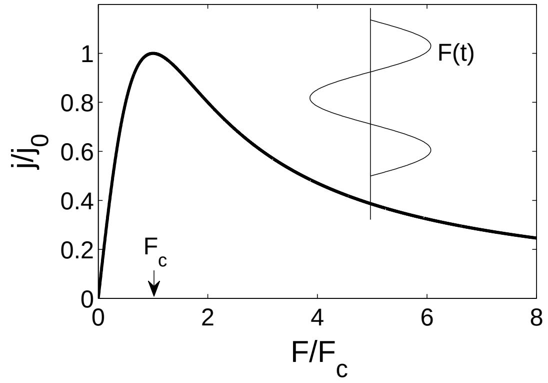

FIGURE 2.6: $J - F$ characteristics for miniband transport.

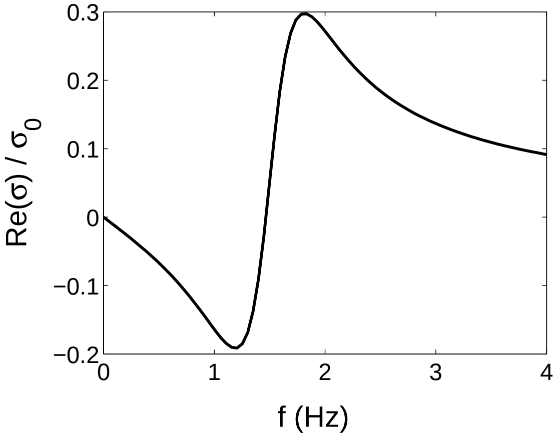

FIGURE 2.7: Real part of conductivity for $f_B = 1.5$ THz and $\tau_i = \tau_e = 0.5$ ps.

When $\omega_E^2 \tau_p \tau_e > 1$, the optical propagation constant

$$\alpha = \frac{\sigma(\omega)}{\sqrt{\epsilon}\epsilon_0 c} \tag{2.49}$$

has a negative real part for the frequency from 0 to near ω_B and has a maximally negative real part just below ω_B.

It is more instructive to rewrite this gain using a quantum derivative notation[52]

$$g = -\frac{ed}{n_r \epsilon_0 c} \frac{j_{dc}(eFd + \hbar\omega) - j_{dc}(eFd - \hbar\omega)}{2\hbar\omega}. \tag{2.50}$$

This has the meaning that the gain/absorption is proportional to the dc differential conductivity while the energy is discretized in units of the photon energy $\hbar\omega$.

Now this can be explained in terms of the quantum-mechanical Wannier-Stark picture[53]. The individual Wannier-Stark ladder states are shifted in space in units of a superlattice period. Since the energy drop across each period is elF, the energy difference between neighboring Wannier-Stark ladders is equal to elF, which is also equal to $\omega_B\hbar$ by simply rewriting the Bloch frequency. The transition between neighboring Wannier-Stark ladder states may also be assisted by phonon, which can cause emission and absorption of photons with energy slightly less than $\hbar\omega_B$. This explanation has been fully described by Willenberg *et.al.*[53] using density matrix calculation. The gain obtained using this approach agrees very well with the gain obtained from the semiclassical approach, that is, Eq. 2.50 above in high temperature limit.

3

Dependence of front dynamics on contact conductivity in weakly-coupled superlattices

The current vs. field curves with NDC introduced in Chapter. 2 describe the local property in superlattices: the tunneling current through a barrier in weakly-coupled superlattices or the current at one point in strongly-coupled superlattices. When a bias voltage is applied across the whole structure, the current vs. total voltage curve turns out to be quite different from the local current vs. field curves. The underlying reason is that the field inside the superlattice is non-uniform and forms domains. The interfaces where field domains with different field intensities meet are called fronts, much as the fronts in fluid dynamics. The weakly-coupled superlattice is a system where rich front dynamics occurs, manifested by the total current and its relationship with the applied voltage.

In this Chapter, we will study front dynamics in weakly-coupled superlattices with different contact conductivities. We will first see static or moving field domains/fronts under fixed bias voltages. Then we will study how the system respond to sudden switching of the bias voltage.

3.1 The model for one-dimensional superlattices

To remind ourselves of the sequential tunneling model, the model equations which are the Poisson equation (2.34), the charge continuity equation (2.35) and the total applied voltage (2.37) are copied here:

$$F_i - F_{i-1} = \frac{e}{\varepsilon}(n_i - N_D), \quad i = 1, ..., N. \tag{3.1}$$

$$e\frac{dn_i}{dt} = J_{i-1\to i} - J_{i\to i+1}, \quad i = 1, ..., N. \tag{3.2}$$

$$l\sum_{i=0}^{N} F_i = V(t), \tag{3.3}$$

This model is for one-dimensional superlattices where the dynamics in the lateral direction is assumed to be uniform and neglected. Only the dynamics along the growth direction z is considered in this model.

The charge continuity equation determines the evolution of electron density n_i in time and space. It is composed of partial derivative of n_i with respective to time and difference of currents due to the discrete nature of weakly-coupled superlattices. In continuum limit, it is a partial differential equation. However, due to the unique structure of this system which we will show below, this system can be cleverly written as a ordinary differential equation set, which not only is easier to simulate but also easier to perform stability analysis on.

First, differentiating Eq. (3.1) with respect to time and plugging into Eq. (3.2):

$$\varepsilon\frac{dF_i}{dt} + J_{i\to i+1} = J(t), \quad i = 0, ..., N. \tag{3.4}$$

in which the total current density $J(t)$ is the same for all periods. This equation tells us that the total current is composed of the tunneling current $J_{i\to i+1}$ and the displacement current $\varepsilon dF_i/dt$. Moreover, the total current is the same everywhere inside the superlattice. Summing Eq. 3.4 over index i, one obtains the total current in terms of all F_i:

$$J(t) = \frac{1}{N+1}\frac{\varepsilon dV}{l\, dt} + \frac{1}{N+1}\sum_{i=0}^{N} J_{i\to i+1}, \tag{3.5}$$

where we applied the total voltage condition Eq. 3.3. Then plugging Eq. 3.5 back into Eq. 3.4 yields:

$$\frac{dF_i}{dt} = \frac{1}{(N+1)l}\frac{dV}{dt} + \frac{1}{(N+1)\varepsilon}\sum_{j=0}^{N} J_{j\to j+1} - \frac{1}{\varepsilon}J_i, \tag{3.6}$$

for $i = 0, ..., N$.

Now we have rewritten the model equations (3.1) - (3.3) to a system of ordinary differential equations (ODEs). The advantage of this representation of the model is that the bias condition, Eq. (3.3), is naturally embedded and this renders the numerical simulation straightforward and relatively stable. We have used both first-order Euler and fourth-order Runge-Kutta methods to solve this system (3.6), with initial condition

$$E_i(0) = E_{i0}, \quad i = 0, ...N, \quad \phi(0) = \sum_{i=0}^{N} \frac{E_{i0}}{N+1}. \tag{3.7}$$

The simulations show rapid convergence, so it is not necessary to use higher order or implicit methods.

3.2 Contact conductivity vs. doping density

The microscopic model for the tunneling current through the boundary is similar to the tunnelling within the superlattice [54]. From Eq. 2.27, treating the contact as three dimensional Fermi gas and calculate the tunneling matrix T, we have the tunneling current from the emitter contact:

$$J_{0\to 1} \approx j_e^{(f)}(F_0) - n_1 w^{(b)}(F_0), \tag{3.8}$$

$$j_e^{(f)}(F_0) = \sum_{j=1}^{n} \frac{16k_0^2k_1^2\alpha_0^2(k_0^2+\alpha_0^2)^{-1}(k_1^2+\alpha_0^2)^{-1}}{(w+\alpha_0^{-1}+\alpha_1^{-1})\mathrm{e}^{-2\alpha_0 d}}\theta\left(\mathcal{E}_j - eF_0\left(l+\frac{w}{2}\right)\right)$$

$$\times\frac{k_BT}{2\pi\hbar}\ln\left(1+\exp\left(\frac{\epsilon_F + eF_0(l+w/2)-\mathcal{E}_j}{k_BT}\right)\right), \tag{3.9}$$

$$w^{(b)}(F_0) = \frac{8\hbar k_0k_1^2\alpha_0^2(k_0^2+\alpha_0^2)^{-1}\mathrm{e}^{-2\alpha_0 d}}{m^*(w+\alpha_0^{-1}+\alpha_1^{-1})(k_1^2+\alpha_0^2)}\theta\left(\mathcal{E}_1 - eF_0\left(l+\frac{w}{2}\right)\right) \tag{3.10}$$

where,

$$\epsilon_F = \frac{\hbar^2}{2m^*}(3\pi^2N_c)^{2/3}; \tag{3.11}$$

where N_c is the doping density in the emitter.

$$\hbar k_0 = \sqrt{2m^*(\mathcal{E}_j - eF_0(d+w))} \tag{3.12}$$

$$\hbar k_1 = \sqrt{2m^*\mathcal{E}_j} \tag{3.13}$$

$$\hbar\alpha_0 = \sqrt{2m^*(eV_b - \mathcal{E}_j + eF_0(d+w/2))} \tag{3.14}$$

$$\hbar\alpha_1 = \sqrt{2m^*(eV_b - \mathcal{E}_j - eF_0w/2)} \tag{3.15}$$

Similarly, the tunneling current to the collector is

$$J_{N\to N+1} \approx n_N w^{(f)}(F_N), \tag{3.16}$$

$$w^{(f)}(F) = \frac{8\hbar k_{N+1}k_N^2\alpha_N^2(k_N^2+\alpha_N^2)^{-1}\mathrm{e}^{-2\alpha_N d}}{m^*(w+\alpha_{N-1}^{-1}+\alpha_N^{-1})(k_{N+1}^2+\alpha_N^2)} \tag{3.17}$$

where

$$\hbar k_{N+1} = \sqrt{2m^*(\mathcal{E}_1 + eF_N(d+w))} \tag{3.18}$$

$$\hbar k_N = \sqrt{2m^*\mathcal{E}_1} \tag{3.19}$$

$$\hbar\alpha_{N-1} = \sqrt{2m^*(eV_b - \mathcal{E}_1 + eF_N(d+w/2))} \tag{3.20}$$

$$\hbar\alpha_N = \sqrt{2m^*(eV_b - \mathcal{E}_1 - eF_Nw/2)} \tag{3.21}$$

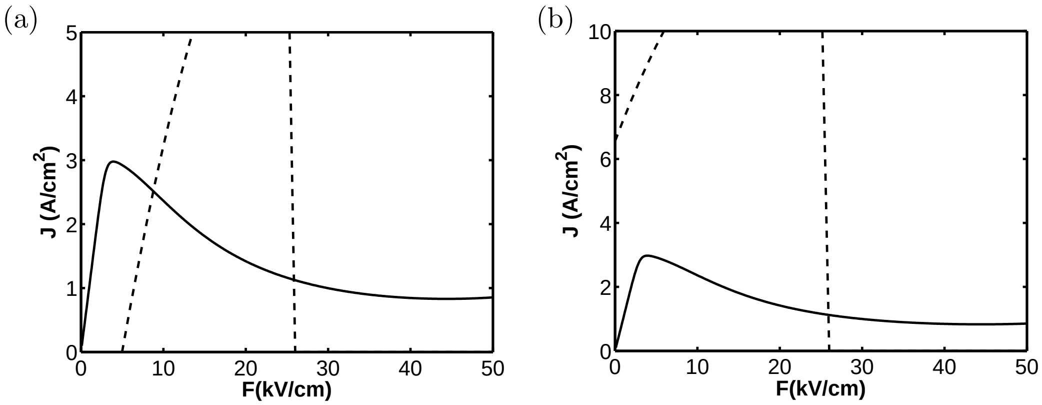

FIGURE 3.1: Dashed line: the tunneling current from the emitter to the first period for doping density in the emitter (a) $N_c = 1 \times 10^{18}\text{cm}^{-3}$ and (b) $N_c = 2 \times 10^{18}\text{cm}^{-3}$. Solid line: the intrinsic tunneling current inside the superlattice.

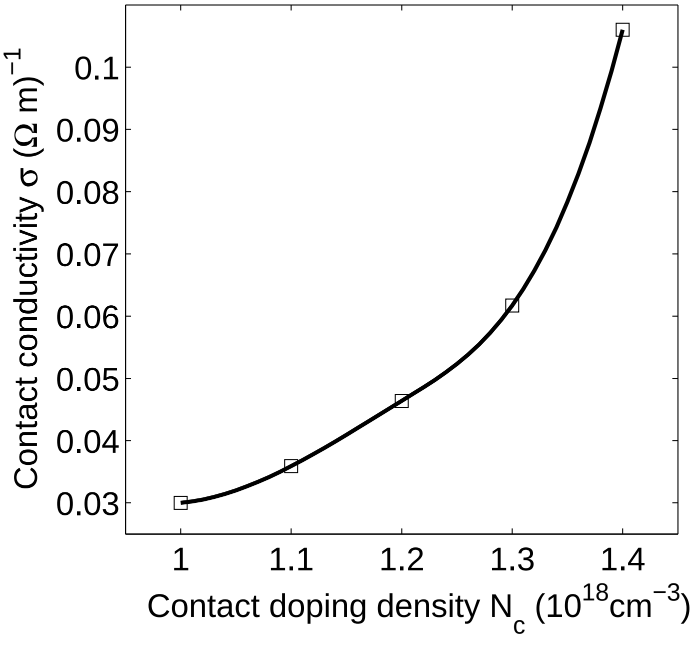

FIGURE 3.2: Effective contact conductivity versus N_c.

The tunneling current from the emitter to the first period is plotted in Fig. 3.1 for doping density in the emitter (a) $N_c = 1 \times 10^{18}\text{cm}^{-3}$ and (b) $N_c = 2 \times 10^{18}\text{cm}^{-3}$ along with the intrinsic tunneling current. A discrepancy between the two curves can be clearly seen. The emitter current intersects the intrinsic current for relatively small N_c and is higher than the intrinsic current for large N_c. If we approximate the emitter current with a straight line that intersects the intrinsic current at the same point as the detailed emitter model, we find that the behavior of the superlattice is qualitatively the same. So we can describe the emitter by a single parameter contact conductivity σ and the emitter can current can be written as

$$J_{0\to1} = \sigma F_0. \tag{3.22}$$

Similarly, the collect current is

$$J_{N\to N+1} = \sigma F_N \frac{n_N}{N_D}, \tag{3.23}$$

which also depends on the electron density in the last period. The values of contact conductivity corresponding to different emitter doping density are listed in Table 3.1 and also plotted in Fig. 3.2. It can be seen that the contact conductivity increases as doping density in the emitter increases.

N_c ($\times 10^{18}\text{cm}^{-3}$)	1.0	1.1	1.2	1.3	1.4
σ $(\Omega\text{m})^{-1}$	0.030	0.036	0.046	0.062	0.106

Table 3.1: Doping density values equivalent to contact conductivity σ values.

3.3 Dependence of time-averaged $I{-}V$ curves on contact conductivity

For larger values of σ, the $I - V$ curves typically exhibit as many stable current branches as there are superlattice periods. Each branch corresponds to the location of a single static charge accumulation layer in a particular quantum well of the superlattice. Typically, there is also multistability between adjacent branches. The overall electric field configuration has a high-field domain on the collector side of the superlattice and low-field domain on the emitter side of the superlattice. As the contact conductivity is lowered, the static domain configuration loses stability in favor of an oscillatory current. In many respects the overall behavior is qualitatively similar to that observed for superlattices in which the doping level of each period in the superlattice was lowered from a level that corresponds with intentionally doped structures to undoped structures.[55, 56] However, for very low values of σ the $I-V$ behavior is not similar to the case of very low doping level and one finds a high-field region next to the emitter contact as discussed below. We have calculated both *ramped* and *time-averaged* $I-V$ curves, and these two possess nearly identical form in regimes where the field profile is time-independent. The ramping procedure is as follows: the time step is 1.47 ns and total number of ramping steps from 0 V to 4 V and back to 0 V is 8×10^5, i.e. total ramping time is about 1.2 ms. The up and down sweeps show the presence of hysterisis. The time-averaged $I-V$ curves which we show in Fig. 3.3 below are calculated as follows: at every ramping step described above, the current is averaged over a period of time so long that the time-averaged current value converges, before proceeding the next voltage. This time is at least 14.7μs, much longer than oscillation periods (typically less than 1μs).

3.3.1 Current branches and field domains at high σ

For the highest value of σ studied here, the $I-V$ curves are composed of regularly-spaced, stable branches shown in Fig. 3.3(a). Each branch corresponds to a field configuration with a high field domain near the collector and a low field field domain near the emitter, illustrated in Fig. 3.4(a). The high field domain expands by one period when a new current branch forms. The field for upsweep in Fig. 3.3(a) as a function of period number and applied voltage is shown in Fig. 3.4(b). The two

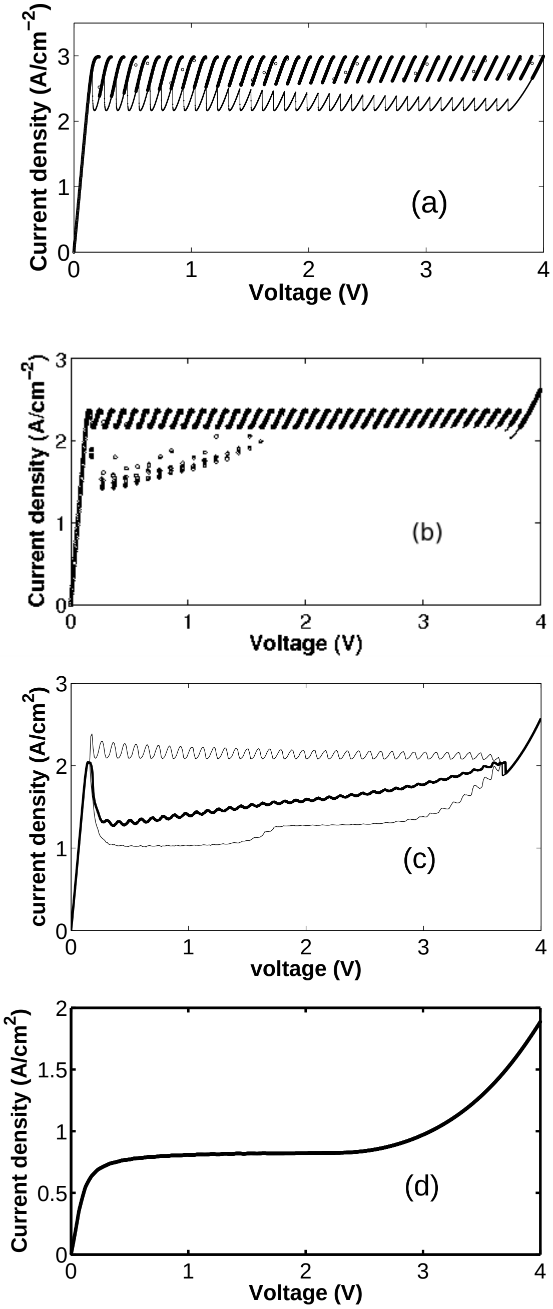

FIGURE 3.3: Time-averaged $I-V$ curves for different σ values: (a) $\sigma = 0.08(\Omega\text{m})^{-1}$, (b) $\sigma = 0.024(\Omega\text{m})^{-1}$, (c) $\sigma = 0.016(\Omega\text{m})^{-1}$, and (d) $\sigma = 0.00168(\Omega\text{m})^{-1}$. In (c) the thin curves show the envelope of extrema of the time-dependent current.

domains are separated by a charge accumulation layer that is mostly confined to two adjacent quantum wells. As the branch number increases by one, the center of the accumulation layer jumps by one period of the superlattice, i.e., to a quantum well that is one period closer to the emitter contact. The contour plot for electron density for upsweep as a function of period number and applied voltage is shown in Fig. 3.4(c).

A significant feature of the $I - V$ curve in Fig. 3.3(a) is that the upsweep curve does not match the downsweep curve. At certain ranges of the applied voltage, the upsweep current (upper branch) is larger than the downsweep current (lower branch). This is called bistability or hysteresis. This is because for these values of applied voltage, the CAL can either be one well or the next, corresponding to two different field configurations. An example is shown in Fig. 3.4(d) for 1 V. The CAL stays either in the 32nd well for upsweep or in the 31st well for downsweep. For higher voltages, tristability and multi-stability occurs.

3.3.2 Current self-oscillation

As σ decreases to intermediate values corresponding to Fig. 3.3(b), the stable current branches become smaller and gaps open up between them. In these gap regions there is no stable static field configuration and current self-oscillations occur which correspond to the periodic motion of the charge dipole layers across all or part of the superlattice. This behavior is similar to that reported by Hizanidis *et al.* for a distinct model of superlattice transport and different device parameters.[57] It is likely that the bifurcation diagram of superlattice current behavior versus σ reported in Ref. [57] is also applicable in our system. Finally, it is interesting to note that similar bifurcation behavior is found when the doping level is varied instead of σ, although in the case of intermediate doping levels, the current self-oscillations are associated with charge monopoles.[55]

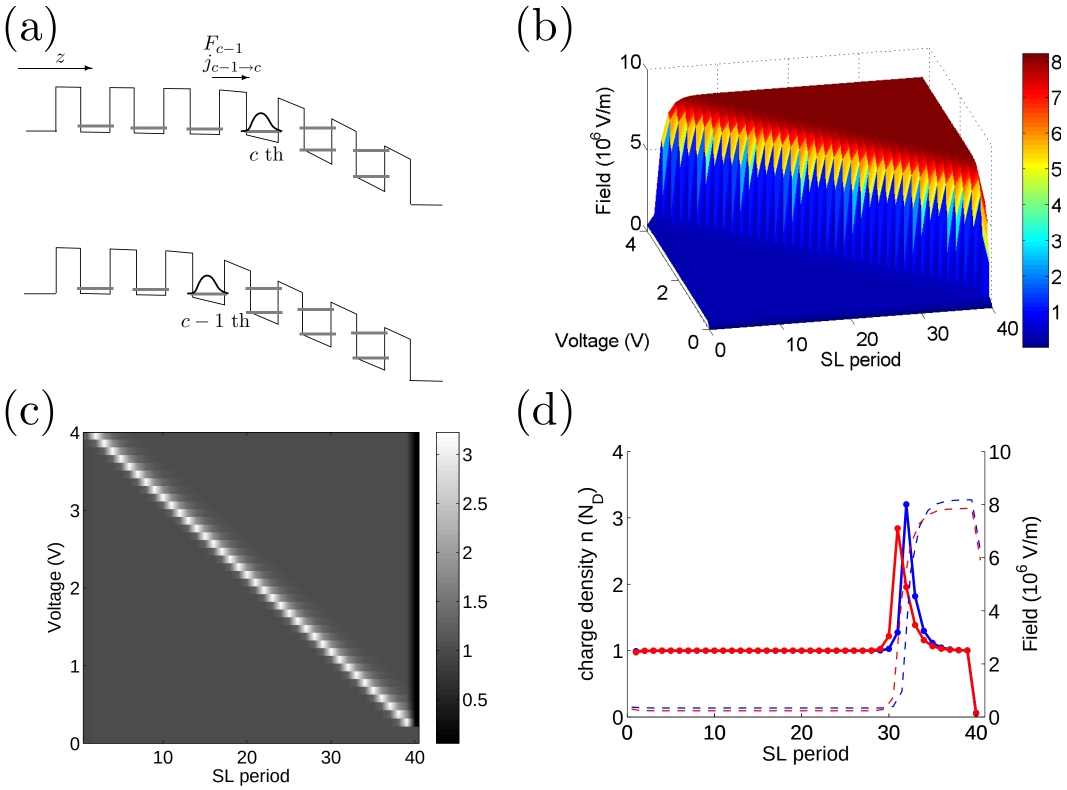

FIGURE 3.4: (a)Schematic of bistable field domains. (b) Field vs. voltage V and superlattice period for upward ramping. (c) Charge density n vs. voltage V and superlattice period for upward ramping. (d) Bistable field distribution and charge density distribution for $V = 1$ V.

For lower σ values corresponding the Fig. 3.3(c), the stable branches cease to exist and all the points on the plateau correspond to current self-oscillation, i.e., stable static electric field configurations do not occur for these σ values. The structure of the time-varying electric field profile is that of the dipole layer moving across the entire sample and then re-cycling and is similar to that found in previous studies.[57] The electron density evolution and the current traces at different bias voltages are plotted in Fig. 3.5. Although the current traces appear very different, there are some common features in electron density evolution. A charge depletion layer (CDL) followed by a CAL forms near the emitter and both move toward the collector. After CAL reaches the superlattice period where a CAL could build for high σ, the CAL

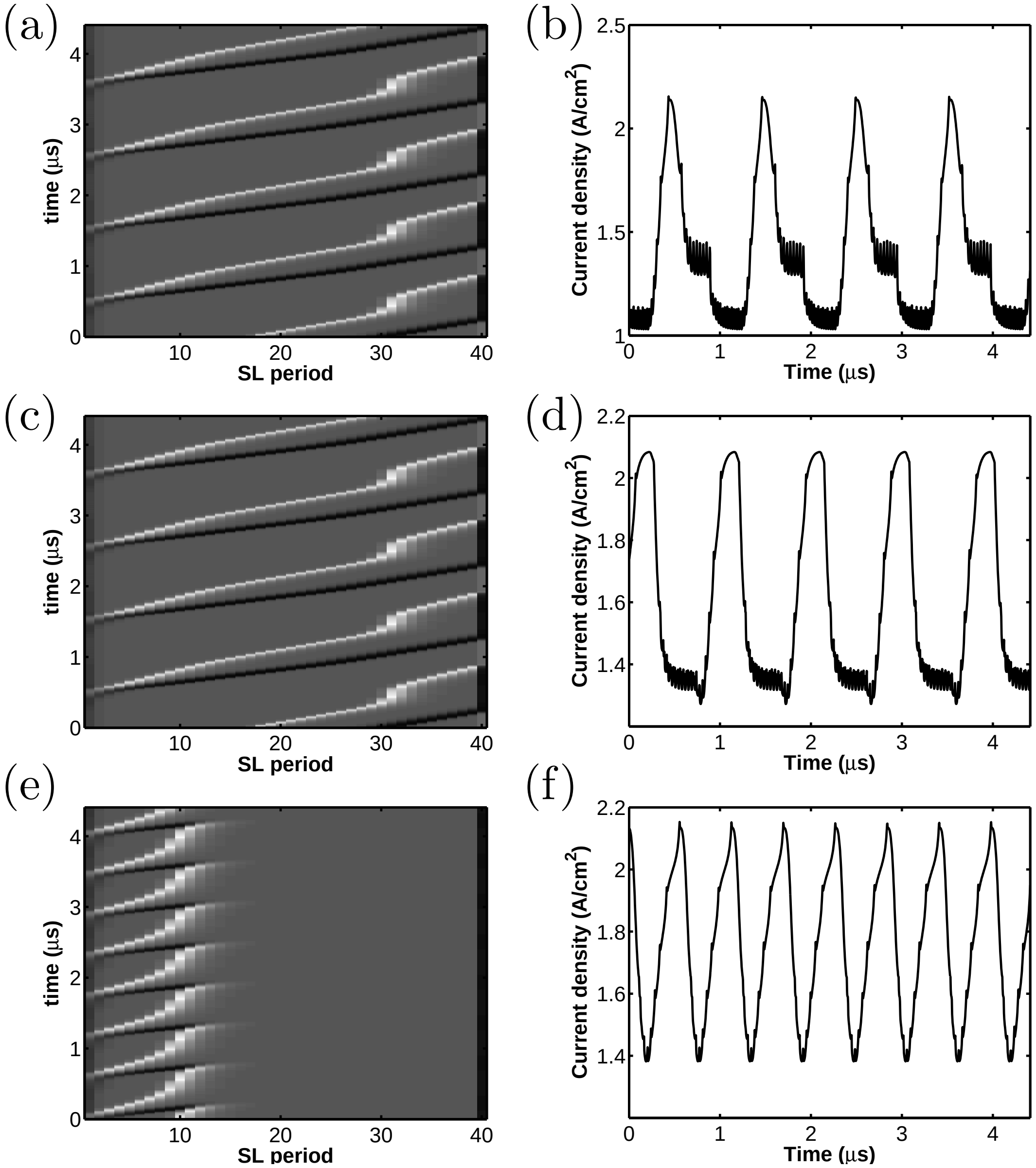

FIGURE 3.5: Current oscillations for $\sigma = 0.016(\Omega\text{m})^{-1}$ at (a),(b) $V = 1$ V, (c),(d) $V = 2$ V and (e),(f) $V = 3$ V. Left column: charge density contour plot. Right column: current time series.

stays at that position for a short period of time. During this time, the front CDL either has reached the collector for high voltages or has annihilated with an old CAL. Then the CAL failed to settle down, it continues to move toward the collector and a new CDL and CAL pair form at the emitter. This is a periodic process.

3.3.3 Extremely low σ

Fig. 3.3(d) shows a typical $I-V$ curve for very low σ value such that the contact characteristic sits below the intrinsic $J-F$ characteristic of the superlattice [cf. Fig. 1]. In this case, we find a stable $I-V$ curve without apparent branches or multistability. Remarkably, this corresponds to a stable, static electric field domain configuration in which the low field domain is adjacent to the collector and a non-constant high field region is adjacent to the emitter. These are separated by a *static* depletion layer that extends over three or more periods, shown in Fig. 3.6. Because the depletion layer has significantly lower absolute value of charge density than the accumulation layers described above, bistability is not expected or observed in this case. To our knowledge, such a field configuration has not been reported or predicted previously for weakly-coupled superlattices though there is evidence for such a field configuration in certain multiple-quantum well device structures.[58] This behavior can be understood by examining the time-independent continuum limit of the discrete rate equation model, Eqs. (2.34) and (2.36) which provides a good description provided that the spatial scale of electric field variation is not too rapid. We begin by approximating the field difference in Eq. (2.34) in terms of the spatial field derivative, i.e., $F_i - F_{i+1} \simeq l(\partial F/\partial x)_i$. Substituting this expression into Eq. (2.34) and solving for n_i allows us to write

$$n_i \simeq \frac{\varepsilon l}{e}(\partial F/\partial x)_i + N_D. \tag{3.24}$$

The current equation, Eq. (2.36), can be written in time-independent form as

$$\sigma F_0 = J_{i\to i+1}(n_i, n_{i+1}, F_i), \tag{3.25}$$

where we have dropped the displacement current and explicitly included the boundary current. Referring back to the expression for well-to-well tunneling current, Eq. (2.29), we see that, except for fields very close to zero, it is reasonable to include the drift term only so that $J_{i\to i+1}(n_i, n_{i+1}, F_I) \simeq e n_i v^f(F_i)/l$. [33] Now, substituting Eq. (3.24) into Eq. (3.25) and using the aforementioned drift approximation, we arrive at a first-order differential equation for the static field profile

$$\frac{e}{l}[\frac{\varepsilon l}{e}(\partial F/\partial x) + N_D]v^f(F) = \sigma F_0. \tag{3.26}$$

The numerical results are easier to interpret if we write this equation in terms of $\partial F/\partial x$ as follows

$$\frac{\partial F}{\partial x} = \frac{e N_D}{\varepsilon l}(\frac{\sigma F_0}{J_{superlattice}(F)} - 1), \tag{3.27}$$

where we have used the drift limit of the superlattice current-field characteristic under uniform field conditions, $J_{superlattice}(F) \simeq e N_D v^f(F)/l$. Equation (3.27) provides a good qualitative description of the key features in the field profile of Fig. 3.6. For instance, the field profile can be calculated by integrating Eq. (3.27) from $x = 0$ (i.e., the injecting contact) into the sample, subject to a boundary condition $F(x = 0) = F_0$, where F_0 is ultimately to be determined in terms of the total applied voltage, i.e., $V = \int_0^{Nl} F(x)dx$. In the limit of small σ such that $|\sigma F_0| < |J_{superlattice}(F)|$ we see immediately (from the right hand side of Eq. (3.27)) that only regions of depleted charge are possible. Furthermore, the magnitude of depleted charge will be maximal when $|J_{superlattice}(F)|$ is largest, and this explains the appearance of the predominant depletion layer in the range of wells 17 to 20. The structure of Eq. (3.27) also explains why the field profile is not constant in the high field region between the emitter and the depletion layer: for sufficiently small σ, we have $|\sigma F_0| < |J_{superlattice}(F)|$ throughout this range of fields and there is a non-zero charge density in this region (corresponding to depletion of electrons) that is approximately uniform - since $J_{superlattice}(F)$ is approximately constant for these field values, cf. Fig. 1. Furthermore, Eq. (3.27) gives insight into the shape of the $I-V$ curve at low σ,

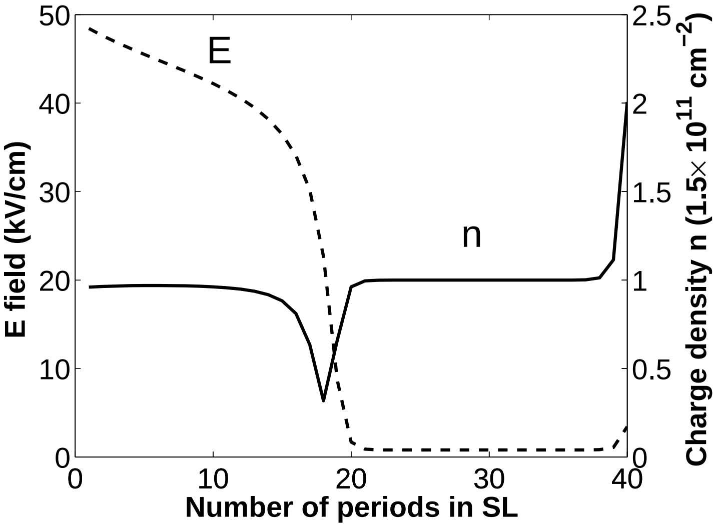

FIGURE 3.6: The spatial profiles of electric field and charge density for applied voltage $V = 1$ Volt and contact conductivity $\sigma = 0.00168(\Omega \mathrm{m})^{-1}$. A static charge depletion layer seperates the high field region next to the emitter and the low field domain next to the collector.

cf. Fig. 2(d). The plateau occurs because for this range of applied voltages, the boundary field F_0 is almost constant with increasing voltage; the increasing voltage is achieved by the shifting the position of the depletion layer towards the collector.

Equation (3.27) also allows us to see why the low σ behavior reported here is different from that previously reported for low doping level or, equivalently, for small values of N_D.[55, 33] For σ fixed at a moderately large value, Eq. (3.27) implies the presence of charge accumulation layers, *regardless* of the value of N_D. When N_D is small this leads to stable, static field profiles and $I - V$ curves that are proportional the local superlattice current-field characteristic.[55]

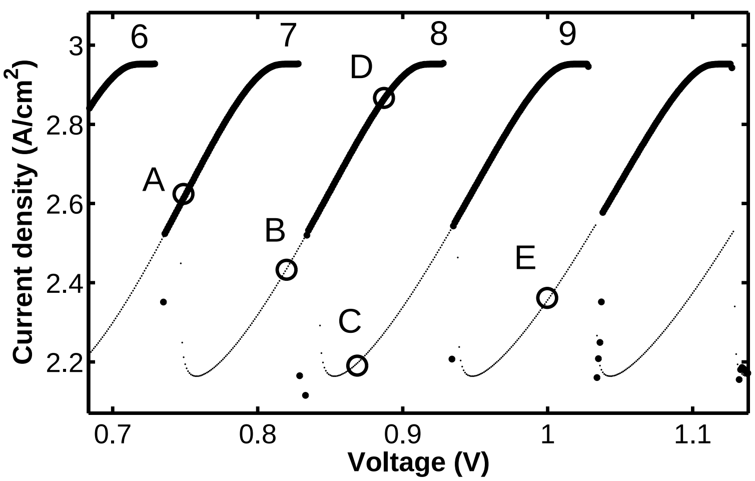

FIGURE 3.7: Initial voltage (A) and successive final voltages (B, C, D, and E) indicated on the $I - V$ curve for $\sigma = 0.064(\Omega\text{m})^{-1}$.

3.4 Dependence of Relocation Type on contact conductivity and Voltage Step

We now consider the response of electric field profiles and associated current transients to abrupt steps in applied voltage. We focus on a contact conductivity value $\sigma = 0.064(\Omega\text{m})^{-1}$ (which is slightly below the characteristic value defined above, i.e., $\sigma_c \equiv J_M/F_M = 0.07924(\Omega\text{m})^{-1}$) and nearby values for which static field domains are stable under time-independent voltage bias. In Fig. 3.7 we indicate the initial dc voltage by the point A and then points B, C, D, and E correspond to the successive final voltages in the following discussion.

The transition from point A (0.75 V) to point B (0.82 V) exhibits the injected dipole process with relatively complex spatio-temporal structure and long relocation time t_r. The corresponding current transient behavior and space-time evolution of the net charge density are shown in Fig. 3.8. The voltage step causes a current jump which injects electrons into the superlattice. Prior to the voltage step, there is a small depletion layer at the emitter due to the higher field in the emitter contact;

the injected electrons form between the contact and the depletion layer, pushing the depletion layer into the sample. At the same time, the initial accumulation layer jumps back one well, from well number 34 to 33. Then, the small dipole configuration detaches from the emitter and moves into the superlattice. For the particular conditions shown here it remains small amplitude (so that it is not visible on the gray scale of Fig. 3.8(b)) and moves at a steady velocity for the first 0.1 μsec after the voltage step; during this time, the initial accumulation layer remains at a fixed in well number 33 and the current has a large, approximately constant value. After this initial behavior, the dipole layer grows rather abruptly into a moving, fully developed dipole. The initial accumulation layer detaches from well number 33 and begins to move towards the collector at the same speed as the accumulation part of the injected dipole. The current drops to a new approx. steady value during this interval - from roughly 0.2 to 0.4 μsec in Fig. 3.8(a). The small rapid oscillations in current are due to the motion of the large-amplitude accumulation layers between adjacent wells and these have been discussed previously.[46, 45] These three charge layers move toward the collector and the foremost two layers disappear successively at the collector. Finally, the injected accumulation layer stops at the new position (i.e., well number 33) forming the stable field configuration that corresponds to the final voltage. It should be noted that this injected dipole is slightly different than that described in Ref. [45]. In that case, a smaller assumed σ value led to the appearance of the fully-developed injected dipole beginning at the emitter contact. Additionally, we note that the overall shape of the current transient reflects the prevalence of dipole motion and is similar to that which occurs in the bulk Gunn effect. [59, 60]

As the voltage step size increases there is a smooth transition to the next scenario, in which the injected dipole layers become smaller and move faster. Thus, the relocation time becomes smaller as shown in Fig. 3.9 which corresponds to a voltage jump from point A (0.75 V) to point C (0.86965 V) in Fig. 3.7. In this case the final

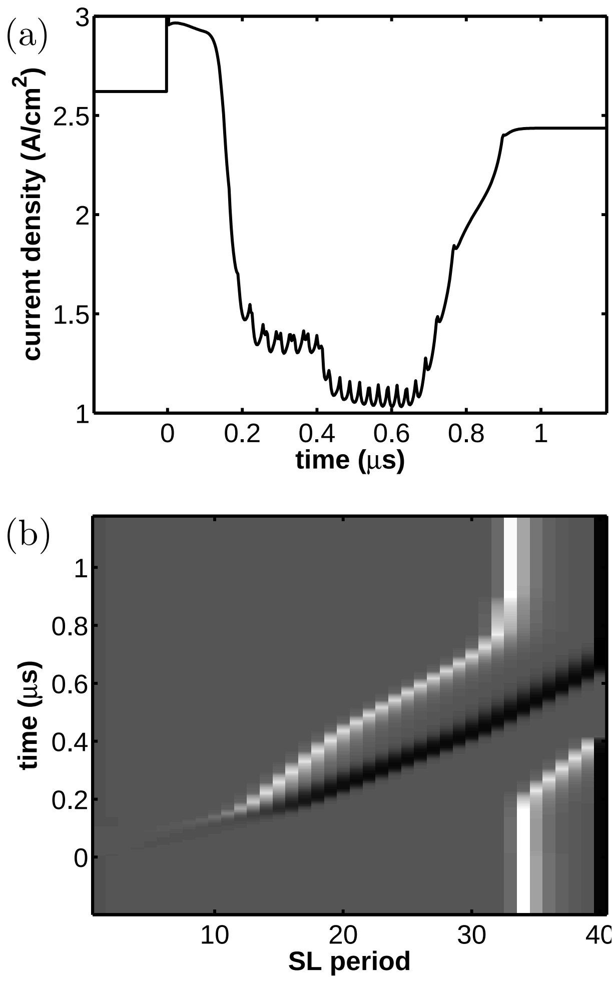

FIGURE 3.8: Injected dipole relocation mechanism for $\sigma = 0.064(\Omega\text{m})^{-1}$: (a) transient current response, and (b) space-time portrait of charge density. Voltage switches from 0.75 V to 0.82 V (cf. point B in Fig. 3.7).

accumulation layer is at well number 32, two steps closer to the emitter than the initial position. This faster behavior is a direct consequence of the larger voltage step which implies the injection of more electrons. This, in turn, leads to more complete filling of the depletion layer at the emitter resulting in a smaller charge dipole at the emitter. It also can be seen that a small charge layer moves faster than a fully developed one. This can be understood because for a smaller overall charge value in either the accumulation or depletion layer there is less charge to tunnel through

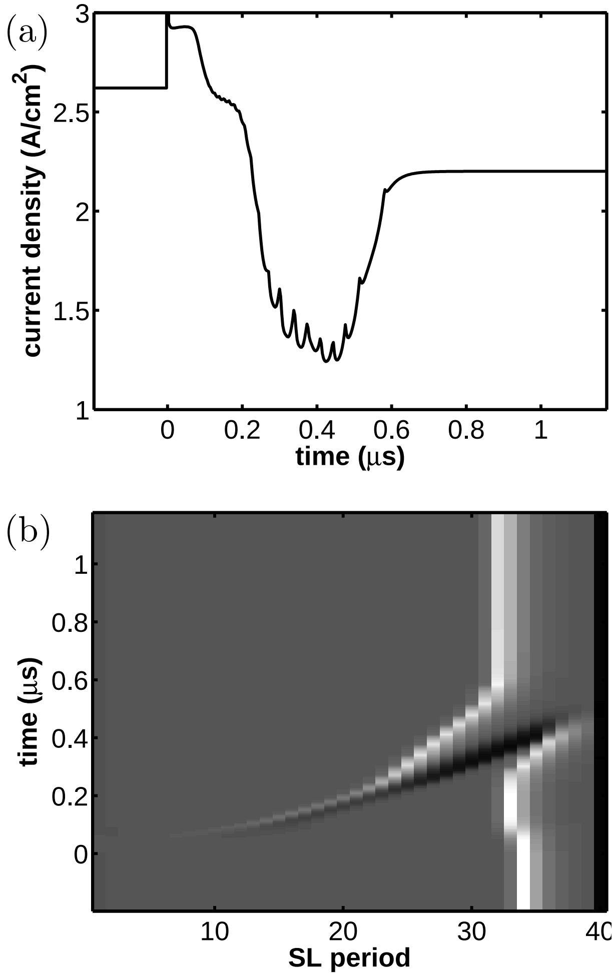

FIGURE 3.9: Shortened injected dipole relocation mechanism for $\sigma = 0.064(\Omega\mathrm{m})^{-1}$: (a) transient current response, and (b) space-time portrait of charge density. Voltage switches from 0.75 V to 0.86965 V (cf. point C in Fig. 3.7).

each barrier and the motion is therefore faster.

Further increasing the voltage step, we can see the single monopole shift mechanism shown in Fig. 3.10, which corresponds to a voltage step from point A (0.75 V) to point D (0.88 V) in Fig. 3.7. In this scenario, the injected electrons have almost completely filled the depletion layer at the emitter and the fluctuation is so small that it simply dies out as it begins to move into the superlattice. The original accumulation layer just moves backward by one period and the whole system reaches

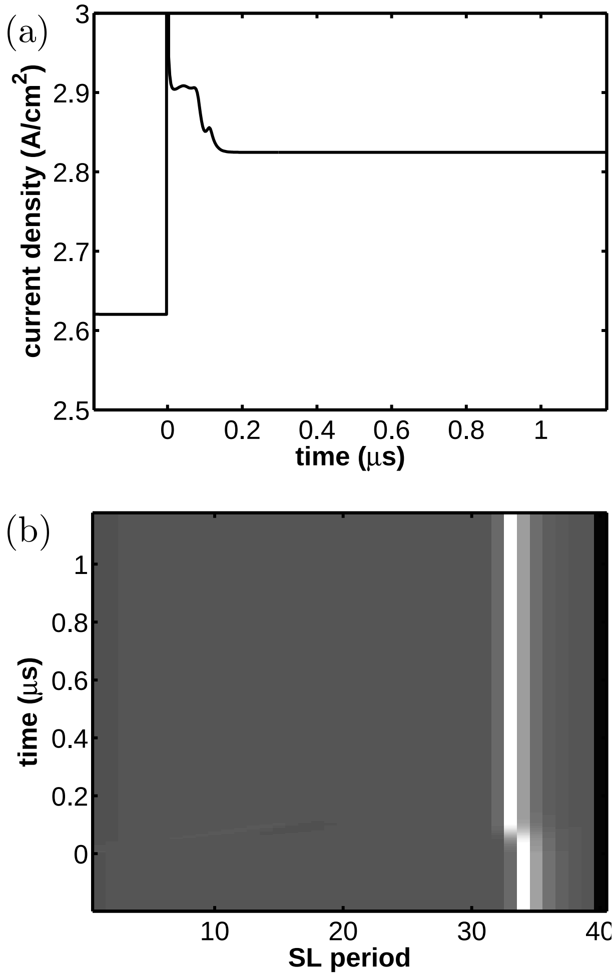

FIGURE 3.10: Single monopole shift $\sigma = 0.064(\Omega\mathrm{m})^{-1}$: (a) transient current response, and (b) space-time portrait of charge density. Voltage switches from 0.75 V to 0.88 V (cf. point D in Fig. 3.7).

a stable state. This process is the simplest and the relocation time is the smallest.

At a large voltage step size that takes the system across two current branches (corresponding to the transition from point A (0.75 V) to E (1.00 V) in Fig. 3.7), we observe an *injected monopole* shown in Fig. 3.11. The large number of injected electrons rapidly fill the depletion layer at the emitter contact and a small accumulation layer is formed at the emitter. This accumulation layer moves rapidly into the superlattice and comes to rest at the new stable position. The original accumulation layer simply shrinks and disappears. The relocation time of this process is also relatively short. The initial motion of the small accumulation layer is rapid and it gradually slows as its amplitude increases to the final stable value. At the same time, the current response is strikingly different than that for dipole motion. The overall waveform that drops smoothly as the accumulation layer moves into the sample and then rises as the accumulation layer reaches its final location; the intervals of approximately steady current response associated with dipole motion are absent. This behavior is similar to that observed in studies of the bulk Gunn effect in which moving dipole domains were found to give time-periodic current with flat intervals, while moving monopoles were associated with a more sinusoidal current oscillation.[59, 60]

To get a complete picture of the dependence of relocation mechanism and relocation times on contact conductivity, we have computed the relocation time for an entire range of σ and V_{step} values; the results are summarized in Fig. 3.13. For this figure, the initial voltage is 0.75 V and is in the middle of the 7th branch on the $I-V$ curve. An overall feature of this diagram is that we observe a series of three plateaus with increasing V_{step}. The first plateau, with small V_{step} and independent of σ, corresponds to voltage switching on the same branch in which domain relocation occurs via single monopole shift and is rapid. On the second step, the voltage step crosses one current branch and there is a plateau of long relocation time corresponding to the injected dipole for smaller values of σ; however, the relocation time drops sharply for larger values of σ, indicating suppression of the injected dipole for σ values above a characteristic value $\sigma^* \approx 0.072(\Omega\text{m})^{-1}$. While this transition is **not** an abrupt bifurcation point in σ, it does occur over a relatively narrow range of σ values which correspond approximately with the σ value where the contact characteristic no longer intersects the $J-F$ curve in the NDC region, cf. Fig. 1 the σ_c value. This suppression occurs because the depletion layer at the emitter becomes small for large

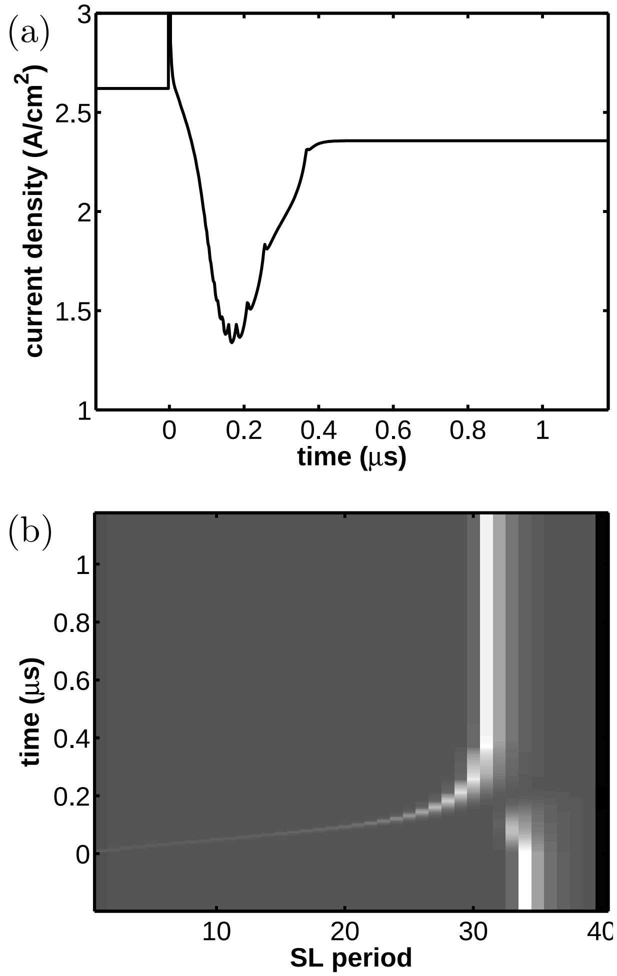

FIGURE 3.11: Injected monopole relocation mechanism for $\sigma = 0.064(\Omega\text{m})^{-1}$: (a) transient current response, and (b) space-time portrait of charge density. Voltage swiches from 0.75 V to 1.00 V (cf. point E in Fig. 3.7).

σ values so that even a small amount of injected electrons associated with V_{step} can fill the depletion layer before it has a chance to propagate into the superlattice. The third step mostly consists of shorter relocation time behavior corresponding to the injected monopole mechanism. These fast transient response for large voltage steps are confirmed in the recent experiments carried out on samples with large contact conductivity[61]. Figure. 3.12(b) shows such a measured current response which has the same order of magnitude of response time. However, there is a small part of the lower lefthand corner of the third step where injected dipole behavior is observed and this becomes more prominent for σ values below those shown.

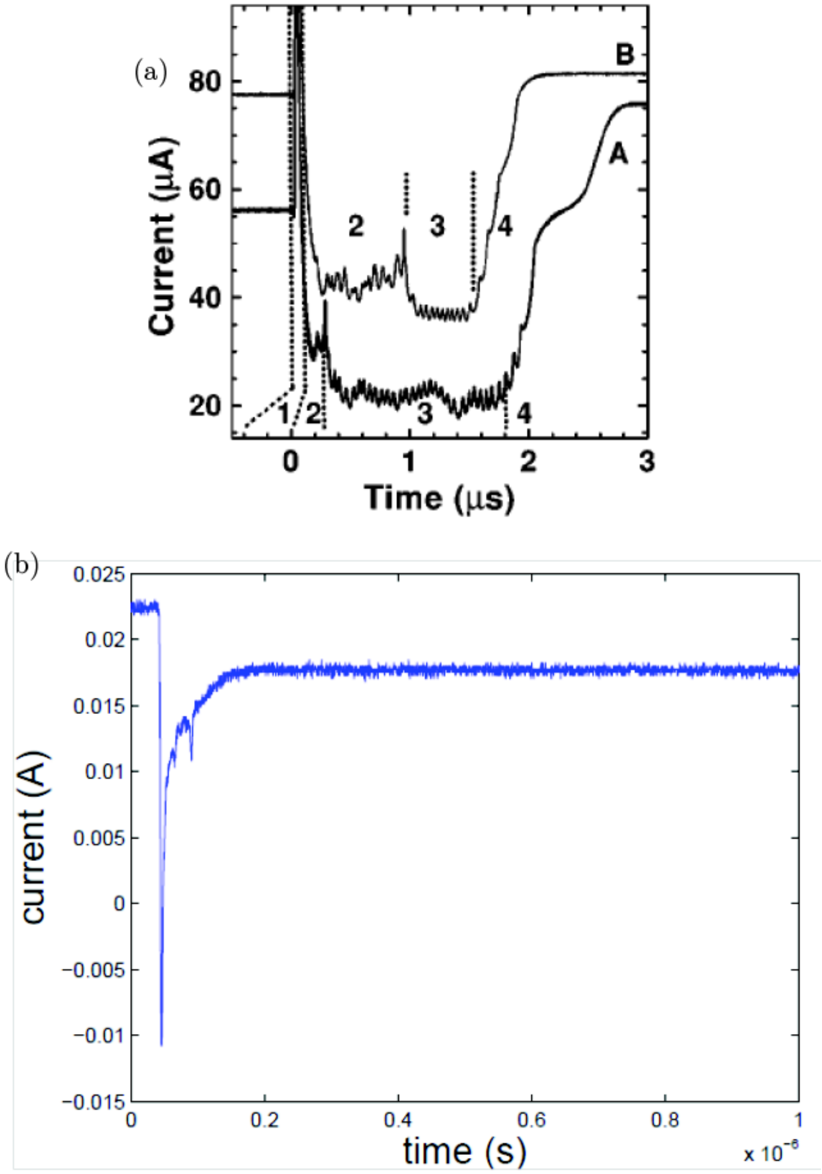

FIGURE 3.12: Measured current response for large voltage step switching and (a) low contact conductivity (from Ref. [46]) (b) high contact doping 2×10^{18} cm^{-3} corresponding to a high contact conductivity, $\sigma > 0.1(\Omega\text{m})^{-1}$, [61] see Fig. 3.2.

The wall separating the plateau and the first step indicates steady small-amplitude current oscillation behavior that typically occurs at the ends of static current branches.

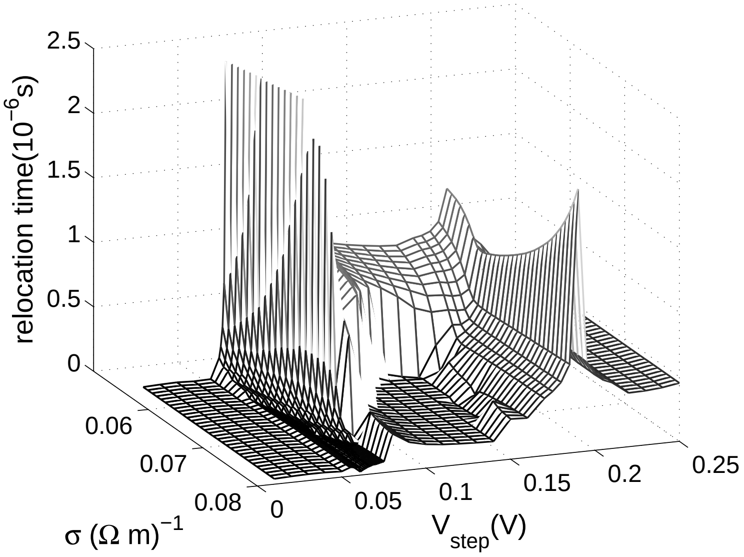

FIGURE 3.13: Dependence of relocation time on voltage step V_{step} and contact conductivity σ. Initial voltage is 0.75 V.

This behavior was first reported in Ref. [47] and corresponds to steady-state oscillation of the accumulation layer between adjacent wells. It is interesting to note that this behavior also ceases for σ values above σ^* implying that the current branches do not end in small-amplitude oscillations for sufficiently large σ. On the other hand, the ridge between the second and the third steps - which results from metastable behavior during switching and produces a delayed shift - becomes more pronounced for larger σ. This behavior gives rise to non-trivial stochastic switching effects that have been studied experimentally and theoretically.[62, 63] We also note a prevalence of injected monopole behavior for values of σ in excess of the characteristic value σ_c. This behavior is analogous to that found in earlier work on the bulk Gunn effect in which periodically moving dipoles were associated with lower values of σ (i.e., $\sigma < \sigma_c$) while periodically moving charge monopoles were associated with large values of σ (i.e., $\sigma \gtrsim \sigma_c$).[59]

3.5 Conclusion

We have studied how contact conductivity σ, characterizing the boundary condition for the sequential tunneling model, affects the time-averaged $I-V$ characteristics of weakly-coupled superlattices and their response to sudden switching of the applied voltage. We find that for relatively large σ values the $I-V$ curves exhibit static, multistable branches that reflect the presence of a static charge accumulation layer that separates the sample into low- and high-field domains. For intermediate values of σ the $I-V$ curves reflect the presence of current self-oscillations which are due to the periodic motion of charge dipole layers across portions of the sample. Finally, at very small σ the $I-V$ curve is a stable curve without branches, and reflects an inverted static field configuration in which the high field domain is next to the emitter. The overall trend in σ-dependent behavior is seen to result from the role of the contact in setting a limit on the quantity of electrons that enter the superlattice. While there are some similarities between σ dependence and doping density dependence studied previously [55, 56] for large and intermediate conductivity values, the behavior for very small σ is distinct from that occuring for small doping density.

Relocation response to a range of σ values and voltage step values V_{step} is characterized by studying the relocation time t_r and shows that the injected dipole occurs only for a specific range of σ values (within the multistable $I-V$ range) and small V_{step}. Transitional regions are found to occur between different relocation types. A figure of relocation time versus σ and V_{step}, serving as a phase diagram for different relocation types, has been plotted and discussed. The dependence of relocation types on both σ and V_{step} results from the crucial role these two factors play in determining the quantity of electrons that are injected into the superlattice through the emitter contact.

4

The weakly-coupled superlattice with a shunting side layer

In Chapter 3, we have seen that the superlattice with negative differential conductivity is a nonlinear medium having rich front dynamics and nonuniform field domains. A question arises: how can we control front behavior in such a system? More specifically, can we suppress the fronts in such a media? In other words, can one stabilize a spatially uniform electric field distribution in the superlattice? A direct application of this capability of suppressing fronts is the superlattice-based THz oscillator, which we will investigate in next Chapter.

We propose a structure of a weakly-coupled superlattice with a shunting layer grown on its side. This opens a parallel channel connected the superlattice at each quantum well. The idea of using the shunt to suppress space-charge instability first appeared in Ref. [64]. However, their oversimplified model was not able to show rich dynamics in this structure. In this Chapter, a model is first proposed and rich electronic transport dynamics in this system is studied. Additionally, we are able to determine a maximum lateral size for which a uniform electric field is stabilized by a shunt layer.

4.1 Laterally extended model of the superlattice with shunt layer

The dynamical properties of weakly-coupled semiconductor superlattices have been successfully described by the sequential resonant tunneling model over the past several years.[65, 32, 33, 44] However, previous works usually consider only the dynamics along the growth (vertical) direction of the superlattice and ignore the dynamics in the in-plane (lateral) direction, i.e., treat each period as an infinitely large plane with uniform charge density. More recently, Amann *et al.*[66] developed a theoretical framework which describes both lateral and vertical electronic dynamics. Here, we extend this framework to include the effects of a shunting side layer.

The structure of the shunted superlattice is shown in Fig. 4.1. Each quantum well forms a slab that is parallel to the $x-y$ plane, with cross sectional dimensions L_x and L_y. There are N such quantum wells stacked on top of each other in the z direction, sandwiched between an emitter layer and a collector layer. The shunt layer is located between $-\delta_x \leq x \leq 0$, with thickness δ_x. The superlattice period is $l = w + d$, where w and d are the width of the quantum well and width of the barrier, respectively. The external voltage is applied in the z direction, across the emitter and the collector.

4.1.1 The laterally extended model for superlattice

Inside the superlattice, the electrons are localized within one quantum well due to the relatively thick quantum barriers. Furthermore, the electrons are assumed to be at local equilibrium and the local *two-dimensional* charge density at time t is denoted by $n_m(x, y, t)$, where m is the well index, x, y are the in-plane coordinates. The charge continuity equation in the superlattice can be written as:

$$e\,\dot{n}_m(x, y, t) = j_{\parallel m-1\to m} - j_{\parallel m\to m+1} - \nabla_\perp \cdot \mathbf{j}_{\perp m}, \qquad (4.1)$$

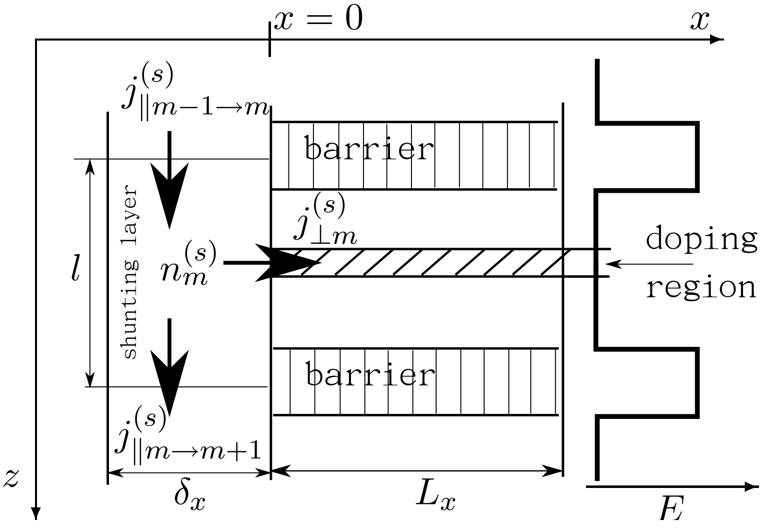

FIGURE 4.1: Schematic of the shunted superlattice. The growth direction is along the z direction and the quantum wells are parallel to the x direction. The superlattice is located at $x > 0$ and the shunt is at $x < 0$. The thick line on the right is the potential energy of an electron in the conduction band of the superlattice.

where

$$\nabla_\perp = \mathbf{e}_x \frac{\partial}{\partial x} + \mathbf{e}_y \frac{\partial}{\partial y}, \tag{4.2}$$

and $j_{\|m-1\to m}$ denotes the three dimensional vertical current in z direction tunneling through each barrier (units: [A/m^2]) and $\mathbf{j}_{\perp m}$ is the lateral two-dimensional current density (units: [A/m]). The electron charge is $e < 0$. The y-dependence is ignored and Eq. (5.2) can be rewritten as:

$$e\,\dot{n}_m(x,t) = j_{\|m-1\to m} \; - \; j_{\|m\to m+1} \; - \; \frac{\partial j_{\perp m}(x)}{\partial x}. \tag{4.3}$$

The local vertical tunneling current $j_{\|m\to m+1}$ through each barrier is described by the sequential resonant tunneling model which has been derived using different methods;[32, 33, 44] in this paper, we have used the same form as in Refs. [33, 44]. This tunneling current depends on the electric field $F_{\|m}(x)$ across the barrier through which the tunneling occurs and the electron charge densities $n_{m-1}(x)$ and $n_m(x)$ in the neighboring quantum wells of this barrier. Thus, the tunneling current has the functional form:

$$j_{\|m-1\to m}(x) = j_{\|m-1\to m}[F_{\|m}(x), n_{m-1}(x), n_m(x)]. \tag{4.4}$$

If the charge density is uniform, the tunneling current $J_{\|}(F, N_D, N_D)$ follows the dash-dot curve in Fig. 4.3b. The conductivity peak is due to resonant tunneling between non-equivalent levels in adjacent wells. The negative conductivity part is due to non-resonant tunneling of electrons when the applied field across the barrier is high enough such that the ground levels in neighboring quantum wells mismatch. The tunneling current densities through the emitter and collector layers are modeled by Ohmic boundary conditions,[66] that is, $j_{\|0\to 1}(x) = \sigma F_{\|0}(x)$, and $j_{\|N\to N+1}(x) = \sigma F_{\|N}(x) n_N/N_D$, with contact conductivity σ and two-dimensional doping density N_D in each well.

The lateral dynamics is caused by the in-plane current $\mathbf{j}_{\perp m}$ which consists of a drift part and a diffusion part. When the y-dependence is ignored, this becomes

$$j_{\perp m}(x) = -e\mu n_m F_{\perp m} - eD_0 \frac{\partial n_m}{\partial x} \tag{4.5}$$

where $F_{\perp m}(x)$ is the in-plane component of the electric field at x in well m, μ is the mobility and D_0 is the diffusion coefficient. The generalized Einstein relation [67] establishes the connection between μ and D_0 for arbitrary two-dimensional electron densities including the degenerate regime:

$$D_0(n_m) = \frac{n_m}{-e\rho_0(1 - \exp[-n_m/(\rho_0 k_B T)])}\mu \tag{4.6}$$

with the two-dimensional density of states $\rho_0 = m^*/(\pi\hbar^2)$, where m^* is the electron effective mass. Here we assume that μ and D_0 are fixed.

Both the lateral and vertical currents depend on the electrical fields which in turn depend on the scalar potential $\phi_m(x, y)$. The potential can be solved by the Poisson equation

$$\Delta\phi_m(x,y) = (\Delta_\perp + \Delta_\parallel)\phi_m(x,y) = -\frac{e}{l\epsilon_r\epsilon_0}(n_m - N_D), \tag{4.7}$$

with

$$\begin{aligned}
\Delta_\perp\phi_m(x) &= \frac{\partial^2}{\partial x^2}\phi_m(x), && (4.8)\\
\Delta_\parallel\phi_m(x) &= \frac{\phi_{m-1}(x) - 2\phi_m(x) + \phi_{m+1}(x)}{l^2}, && (4.9)
\end{aligned}$$

where ϵ_r and ϵ_0 are the relative and absolute permittivity, respectively. Then the field can be calculated as

$$\begin{aligned}
F_{\parallel m}(x,y) &= \frac{\phi_{m+1}(x) - \phi_m(x)}{l},\\
F_{\perp m}(x) &= -\frac{\partial\phi_m(x)}{\partial x}. && (4.10)
\end{aligned}$$

Here we solve the Poisson equation using an approximation method assuming that the typical structures in the lateral direction vary on a length scale much longer than the mean free path of the degenerate electrons.[66]

4.1.2 The shunt

The drift-diffusion dynamics of the shunting layer is similar to that of the lateral dynamics within each superlattice quantum well. First, we neglect x-dependence in the shunt, that is, the shunt is collapsed into a single layer along the z-direction. Note also that unlike the superlattice, which possesses an intrinsic discreteness along z direction, the shunt is a continuous layer. Therefore, we make a further approximation that the shunt is divided into blocks aligned with the periods of the superlattice and that the charge density is locally uniform within each block. This assumption not only provides the discretization required by numerical simulation, but also matches the dynamics of the shunt with that of the superlattice. With these two assumptions, we can write down the continuity equation in the m-th shunt block as follows:

$$e\,\dot{\tilde{n}}_m^{(s)}(t)\cdot\delta_x\,l\,L_y = j^{(s)}_{\parallel m-1\to m}\cdot\delta_x\,L_y\;-\;j^{(s)}_{\parallel m\to m+1}\cdot\delta_x\,L_y\;-\;\tilde{j}^{(s)}_{\perp m}\cdot l\,L_y, \tag{4.11}$$

where the superscript (s) denotes the quantities in the shunt and the tilde denotes that the quantities are three-dimensional, i.e.,

$$n_m^{(s)} = \tilde{n}_m^{(s)}\cdot l;\quad j^{(s)}_{\perp m} = \tilde{j}^{(s)}_{\perp m}\cdot l. \tag{4.12}$$

Here, the quantity $j^{(s)}_{\perp m}$ denotes the lateral current that flows between the shunt and the superlattice through their interface. Then we can write Eq. (4.11) in the form:

$$e\,\dot{n}_m^{(s)}(t) = j^{(s)}_{\parallel m-1\to m}\;-\;j^{(s)}_{\parallel m\to m+1}\;-\;\frac{j^{(s)}_{\perp m}}{\delta_x}, \tag{4.13}$$

Note that the vertical current in the shunt has a very different form than the tunneling current in the superlattice. It follows a similar dynamics as the in-plane current in the superlattice quantum wells and is related to the three-dimensional charge density in the shunt:

$$j^{(s)}_{\parallel m-1\to m} = -e\mu\tilde{n}_m^{(s)}F^{(s)}_{\parallel m} - eD_0\frac{\partial\tilde{n}_m^{(s)}}{\partial z}. \tag{4.14}$$

Here we assume the mobility μ and the diffusion coefficient D_0 have the same values as in the superlattice.

Next, we examine the lateral current that connects the shunt and the quantum well layer within the superlattice:

$$j^{(s)}_{\perp m} = -e\mu n_m(x=0)F_{\perp m} - D_0\nabla_\perp n_m\Big|_{x=0^+}. \tag{4.15}$$

In this equation, the boundary should be defined at $x = 0^+$ for calculation of both the current and the potential in the shunt. Since the shunt is assumed to be uniform in x direction, defining the above equation at $x = 0^-$ implies that $F_{\perp m}$ and $\nabla_\perp n_m^{(s)}$ are zero which would lead to zero boundary current. Another advantage of choosing the boundary at $x = 0^+$ is that the potential in the shunt should be equal to the potential in the superlattice close to its boundary, i.e., $\phi_m^{(s)}(x < 0) = \phi_m(x = 0^+)$, since the potential is continuous everywhere. This relation allows us to equate the potential in the shunt with that at the inner boundary of the superlattice. So the potential at the boundary of the solution of Eq. (4.7) is just the potential in the shunt. The fields required to calculate the current in Eq. (4.15) can be obtained by

$$\begin{aligned} F_{\parallel m}^{(s)}(x) &= \frac{\phi_{m+1}^{(s)}(x) - \phi_m^{(s)}(x)}{l}, \\ F_{\perp m}(0^+) &= -\nabla_\perp \phi_m(x)\Big|_{x=0^+}. \end{aligned} \tag{4.16}$$

The charge density and its normal gradient at the boundary are

$$n_m(x = 0) = \frac{n_m(0^+) + n_m^{(s)}(0^-)}{2}, \tag{4.17}$$

$$\nabla_\perp n_m\Big|_{x=0^+} = \lim_{\Delta x \to 0^+} \frac{n_m(\Delta x) - n_m^{(s)}}{\Delta x}. \tag{4.18}$$

4.1.3 Connectivity

Here we also note the possible effects of energy band structure of the shunted superlattice and the doping density in the shunt. In the above discussion, the situation has been simplified because no band bending is included. However, variations in doping densities in the shunt and the superlattice can cause band bending effects at the interface. Even if the shunt is doped to have the same Fermi level as that in the superlattice so that little band bending might be expected, there are other issues that impact the connection quality between the shunt and the superlattice, for example, surface roughness and the presence of trap states or a thin oxide layer.

On the other hand, these effects can be minimized through the use of a fabrication process such as cleaved edge overgrowth which is known to produce very high quality interfaces.[68, 69] To quantify the quality of the connection between the superlattice and the shunt, we introduce a parameter $0 \leq a \leq 1$ such that $a = 1$ corresponds to a perfect connection and $a = 0$ corresponds to no connection. This leads to the following modification of Eq. (4.15):

$$j_{\perp m}^{(s)} = a \cdot \left(-e\mu n_m(x=0) F_{\perp m} - D_0 \nabla_{\perp} n_m \bigg|_{x=0^+} \right). \tag{4.19}$$

Here we note that the determination of a values for specific interface types would be a separate theoretical or experimental work which is beyond the scope of the present paper.

4.1.4 Doping density in the shunt

Similarly, we introduce a separate parameter $b > 0$ that allows us to model the effect of having different doping density and/or mobility in the shunt vs. superlattice quantum wells. Also, recognize that the field in the shunt is almost uniform and $n_m^{(s)} \approx N_D^{(s)}$ when the conductance in the shunt is high, where $N_D^{(s)}$ is the doping density in the shunt. This leads to the following modification of Eq. (4.14),

$$j_{\| m-1 \to m}^{(s)} = -e\mu \tilde{n}_m^{(s)} F_{\| m}^{(s)} - eD_0 \frac{\partial \tilde{n}_m^{(s)}}{\partial z} \approx -eb\mu^{(s)} \tilde{N}_D F_{\| m}^{(s)}, \tag{4.20}$$

where $b\mu\tilde{N}_D = \mu^{(s)}\tilde{N}_D^{(s)}$. Note that $b > 1$ when the doping density in the shunt is greater than that in the quantum wells and b is much less than one when the shunt is weakly conducting so that only a small fraction of the total vertical current flows through it.

4.1.5 The total current

It is also useful to point out that the total current,

$$J = \left(\epsilon_r \epsilon_0 \dot{F}^{(s)}_{\|m} + j^{(s)}_{\|m \to m+1}\right) \cdot \delta_x + \int_0^{L_x} \left(\epsilon_r \epsilon_0 \dot{F}_{\|m} + j_{\|m \to m+1}\right) dx, \tag{4.21}$$

is the same for each period. To show this, note that the Poisson equation can be written as

$$\nabla \cdot (\mathbf{F}_\perp + \mathbf{F}_\|) = \frac{e}{l \epsilon_r \epsilon_0} (n_m - N_D), \tag{4.22}$$

or

$$\frac{F_{\|m} - F_{\|m-1}}{l} + \frac{\partial F_\perp}{\partial x} = \frac{e}{l \epsilon_r \epsilon_0} (n_m - N_D). \tag{4.23}$$

Substituting the above equation into Eq. (4.3) yields

$$l \epsilon_r \epsilon_0 \frac{d}{dt} \left(\frac{F_{\|m} - F_{\|m-1}}{l} + \frac{\partial F_\perp}{\partial x} \right) = j_{\|m-1 \to m} \; - \; j_{\|m \to m+1} \; - \; \frac{\partial j_{\perp m}(x)}{\partial x}. \tag{4.24}$$

Then, one integrates both sides of the preceeding equation with respect to x from $-\delta_x$ to L_x. Due to the vanishing boundary conditions $F_\perp(-\delta_x) = F_\perp(L_x) = 0$ and $j_{\perp m}(-\delta_x) = j_{\perp m}(L_x) = 0$, the lateral terms in the above equation integrate to zero. This yields

$$\epsilon_r \epsilon_0 \frac{d}{dt} \int_{-\delta_x}^{L_x} F_{\|m} dx + \int_{-\delta_x}^{L_x} j_{\|m \to m+1} dx = \epsilon_r \epsilon_0 \frac{d}{dt} \int_{-\delta_x}^{L_x} F_{\|m-1} dx + \int_{-\delta_x}^{L_x} j_{\|m-1 \to m} dx. \tag{4.25}$$

which shows that the total current is independent of the well index m. Note that the current through the shunt will be the dominating contribution to the total current of a superlattice if the shunt is thick and well-conducting. Even a completely disconnected shunt (i.e. $a = 0$) contributes a constant current of $J_0^{(s)} = \delta_x e \mu N_D U/(Nl + d)$ to the total current J of a homogeneous superlattice. Since we are interested in effects arising from the interaction between the superlattice and the shunt, we will in the following discuss the current dynamics on the basis of the superlattice current defined by $J_{\text{superlattice}}(t) = J(t) - J_0^{(s)}$.

4.2 Parameters and Time scales

The parameters that we use in the simulation are listed in Table I. These parameters come from weakly-coupled GaAs/AlAs superlattice structures that have been studied in experiments.[62] Variations of the parameters such as barrier thickness and doping density have been extensively studied in previous work and dynamical features are found to be robust.[33] The nonlinear behaviors such as current branches are clearly seen at low temperature in experiments.[70] The quantum wells and the shunt are GaAs with same doping level and the barriers are undoped AlAs. We make the assumption that mobility μ and D_0 are fixed and choose typical values for GaAs.[66] We expect qualitative agreement over a large parameter regime. We found that there are very different time scales in this complex structure which requires an implicit method of numerical iteration. The first time scale τ_b is the dielectric relaxation time in the bulk material both in the shunt and in each quantum well in the superlattice. It is determined by the doping density. We know that the conductivity g is proportional to the charge density

N -	N_D (m^{-2})	w (nm)	d (nm)	μ (m^2/Vs)	D_0 (m^2/s)	T (K)	ϵ_r -
40	1.5×10^{15}	9	4	10	0.015	5	13.18

Table 4.1: Parameters used for the shunted weakly-coupled superlattice.

$$g \approx e\mu N_D/l \sim 1.6 \times 10^{-19} \times 10 \times 10^{23} (\Omega\mathrm{m})^{-1} \sim 10^5 (\Omega\mathrm{m})^{-1} \tag{4.26}$$

So the dielectric relaxation time in the shunt layer and within each quantum well is approximated as

$$\tau_b = \frac{\epsilon_r \epsilon_0}{g} \sim \frac{0.1 \times 10^{-9}}{10^5}(\mathrm{s}) \sim 10^{-15}(\mathrm{s}) \qquad (4.27)$$

which is relatively fast due to the high conductivity. This is the time it takes for a fluctuation in the charge density to be neutralized within either the shunt layer or quantum wells.

The second time scale τ_t is the one in the vertical dynamics. According to the sequential resonant tunneling model, the vertical current is to the order of 10^{-4} (A/m^2) and the positive differential conductivity g_t is of order 0.1 $(\Omega\ \mathrm{m})^{-1}$. Thus, $\tau_t = \epsilon_r \epsilon_0 / g_t \sim 10^{-9}$ s, a much larger time scale than τ_b. Moreover, from numerous previous works, we also know that the behavior of the electrons in the vertical direction is not simply dielectric relaxation. More complex phenomena, such as current self-oscillation, or injected dipole relocation due to switching, have much longer time scales ranging up to microseconds. The time scale τ_t sets a lower limit of the time scales for these nonlinear processes.

Another important time scale τ_i is the time that it takes to carry away or supply the electrons in the superlattice through the shunt. Because the vertical processes are relatively slow, if the shunt has good connection and high conductance, the electrons will move laterally, pass through the intersection between the quantum well and the shunt, and drift away through the shunt. This time scale τ_i is considerably larger than τ_b since the electrons have to move into the shunt first. Later we will see that it takes 1 ns to deplete a full CAL in a small superlattice. The presence of extremely different time scales means that the numerical integration is a stiff problem and this suggests the use of an implicit method. The numerical procedure is described in the Appendix.

4.3 Numerical method

In order to implement the implicit method, the dynamical variables, i.e., the electron densities $n_m(x)$, should be computed from the system Eqs. (4.3) and (4.13). However, the $n_m(x)$ are deeply buried in these equations, where the currents depend on the field that relates to $n_m(x)$ by solving Poisson equation Eq. (4.7). So instead of solving for $n_m(x)$ directly, we use the semi-implicit Euler method and numerically calculate the Jacobian matrix that is needed for this method. The procedure is as follows: after discretization of the space, the quantities of potential and charge density are placed on the grid. The fields and currents (also the charge density that is needed to calculate the currents) are placed on a staggered grid. Knowing the charge density distribution, the potential is determined by the Poisson equation using a method described in Ref. [66]. After that, the currents to each grid point are calculated from the electric fields which are immediately obtained from the potential (cf. Eqs. (4.10) and (4.16)). Then the charge densities are iterated one step forward in time as

$$e\mathbf{n}' = e\mathbf{n} + dt\mathbf{J}(\mathbf{n}'), \tag{4.28}$$

where $\mathbf{n} = (n_{11}, n_{12}, ..., n_{21}, n_{22}, ...)^T$ is the vector whose components are the charge densities on each grid point. The first subscript denotes the superlattice period number and the second one is the grid point index in the x direction. The vector current $\mathbf{J}$ is the total current flow into or out of each grid point. $\mathbf{n}'$ is the new charge density configuration after time step dt. Since we are using the implicit method, $\mathbf{J}$ must depend on the future charge density configuration instead of the old one. We linearize the equations:

$$\mathbf{n}' = \mathbf{n} + \frac{dt}{e}\left[\mathbf{J}(\mathbf{n}) + \left.\frac{\partial \mathbf{J}}{\partial \mathbf{n}}\right|_{\mathbf{n}} \cdot (\mathbf{n}' - \mathbf{n})\right], \tag{4.29}$$

where $\partial J/\partial n$ is the Jacobian matrix, whose dimension is N by N, where N is the number grid points. Rearranging this equation yields:

$$\mathbf{n}' = \mathbf{n} + \frac{dt}{e}\left[\mathbf{1} - dt\frac{\partial \mathbf{J}}{\partial \mathbf{n}}\right]^{-1} \cdot \mathbf{J}(\mathbf{n}) \tag{4.30}$$

We mentioned that the currents do not depend on the charge densities explicitly. So to calculate the Jacobian matrix, we first calculate $\mathbf{J}(\mathbf{n})$, then slightly change the charge density at one grid point to $n_{ij} + \delta n_{ij}$ and calculate the currents $\mathbf{J}'$ based on this charge configuration. Then one row of the Jacobian matrix is immediately obtained by $(\mathbf{J}' - \mathbf{J}(\mathbf{n}))/\delta n_{ij}$.

To solve Eq. (4.30), we do not invert the matrix. Instead, we write it as:

$$\frac{dt\mathbf{J}(\mathbf{n})}{e} = \left[\mathbf{1} - dt\frac{\partial \mathbf{J}}{\partial \mathbf{n}}\right] \cdot (\mathbf{n}' - \mathbf{n}). \tag{4.31}$$

Then we solve this set of linear equations by Gauss elimination.

4.4 Dependence of shunting dynamics on the lateral size of the Superlattice

In this section, we discuss the effects of the lateral size L_x of the superlattice with a high quality shunting layer, i.e., $a = b = 1$. The shunting layer has a width δ_x such that varying δ_x does not affect the dynamics in the shunt. This is numerically confirmed even for the chaotic case that we will discuss below, where a 80 nm shunting layer has the same effect as a 8 mm one. This is because τ_b is much smaller than τ_i and the electrons entering the shunt are carried away so fast that a change in the shunt conductance does not change τ_i. We will study the superlattices with a relatively high contact conductivity $\sigma = 0.04$ $(\Omega\mathrm{m})^{-1}$. At this value of σ, without a shunt, the superlattice has a static high field domain near the emitter and a static low field domain near the collector separated by a static charge accumulation layer (CAL).

Due to the high quality shunt the total current is dominated by the contribution of the current through the shunt. As discussed at the end of Section 4.1, we will therefore consider the superlattice current $J_{\text{superlattice}}$. Also, since we are varying L_x, we scale current to current density.

4.4.1 High quality shunting layer with small L_x

Figure 4.2 shows charge and current density plots for a relatively narrow superlattice with lateral extent $L_x = 20\ \mu\text{m}$. The initial state is prepared as a charge configuration for the superlattice without shunt at total applied voltage $U = 2.1$ V and shows a static charge accumulation layer at the 20th period. After an interval of about 1 ns, the space charge configuration is almost uniform. The in-plane current is plotted as a vector field and shows the electrons in the CAL move in the lateral direction (the opposite direction of the current) into the shunt. We can see that when the system reaches steady state, the net charge is almost neutral, i.e., $n = N_D$, everywhere in the superlattice and the shunt. There are still some small lateral current flows at the first and the last period.

If we take a close look at the steady state, we find that there is a small CAL at the first period and a CDL nearby (Fig. 4.3(a)). The situation is almost inverted near the collector. To better understand this, we focus on the operation points near the emitter shown in Fig. 4.3(b) at $x = 20\ \mu\text{m}$. In this case, the field is almost uniform in the superlattice and each period is biased in the NDC region. The field across the first barrier between the emitter and the first well will also have this same value in the absence of charge accumulation in the first well. This causes a vertical current from the emitter to the first period (thin solid line in Fig. 4.3(b)) which is much larger than the vertical current in the corresponding NDC region of the superlattice. Close to the shunt this extra current will give rise to a lateral current which will quickly reach the shunt and is carried away by the shunt. A little further away from

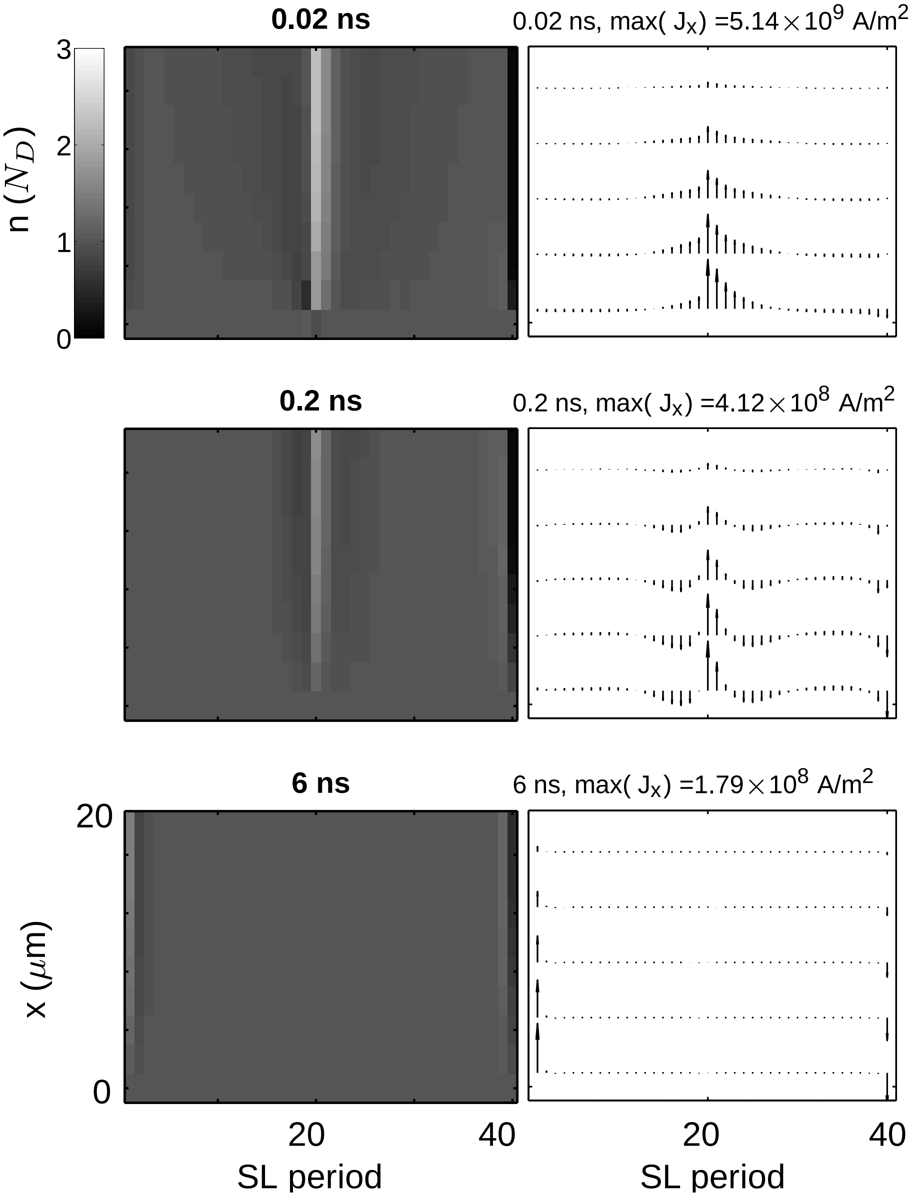

FIGURE 4.2: Charge density plots (left column) and current vector plots of $j_{\perp m}(x)$ (right column) for a superlattice with $L_x = 20$ μm, $U = 2.1$ V and $\sigma = 0.04$ $(\Omega\text{m})^{-1}$ at 0.02, 0.2 and 6 ns. Initial condition is a CAL at the center of the superlattice. The shunt is at the bottom. The color bar on the left of the first contour plot is the scale encoding in units of N_D used throughout this chapter.

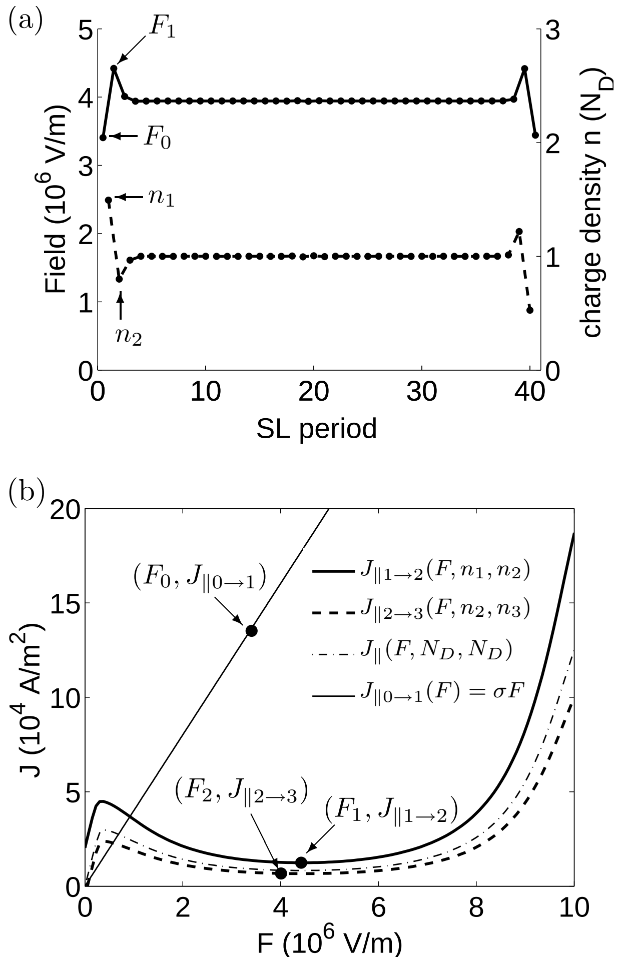

FIGURE 4.3: The steady state for a superlattice with $L_x = 20$ μm, $U = 2.1$ V and $\sigma = 0.04$ $(\Omega\text{m})^{-1}$ at $x = L_x$: (a) field profile (solid line) and charge density (dashed line), (b) The solid dots indicate the actual current operation points on the local vertical current field characteristics $j_{\|m\to m+1}(F, n_m, n_{m+1})$.

the shunt where the lateral current is not sufficient to completely neutralize this extra current, a small CAL is formed in the first well which lowers the electric field and therefore the current across the first barrier. At the same time, the electric field in the second barrier is pushed above the uniform field, causing a very small CDL next to the CAL. Similar arguments can be applied to the collector to explain the appearance of a small CDL in the last quantum well. The overall effect is that a nearly uniform vertical electric field configuration is stabilized for these conditions.

4.4.2 High quality shunting layer with large L_x

As the lateral size L_x of the superlattice becomes larger, the CAL and CDL near the emitter become more prominent (cf. Fig. 4.4(a)-(c), $L_x = 160$ μm) since with increasing distance to the shunt the lateral current becomes less efficient at carrying away the excess current from the emitter to the shunt.

For wider superlattice (cf. Fig. 4.4(d)-(f), $L_x = 640$ μm), the field closer to the shunt is more uniform and the CAL is still attached to the emitter. However, away from the shunt, the CAL detaches from the emitter and locates itself in the first few periods and the nonuniform field region becomes larger. This behavior is due to the lateral current being insufficient to carry away the extra current from the emitter. Thus, the CAL grows bigger and tends to move toward the collector. With the center of the CAL located in different wells at different x positions, the lateral gradients can be increased and a sufficient lateral current can be sustained. The field profile at $x = 640$ μm is plotted in Fig. 4.4(f). Field domains are forming as the field is low to the left of the CAL and high to the right of the depletion region. In this case, the upstream CAL (closer to the emitter, at the left bottom corner of Fig. 4.4(d)) and the downstream CAL (closer to the collector, the wider one in Fig. 4.4(d)) are still connected and this is a time-independent steady state.

In the above case, the lateral size of the superlattice is just below a characteristic value for which the steady state loses stability to oscillatory behavior. Figure 4.5 ($L_x = 800$ μm) shows the simulations of a slightly wider superlattice than considered above. The large downstream CAL still stays in that position. However, due to the large size of the superlattice, the lateral current is not able to sustain a connected stable CAL. The small upstream CAL touches and breaks off from the downstream CAL periodically. There is a small amplitude oscillation in the total current which is shown in the top panel.

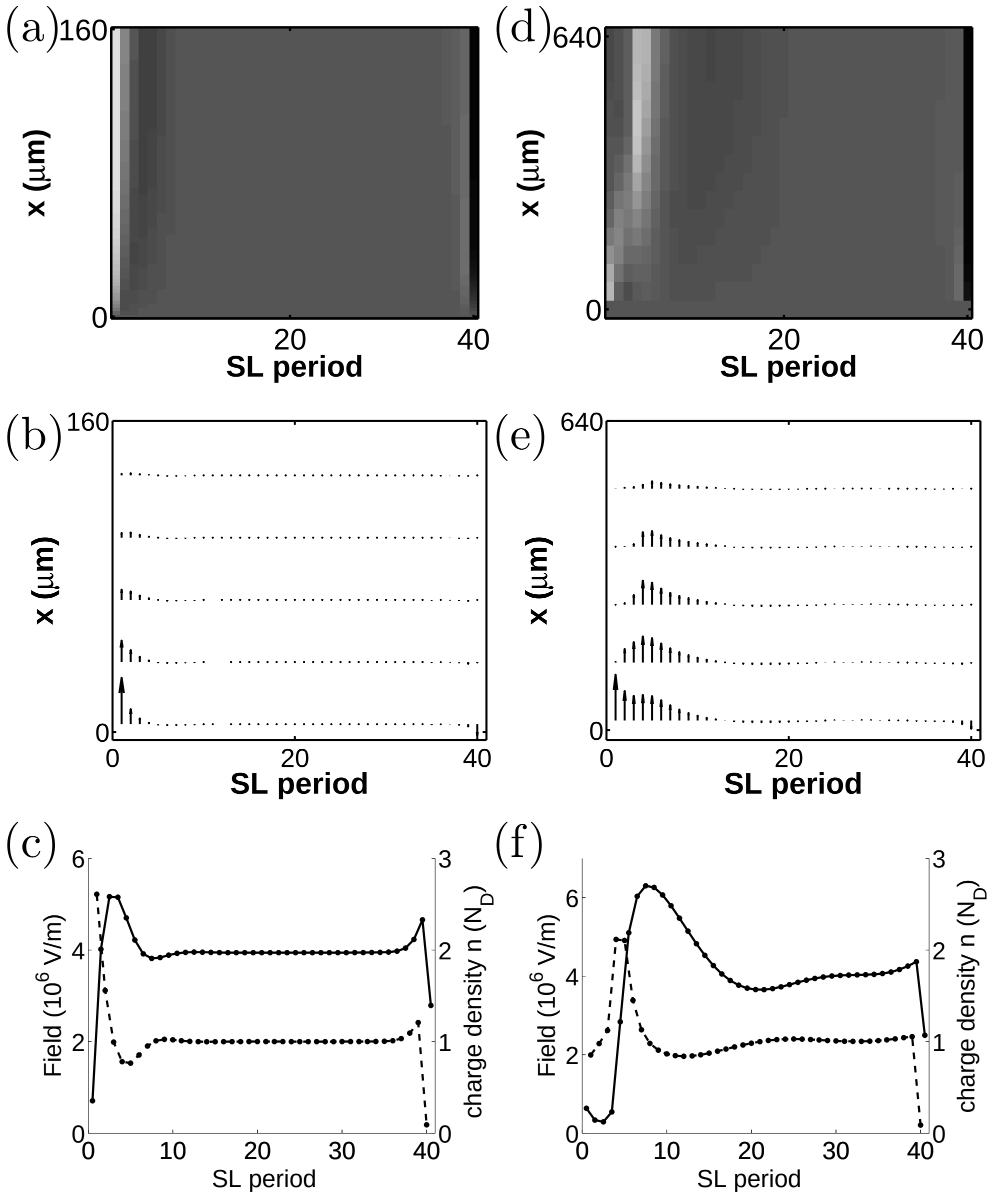

FIGURE 4.4: Steady states: (a), (d) Charge density plots, (b), (e) current vector plots and (c), (f) field profile (solid line) and charge density (dashed line) at $x = L_x$ for $L_x = 160$ μm (left column) and $L_x = 640$ μm (right column), respectively, with $U = 2.1$ V and $\sigma = 0.04$ $(\Omega\text{m})^{-1}$.

For an even wider superlattice (Fig. 4.6 with $L_x = 1.28$ mm), the upstream and downstream CALs are mostly disconnected. The upstream CAL extends laterally into the superlattice and moves toward the downstream CAL(at time 1.969 ms). For

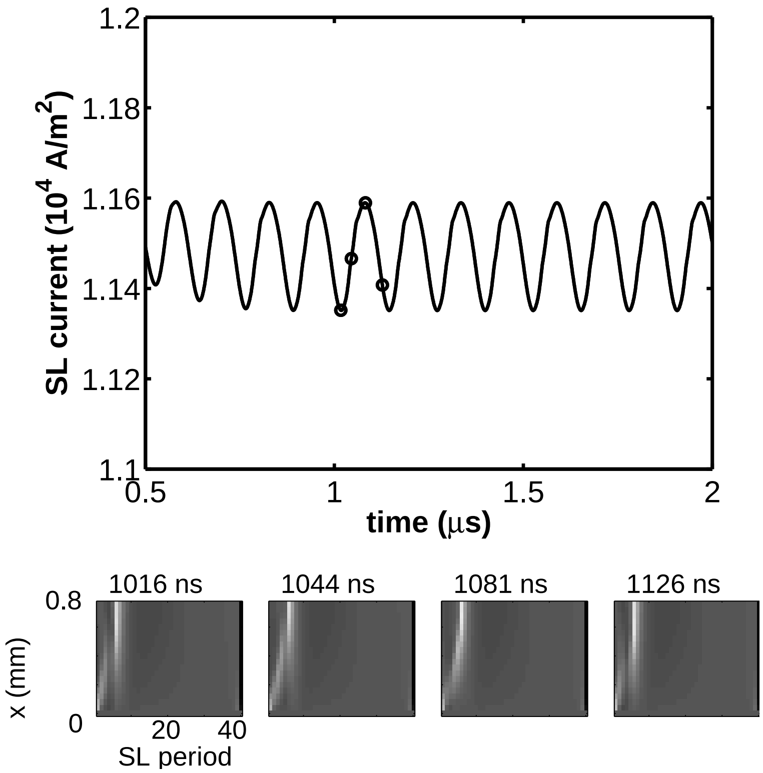

FIGURE 4.5: superlattice current density $J_{\text{superlattice}}/L_x$ and snapshots of charge density distribution for $L_x = 0.8$ mm, $U = 2.1$ V and $\sigma = 0.04$ $(\Omega\text{m})^{-1}$. The times of the snapshots are marked as solid circles in the upper panel. The contour plots have the same superlattice period labeling as the first panel.

certain times during the dynamical evolution (not shown in Fig. 4.6), the upstream CAL breaks off from the emitter and reaches and merges with the downstream CAL. Mostly, there is a depletion region forming between the upstream and downstream CALs (2.211 ms). For certain times, it grows into a full CDL extending across the entire lateral dimension of the structure and, in this case, the upstream CAL also grows into a full CAL (2.395 ms). Then all three fronts begin to move downstream. The downstream CAL and the CDL quickly dissipate and the upstream CAL splits into two segments separated by a small CDL, and we return to the situation shown in the leftmost contour plot of Fig. 4.6. Although these behaviors are quite complicated, they are still periodic, and during each period, the upstream and downstream CALs

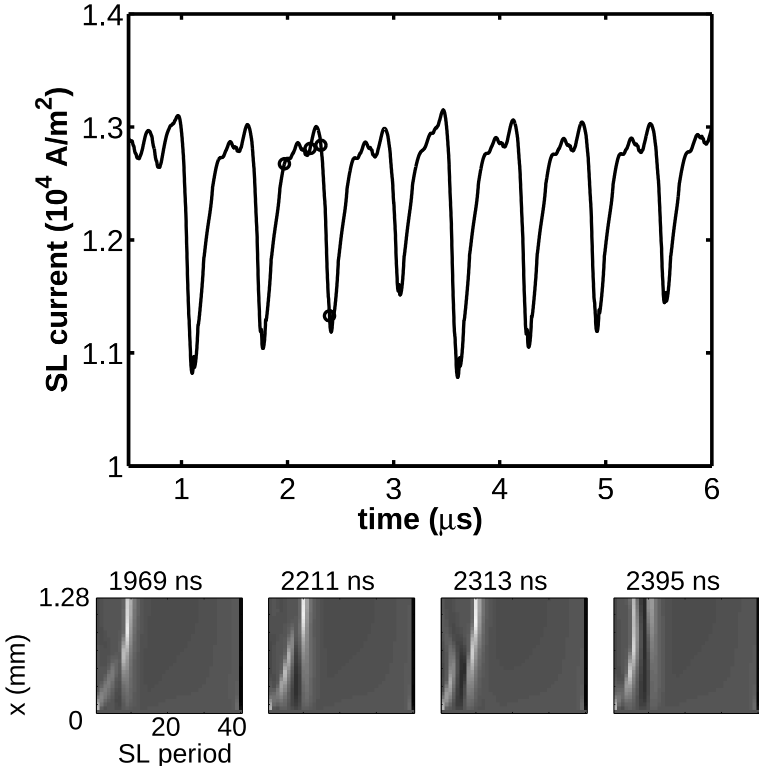

FIGURE 4.6: superlattice current density $J_{\text{superlattice}}/L_x$ and snapshots of charge density distribution for $L_x = 1.28$ mm, $U = 2.1$ V and $\sigma = 0.04$ $(\Omega\text{m})^{-1}$. The times of the snapshots are marked as solid circles in the upper panel. All the contour plots have the same superlattice period labeling as the first panel of Fig.4.5.

merge several times.

However, for an extremely wide superlattice (Fig. 4.7, $L_x = 2.56$ mm), the behavior is apparently chaotic. The effect of the shunt is to cause a CAL attached to the emitter near the shunt. For large values of x, the shunt has less effect and this CAL detaches from the emitter, tends to move downstream to the collector and thus extends toward the downstream CAL. Due to the large lateral size of the superlattice, the impact of the shunt layer becomes very weak on the opposite side of the superlattice. Thus, the downstream CAL is located very close to the 20th period where it would be in the absence of a shunting layer. The merging of the CALs described in last paragraph also appears here except that the merging events are

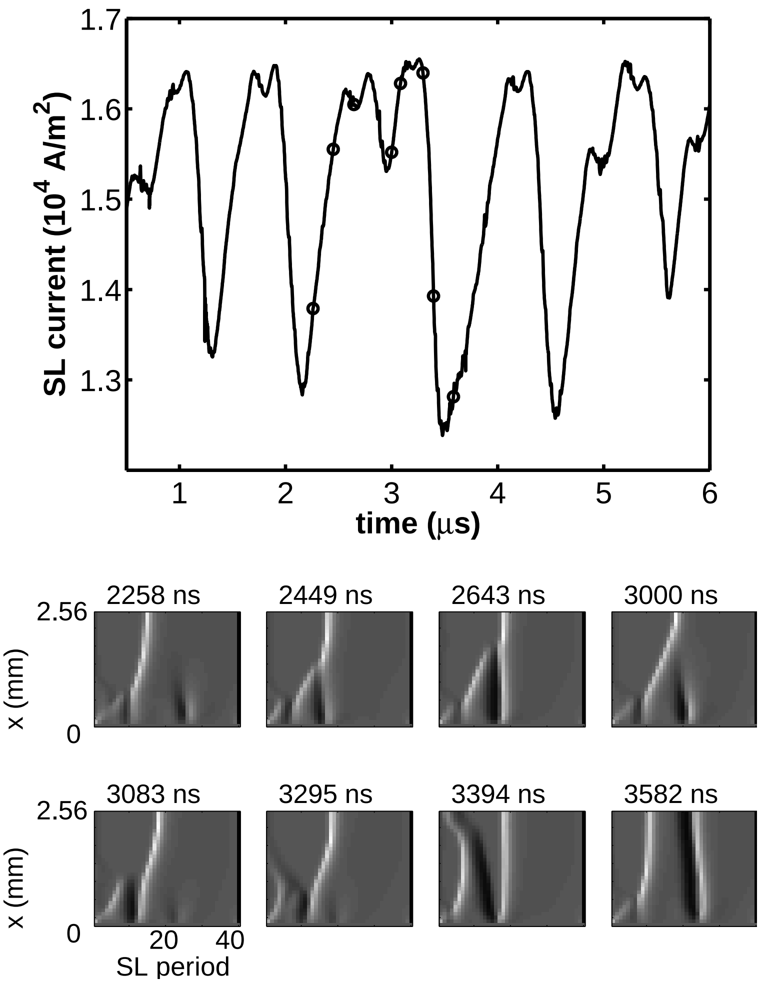

FIGURE 4.7: superlattice current density $J_{\text{superlattice}}/L_x$ and snapshots of charge density distribution for $L_x = 2.56$ mm, $U = 2.1$ V and $\sigma = 0.04$ $(\Omega\text{m})^{-1}$. The times of the snapshots are marked as solid circles in the upper panel. All the contour plots have the same superlattice period labeling as the first panel of Fig.4.5.

now difficult to predict and manifestly not periodic.

Figure 4.8 shows the behavior of a superlattice with $L_x = 5.12$ mm. It should be noted that real superlattice samples rarely have such a large size. In this case, the unstable dynamics only occurs in the portion of the superlattice closest to the shunt. In the portion of the superlattice away from the shunt, a CAL is located at the 20th well, where the shunt has no apparent influence. Over time, the lateral extension of this CAL changes. When a large CDL collides with it at 5.696 ms, the static CAL

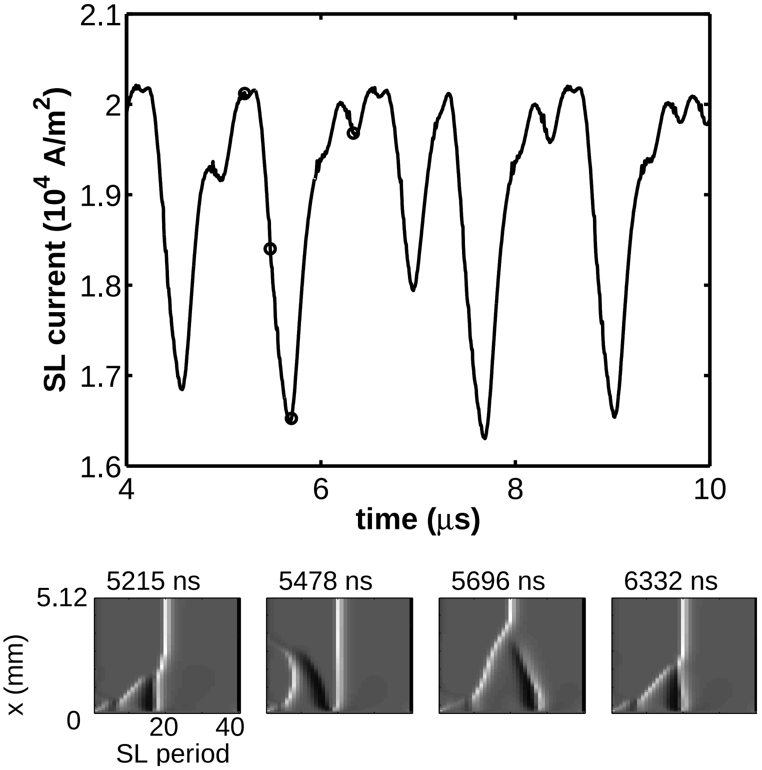

FIGURE 4.8: superlattice current density $J_{\text{superlattice}}/L_x$ and snapshots of charge density distribution for $L_x = 5.12$ mm, $U = 2.1$ V and $\sigma = 0.04$ $(\Omega\text{m})^{-1}$. The times of the snapshots are marked as solid circles in the upper panel. All the contour plots have the same superlattice period labeling as the first panel of Fig.4.5.

shrinks to a small size, causing a large dip in the current trace. The presence of such charge tripole configurations [71] of one CDL and two CALs has already been shown to be associated with chaotic behavior in one-dimensional superlattice models without lateral dynamics.[72]

To summarize, we are able to identify three characteristic length scales in the x direction. The shortest one is the decay length $\bar{L}_x$ (of order 10 μm) at which the charge density in the first quantum well increases from N_D at the superlattice-shunt interface to its maximum value (cf. Fig. 4.4(a)-(c)). The next length scale (of order 200 μm) is the range above which the vertical field configuration loses uniformity and static field domains start to form (cf. Fig. 4.4(d)-(f)). The longest length scale (of order 700 μm) is the width of the superlattice above which the steady state loses stability to oscillatory behavior. This implies that lateral uniformity in the electric field distribution can be expected when L_x is smaller than the intermediate characteristic length scale. The shortest decay length $\bar{L}_x$ can be estimated by noting that the extra current coming from the emitter must be directed to the shunt by the negative gradient of the lateral current $J_\perp$, i.e., $\frac{\partial J_\perp(x)}{\partial x} = J_{\|0\to1}(x) - J_{\|1\to2}(x) < 0$. Then there is approximately a decay length $\bar{L}_x$, at which the quantities such as $J_\perp(x)$, $n(x)$ and $F_x(x)$ approach asymptotic values exponentially. Calculation shows that $\bar{L}_x$ is of order 10 μm for the parameters used in Table I, in agreement with our numerical results.

4.5 Dependence of dynamical behavior on the shunt properties

In the previous section, we have seen that the width of the superlattice determines the lateral dynamics of electronic transport and that the shunt can stabilize a nearly *uniform* field configuration in sufficiently narrow superlattices. Now we investigate the effects of the shunt properties on a small superlattice with width of 20 μm where the lateral field and electron density profiles are almost uniform. Since the charge density is almost uniform laterally, we modify the model such that *the superlattice is collapsed to one point in x direction.* This modification significantly reduces the complexity of the simulation. We first study the effects of connectivity parameter a on a superlattice with conductivity $\sigma = 0.04(\Omega\text{m})^{-1}$ chosen as in the previous section. Then we study the effects of a on a superlattice with lower contact conductivity $\sigma = 0.016(\Omega\text{m})^{-1}$, which corresponds to moving fronts and current self-oscillations in unshunted superlattices,[44] and briefly discuss the effects of shunt conductivity parameter b and width δ_x. The calculation results from this reduced superlattice model have been confirmed by the full superlattice model for a range of different values of a. Since L_x is fixed, we plot the unscaled superlattice current $J_{\text{superlattice}}$.

4.5.1 Dynamical behavior vs. connectivity parameter a for large contact conductivity

Figure 4.9(a) shows a bifurcation diagram using as the bifurcation parameters the connectivity parameter a and the voltage U for $\sigma = 0.04(\Omega\text{m})^{-1}$. There is a bounded region where the system exhibits periodic or chaotic oscillations, shown as the region enclosed by dashed lines in Fig. 4.9(a). The value of the connectivity parameter a of the oscillatory region ranges from about 6×10^{-3} to 7×10^{-6}. In real samples, such a weak connection between the superlattice and the shunt could be associated with a potential barrier formed between the superlattice and the shunt due to band bending or an oxide layer.

For $a \gtrsim 6 \times 10^{-3}$, the charge density in the superlattice is almost uniform except for a small CDL near the emitter, the same situation shown in Fig. 4.2. With the increase of voltage, this CDL becomes more prominent and there is an CAL in the first period. However, this CAL never detaches from the emitter for any value of voltage when $a \gtrsim 6\times10^{-3}$. This is reasonable because for $a \gtrsim 6\times10^{-3}$, the connection is strong enough that the shunt is able to maintain the field in the superlattice almost uniform.

Another stable region is $a \lesssim 7 \times 10^{-6}$. In this region, a static CAL is formed in the superlattice and located close to the position where it is expected when there is no shunt. This is also easy to understand because the connection is so weak that the shunt has almost no influence on the superlattice.

Between these two values of a, we have a transition region where oscillations occur for certain ranges of applied voltage. Here, the bifurcation scenarios by varying voltage are investigated for two sets of values (A and B) of the control parameters.

The bifurcation for point A occurs at $a = 1.00 \times 10^{-3}$ and $U = 1.485$ V (Fig. 4.9(b), 4.10-4.12). Inside the oscillatory region (approximately $U \leq 1.485$ V), the charge density distribution in the superlattice oscillates and the oscillation only

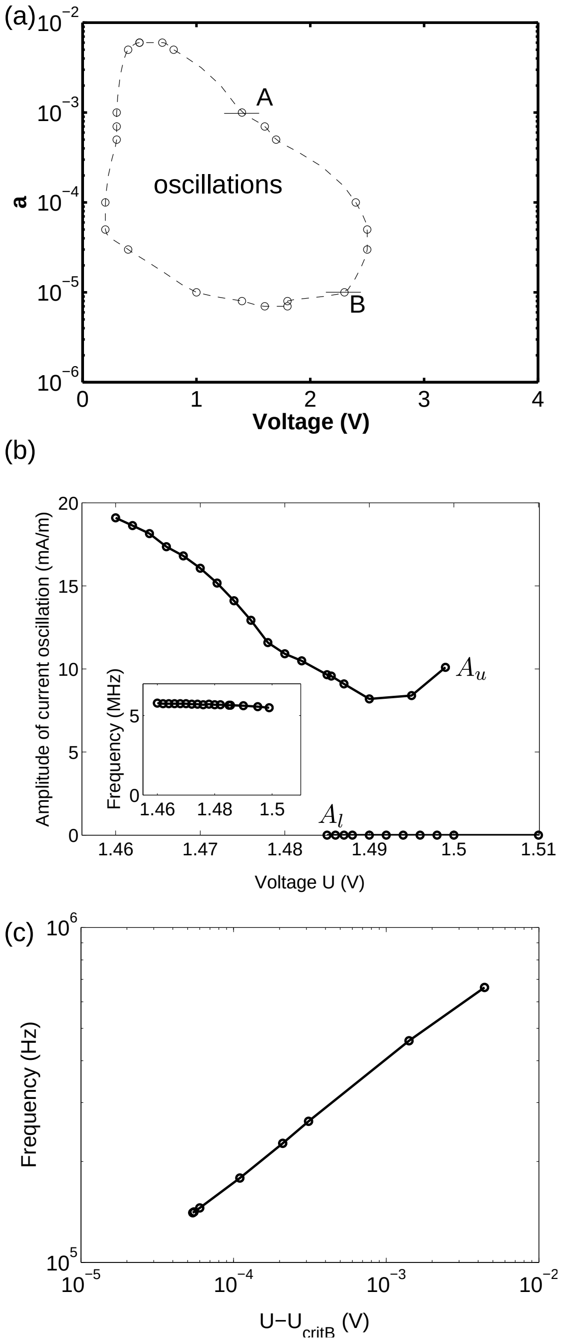

FIGURE 4.9: (a) Bifurcation diagram for $\sigma = 0.04$ $(\Omega\text{m})^{-1}$, $L_x = 20$ μm, $b = 1.00$. Dashed curve shows the approximate boundary of the oscillatory region and location of studied bifurcation points A and B. (b) Bifurcation scenario at A for $a = 1.00 \times 10^{-3}$: amplitude vs. voltage (main figure) and frequency vs. voltage (inset). Points A_u and A_l denote the endpoints of the upper and the lower branches, respectively. (c) Bifurcation scenario at B for $a = 1.00 \times 10^{-5}$: scaling of frequency vs. voltage (double logarithmic plot); $U_{critB} = 2.30441$ V.

involves part of the superlattice (cf. Fig. 4.10). There is a static CAL near the emitter but this is clearly detached from the emitter. The oscillation occurs in the wide region to the right of the CAL in the form of moving charge dipoles (CALs and CDLs), cf. Fig. 4.10(a). However, at any given time, there are three to four pairs of dipoles present. From Fig. 4.10(b), we can see that the charge densities have large amplitude fluctuations along the z direction and the higher frequency component of the current oscillation is due to the movement of these dipoles (Fig. 4.10(c)). This higher frequency f_1 is nine times the lower one f_2 at which the collector receives the moving dipoles. Here we observe the *coexistence* of static CAL and steady moving fronts.

The bifurcation scenario of A is illustrated by Fig. 4.9(b), where the amplitude of the current oscillation is plotted versus the applied voltage. There is a bistability region between $U \approx 1.485$ V and 1.50 V, where the system either oscillates (upper branch) or is in a steady state (lower branch).

The bifurcation at point A_l at the end of the lower branch is studied in Fig. 4.11. When the system starts from a uniform configuration at $U = 1.486$ V, shown in Fig. 4.11(a), (b), (c), it first oscillates similar to the full oscillation in Fig. 4.10, except that the CALs and CDLs are much smaller in Fig. 4.11(b). The oscillation gradually decays to a steady state where there is only a single stable CAL and no charge fronts to its right, as shown in Fig. 4.11(c). The amplitude of the current oscillation is quite small and decays to zero. The well-to-well hopping of the small charge fronts does not have an appreciable effect on the current oscillation form as found for the mature fronts in Fig. 4.10(c). Instead, the shape of the current oscillation is smooth and sinusoidal and possesses a well-defined frequency. After a transient interval, the amplitude $A(t)$ of the current oscillation decays exponentially, i.e., $A(t) = A(t_0) \exp \lambda t$ and the rate λ can be determined by fitting. It also should be mentioned that the initial state corresponding to the uniform field configuration

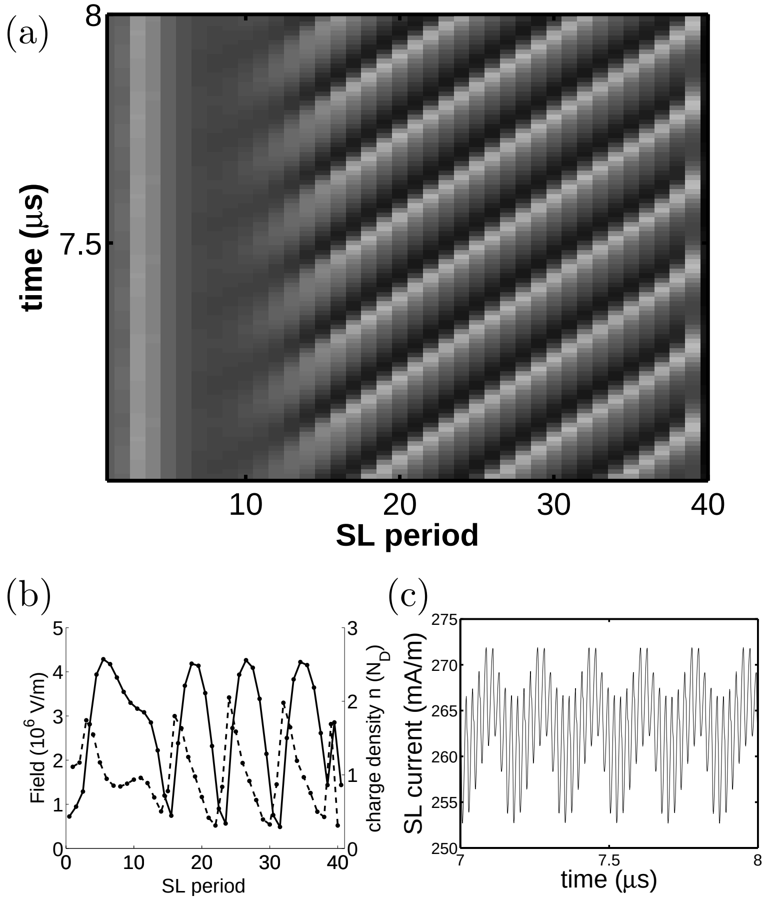

FIGURE 4.10: (a) Charge density distribution evolving in time (gray scale is the same as in Fig. 2), (b) a snapshot of field profile (solid line) and charge density profile (dashed line) at $t = 8$ ns and (c) superlattice current $J_{\text{superlattice}}$ on the upper branch of Fig. 4.9b. Parameters: $a = 1.00 \times 10^{-3}$, $U = 1.46$ V, $\sigma = 0.04$ $(\Omega\text{m})^{-1}$.

falls into the basin of attraction of the upper oscillatory branch for $U \lesssim 1.486$ V. Hence, to obtain λ for the lower branch, we start the system from the steady state of $U = 1.486$ V. This initial state is used for all the points of the lower branch. In the case of $U = 1.481$ V, shown in Fig. 4.11(d), the amplitude of the current oscillation increases exponentially at first and after passing a certain threshold value, quickly evolves into the large oscillations of the upper branch. The inset shows the transition region and indicates that the small charge fronts grow into mature ones. The rate λ can also be fitted and now it is positive. The resulting λ versus U is plotted in

Fig. 4.11(e), showing a linear scaling. This clearly indicates that the bifurcation at A_l is a subcritical Hopf bifurcation. Supercritical Hopf bifurcations in different superlattice models have been found by Patra *et al.*[56] and by Hizanidis et al [73] at low contact conductivity with no shunt. Here we can also see that the time scales have the following relationship: $\tau_b \ll 1/f_{1,2} \ll 1/\lambda$.

It is likely that the bifurcation scenario at A_u in Fig. 4.9(b) is a saddle-node bifurcation which is probably caused by the collision of the stable limit cycle and the unstable limit cycle that arises from the subcritical Hopf bifurcation at A_l. In Fig. 4.12(c), the power spectrum of the limit cycle ($U = 1.4997$ V) and the power spectrum of the transient oscillation at $U = 1.49985$ V - which exceeds the saddle-node bifurcation value U_{A_u} - are almost identical. This rules out a subcritical torus bifurcation. Then we start the system from a configuration corresponding to the steady oscillation at $U = 1.46$ V, but for voltages just above U_{A_u} where there are no limit cycle states, so it eventually reaches the lower branch. Figure 4.12(a) shows this process at $U = 1.49985$ V. After a short time interval of about 1 μs, the oscillation amplitude $A(t)$ enters a regime of transient oscillations and after a relatively long time T, it suddenly exits this region and reaches a steady state. This process looks like a reverse process of Fig. 4.11(d). Figure 4.12(b) shows the decay of the CALs and CDLs. If we choose the critical value to be 1.499791 V, then the slope in Fig. 4.12(d) is -0.5. This means that $T \propto \frac{1}{\sqrt{U-U_{A_u}}}$, consistent with a system that undergoes a saddle-node bifurcation of limit cycles.[74]

The bifurcation at point B is at $a = 1.00 \times 10^{-5}$ (Fig. 4.13). For $U \lesssim 2.305$ V, the system oscillates. At first, there is a single CAL in the superlattice and a dipole is injected from the emitter. The CAL and dipole all move into the superlattice. The leading CDL moves about twice as fast as the two CALs[75] and when it catches up with the original CAL, they annihilate. The CAL of the dipole continues to

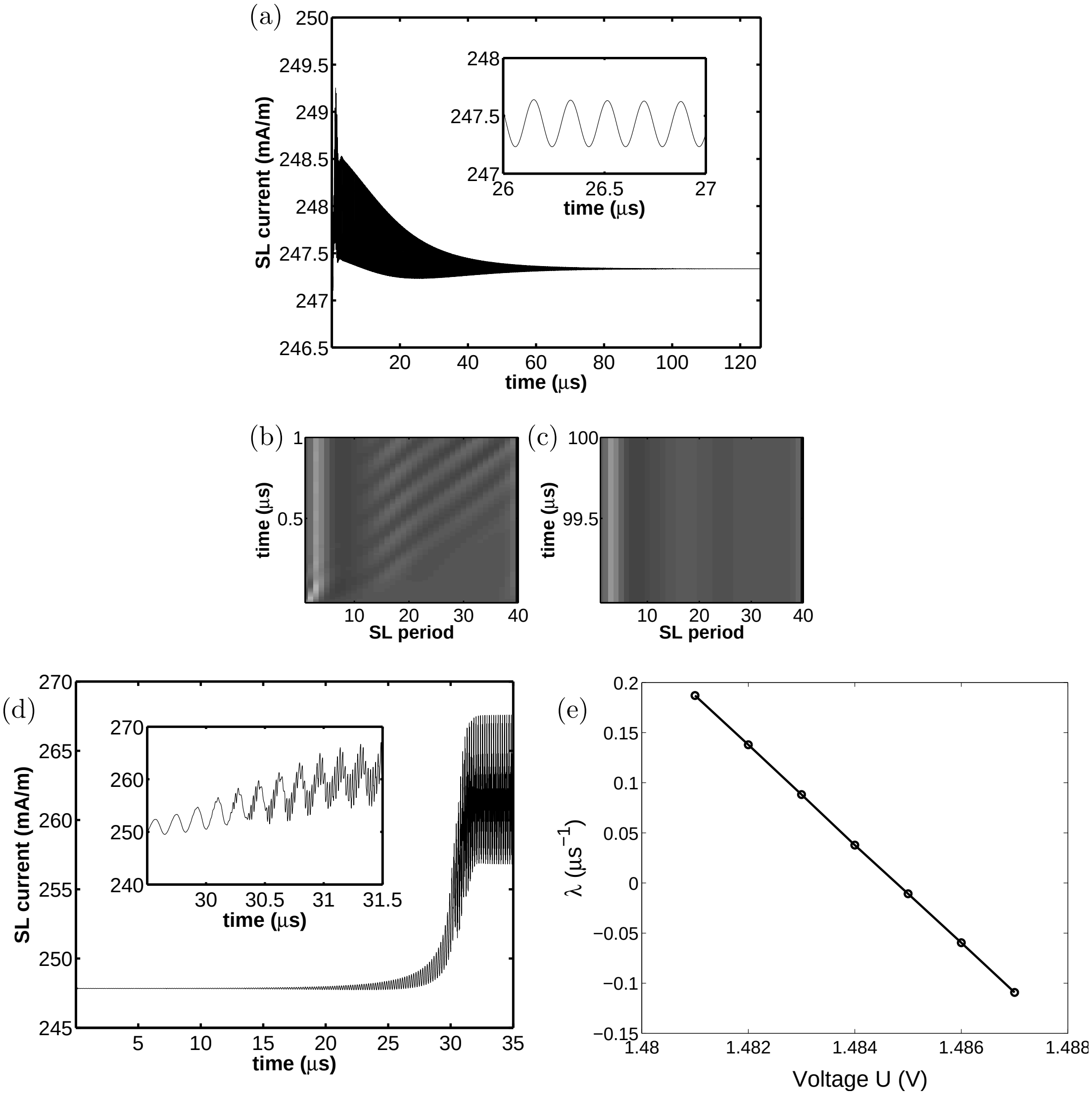

FIGURE 4.11: (a) superlattice current $J_{\text{superlattice}}$ vs. time for $U = 1.486$ V (the inset shows an enlargement), (b), (c) charge density distributions evolving for two different time intervals for voltage near bifurcation point A_l. (d) superlattice current for $U = 1.481$ V. (e) The rate λ of exponential decay $\lambda < 0$ (or increase $\lambda > 0$) of oscillation amplitude versus applied voltage U. Parameters: $a = 1.00 \times 10^{-3}$, $\sigma = 0.04$ $(\Omega\text{m})^{-1}$.

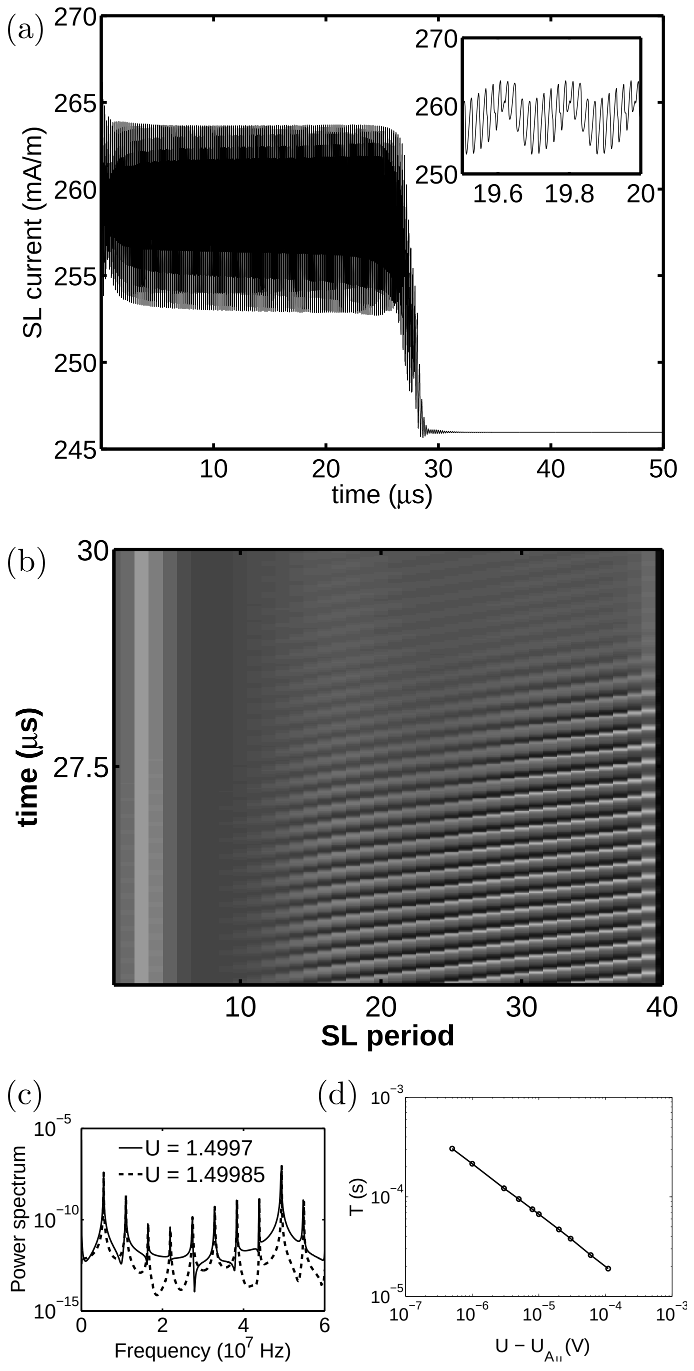

FIGURE 4.12: (a) superlattice current $J_{\text{superlattice}}$ (the inset shows an enlargement), and (b) charge density distribution evolving in time for $U = 1.49985$ V with $a = 1.00 \times 10^{-3}$, $\sigma = 0.04\ (\Omega\text{m})^{-1}$. (c) Power spectrum data for oscillations at $U = 1.4997$ V and $U = 1.49985$ V. (d) The time T for which the system exhibits transient oscillations versus the applied voltage $U - U_{A_u}$. $U_{A_u} = 1.499791$ V.

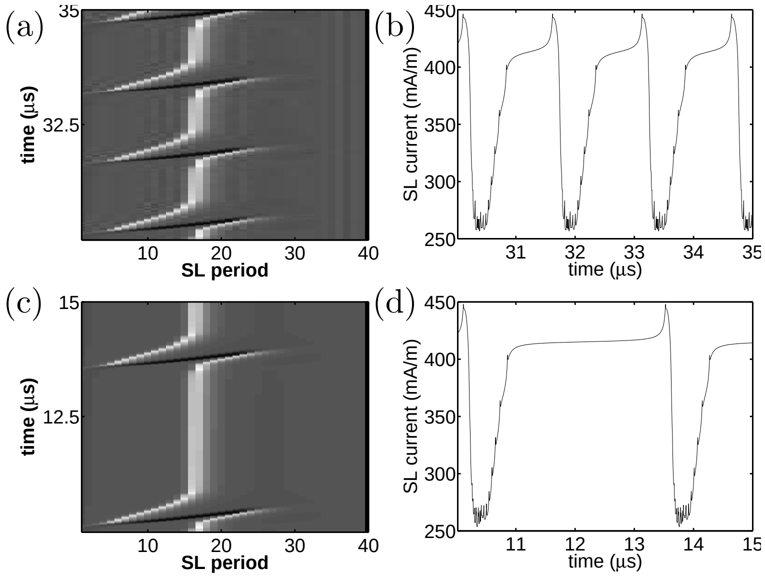

FIGURE 4.13: Bifurcation scenario at point B of Fig.9: (a), (c) charge density distributions vs. time, (b), (d) superlattice current $J_{\text{superlattice}}$ for $U = 2.3$ V (upper panel) and $U = 2.304$ V (lower panel), respectively, with $a = 1.00 \times 10^{-5}$, $\sigma = 0.04\ (\Omega\text{m})^{-1}$.

move forward until it reaches the position of the original CAL and stays there for a certain period of time, waiting for another round of dipole injection. Such a bifurcation of a stationary domain state has been reported before by Hizanidis *et al.* [57] for a one-dimensional superlattice model without shunt at higher contact conductivity. The time needed for a dipole to be injected is called the activation time and the time needed to return from the excited state to the fixed point is called the excursion time.[57] As the applied voltage U approaches the boundary, the activation time becomes longer and longer. Taking the critical value U_{critB} of voltage to be 2.30441 V and plotting the frequency of oscillation versus $U - U_{critB}$, we find the frequency obeys the square-root law which is the characteristic scaling law for the saddle-node infinite period bifurcation or SNIPER,[57] which is a global bifurcation of a limit cycle.

Inside the oscillatory region in the $a - U$ parameter space (Fig. 4.9(a)), we also

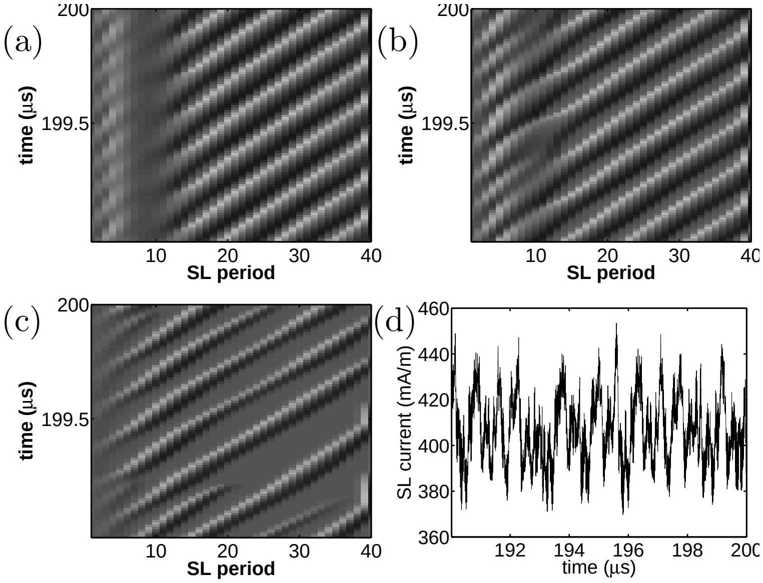

FIGURE 4.14: Charge density distribution vs. time for $a = 1.00 \times 10^{-3}$, $\sigma = 0.04\ (\Omega\text{m})^{-1}$ at (a) $U = 1.2$ V, (b) $U = 1$ V, and (c) $U = 0.5$ V. (d) superlattice current at $U = 0.5$ V.

find regimes of chaos. We still use $a = 1.00 \times 10^{-3}$. As the voltage U decreases inside the oscillatory region, the oscillation shown in Fig. 4.10 involves a larger part of the superlattice and the CAL near the emitter becomes less and less prominent until these moving dipoles cover almost all the superlattice shown Fig. 4.14(a),(b) at $U = 1.2$ V and 1.0 V. Further decrease of the voltage causes the disappearance of the static CAL and the dipoles either annihilate inside the superlattice or reach and disappear at the collector, shown in Fig. 4.14(c) for $U = 0.5$ V. Similar chaotic behavior has also been found in superlattices without a shunt.[75] These complicated and apparently chaotic oscillations are found at many points in the oscillatory regime of Fig. 4.9(a).

In the regime of the stable states between $a \approx 6 \times 10^{-3}$ and 7×10^{-6} (cf. the right hand region of Fig. 4.9(a)), the superlattice usually has a static CAL either inside the superlattice (for low a) or attached to the emitter (for high a) and there is a small static CDL to the right of this CAL. This means that the overall field profile is nearly uniform for larger a ($\gtrsim 6 \times 10^{-3}$), but static field domains form as a decreases.

4.5.2 Dynamical behavior for small contact conductivity

The bifurcation scenario for lower contact conductivity σ is simpler than for the high σ case. Figure 4.15 shows the bifurcation diagram for $\sigma = 0.016$ ($\Omega \mathrm{m}^{-1}$). This value of σ corresponds to current self-oscillation in the superlattice when there is no shunt.[44] The parameter space is again divided into an oscillatory regime and a stable stationary regime. The oscillatory regime starts at about the same value of a as the high σ case, i.e., $a \approx 6 \times 10^{-3}$. However, this oscillatory region does not have a lower bound. This is because without the shunt the superlattice still exhibits oscillations.

The different behaviors at $a = 1.00 \times 10^{-4}$ are shown in Fig. 4.15. As the voltage is deep inside the oscillatory region, dipoles are periodically injected into the superlattice and travel through the entire superlattice (Fig. 4.15(b)). As voltage increases, the distance that the dipoles travel becomes shorter and the CAL and CDL annihilate near the emitter (Fig. 4.15(c)). Similar behaviors have been found in a superlattice model without shunt.[75] As the voltage approaches the boundary, the CDL becomes less and less prominent and the length that the CALs travel becomes even shorter. After the voltage crosses the boundary, the CALs becomes static. The bifurcation scenario is similar to point A, described in the previous section, where there is bistability between oscillatory and steady states. The bifurcation scenarios at other points on the right hand boundary of the oscillatory region appear to be similar to that at point C.

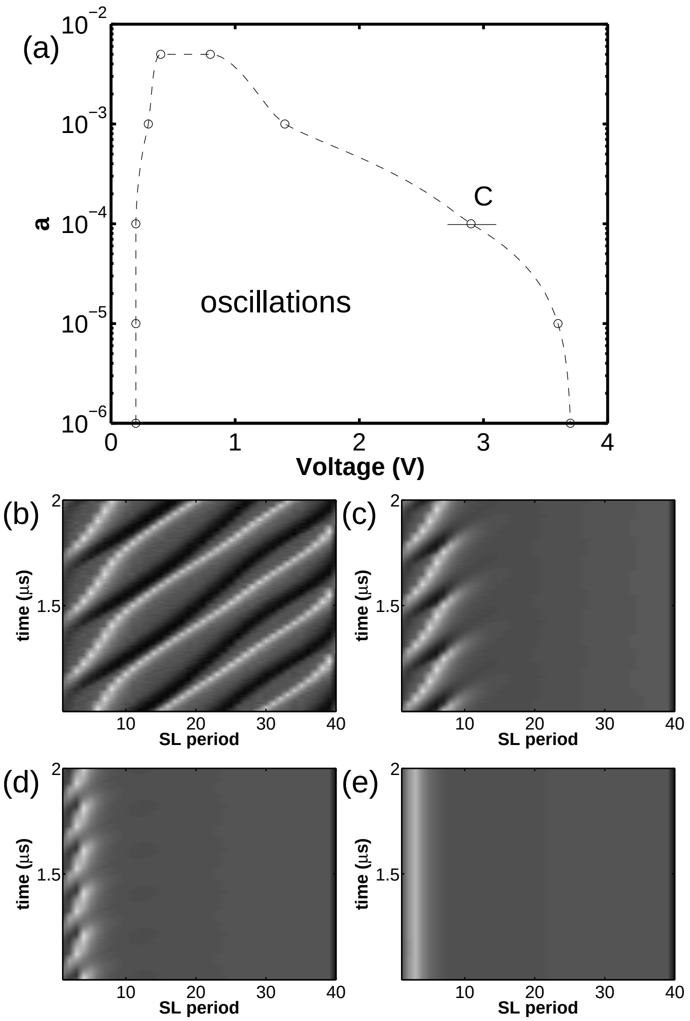

FIGURE 4.15: (a) Bifurcation diagram for $\sigma = 0.016\ (\Omega\mathrm{m})^{-1}$. Charge density distribution vs. time near bifurcation point C, $a = 1.00 \times 10^{-4}$ at (b) $U = 1.6$ V, (c) $U = 2.1$ V, (d) $U = 2.7$ V, and (e) $U = 3.0$ V.

4.5.3 Dynamical behavior vs. shunt conductivity parameter b

The above discussion focuses only on varying the connectivity parameter a with a shunt of high conductance. It is also possible to change other parameters of the shunt, such as the conductivity parameter b in the shunt. A bifurcation diagram can be plotted for b versus U with fixed $a = 1.00$ and $\delta_x = 200$ nm, and it is similar to that shown in Fig. 4.9, with an oscillatory regime between $b \approx 4.5 \times 10^{-8}$ and 4.5×10^{-7}.

Another possible control parameter is the width of the shunt. Simulation shows that only when the width of the shunt is narrower than about 1×10^{-4} nm, which is unrealistically small, the superlattice starts to have oscillation. The oscillatory region for a in Fig. 4.9 and 4.15 is almost not affected when b and δ_x are above certain values so that the current between the shunt and the superlattice can always be supported by the shunt. In reality, δ_x and b should be kept as low as possible to reduce the power dissipated in the shunt and minimize heat production.

4.6 Conclusion

We have theoretically studied the effect of a shunting side layer parallel to a semiconductor superlattice, and find that such a structure can have an almost uniform electric field over the entire structure even when biased in the negative differential conductivity (NDC) region. However, even for a shunt with high conductivity and strong connection to the superlattice, the field in the superlattice can be stabilized only for structures with relatively small lateral extent. As the lateral size L_x becomes larger, the lateral current in the quantum well loses the ability to deplete the extra current coming from the emitter and the field becomes nonuniform. For a sufficiently thin superlattice whose lateral dynamics is uniform, the connection between the shunt and the superlattice and the conductivity of the shunt determines the dynamics in the superlattice. We have also established the bifurcation diagrams for superlattices for different values of the shunt parameters and identified the presence of both local (Hopf) and global (SNIPER) bifurcations.

Although the microscopic nature of electronic transport in weakly-coupled superlattices is different than for strongly-coupled superlattices, the NDC property is known to produce similar dynamics in both types of structures when they are not shunted. Thus, it seems plausible that for suitable shunt connectivity and superlattice lateral width that a stronly-coupled superlattice might also be stabilized with a shunting side layer. This could enable the realization of a superlattice-based THz oscillator.

5

The superlattice-based THz oscillator

The gain for Terahertz (THz) radiation in semiconductor superlattices and its relation to Bloch oscillations has been theoretically studied since the 1970s,[23, 51] suggesting that the superlattice can serve as an active medium for THz radiation. However, such a device has never been realized due to space-charge instabilities associated with NDC. One major motivation for this work in Chapter 4 is to identify conditions that would permit the realization of the superlattice-based THz oscillator. We have shown the possibility that field domains in the weakly-coupled superlattice can be suppressed by the side shunting layer. However, the Bloch oscillation leading to the terahertz gain occurs in strongly-coupled superlattices with miniband structure. In contrast, the resonant tunneling model describes weakly-coupled superlattices.

In this Chapter, the previously developed method is adapted to model transport in the strongly-coupled superlattice with a shunting layer. We will also discuss the problems that still need to be solved for practical devices and compare this method to other proposals for SL-based THz oscillators.

5.1 Overview

Theoretical work by Esaki and Tsu [23] in 1970 was the first to propose a Bloch oscillator based on a superlattice structure. In that paper, they derived current-voltage (I-V) characteristics of a superlattice which showed negative differential conductivity (NDC) associated with Bloch oscillations[76, 77] of the miniband electrons under a DC bias. However, direct observation of Bloch oscillations in solid state materials is difficult due to decoherence caused by electron scattering. However, recent work in trapped atomic gases has shown possibilities to observe Bloch oscillations[78]. In Chapter 2, we have already shown that miniband electron transport leads to associated amplification of high frequency signals thereby suggesting an alternative means of THz oscillation. This is was first predicted by Ktitorov, Simin and Sindalovskii [51] in their important early work. This dynamic negative high-frequency differential conductivity remains negative up to the Bloch frequency ω_B and reaches a resonance minimum at a frequency closely below ω_B, suggesting that the superlattice may serve as an active medium for THz radiation, see Fig. 2.7.

However, no such devices have been realized to date more than three decades after Esaki-Tsu proposal because the NDC causes space-charge instability. Although Bloch oscillations have been observed experimentally in undoped superlattices [79] by studying optical dephasing of Wannier-Stark ladder[80] excitations using degenerate four-wave mixing,[81, 82] the power of coherent THz emission is very small. However, these experiments have shown that the frequency of the emission is tunable by simply changing the applied voltage.[83, 84] For high current densities, the space-charge instability causes moving charge accumulation layers (CALs) and charge depletion layers (CDLs) and thus the superlattice exhibits oscillations similar to the Gunn effect.[21] While devices based on these oscillations may operate in the microwave range, they do not extend to the THz region.[24]

The lack of suitable THz radiation sources and detectors hampers the technological exploitation of the frequency regime spanning from 300 GHz to 10 THz. Quantum cascade laser devices have been shown to operate in the THz range for temperatures up to 164 K.[85] On the other hand, if superlattice-based Bloch oscillators could be successfully realized they might be expected to have certain advantages relative to the quantum cascade structures.[53] Recently, rapid progress in THz technology [86, 87] including biomedical sensing, three-dimensional imaging and chemical agent detection has attracted renewed attention to Bloch oscillators. Some structures have been proposed to stabilize the field in the superlattice against NDC-related instabilities. One scheme theoretically proposed by Hyart *et al.*[88] is the dc-ac-driven superlattice which requires the presence of an initial THz pump. The superlattice is biased in the NDC region under a DC electric field, initially superposed with an AC pump electric field which stabilizes the field distribution.[89] Then the initial pump field can be gradually turned off when THz oscillation has been already established in the superlattice. Alternative schemes that do not require a THz pump include the use of quasistatically modulated microwave bias[90] or parametric amplification.[91, 92] Another suggestion is to stack a few short superlattices, where domains are not able to form.[93] These short superlattices are separated by heavily doped material, and an increase in terahertz transmission at dc bias has been observed.

Yet another scheme is to open a shunting channel parallel to the superlattice, similar to a method that has been used to stabilize tunnel diode circuits.[94, 95] Daniel *et al.* [64] used a distributed nonlinear circuit model to simulate the electric field domain suppression in a superlattice. They have shown that the shunt is able to suppress the voltage inhomogeneity above a critical bias voltage which depends on the shunt width, the superlattice width, and the shunt resistivity. However, the circuit model does not include aspects of the electronic tunneling transport that appear to play an important role in superlattice behavior. The model possesses only a global coupling since the elements are connected in series and the $I - V$ characteristic of each element is fixed. On the other hand, the superlattice model has a more complex structure that has both a global coupling due to the applied voltage constraint as well as a nearest neighbor coupling arising from the varying charge densities that dynamically change the local current density vs. field ($J - F$) characteristics. As a result, the nonlinear circuit model of Daniel *et al.* is not able to exhibit connected field domains or current self-oscillations that are observed in superlattice structures both theoretically and experimentally.[33]

In similar work by Feil *et al.*,[96] a side layer is grown on the cleaved edge of a lightly doped GaAs/AlGaAs superlattice, such that a 2D electron gas is formed at the interface between the superlattice and the side layer. The lightly doped superlattice serves two purposes: (i) to provide a modulated potential for the 2D electron gas at the interface so that under this periodic potential, the electron gas becomes a *surface superlattice* with one lateral dimension; (ii) to provide a uniform field to this surface superlattice since a lightly doped superlattice can maintain a uniform field under external bias. While the suppression of field instabilities has been reported in this type of superlattice, it is still not clear whether this lateral structure will be useful as a THz oscillator.

5.2 The shunted strongly-coupled superlattice model

In last chapter, we studied the weakly-coupled superlattice with a shunting side layer. In this chapter, we use develop a similar model to study the effect of the shunt on the strong-couple superlattice. The structure is shown in Fig. 5.1(a). The superlattice is grown along the z direction and has lateral extent in the x direction from 0 to L_x. The extent in the y direction is assumed large. The shunt can be grown by cleaved-edge-technique and is located at $x < 0$ with width L_s. The system evolves following the charge continuity equation:

$$e\,\dot{n}(x,z,t) = -\nabla\cdot\mathbf{j} = -\frac{\partial j_x}{\partial x} - \frac{\partial j_z}{\partial z}, \tag{5.1}$$

and the Poisson equation

$$\nabla\cdot\mathbf{F} = \frac{\partial F_x}{\partial x} + \frac{\partial F_z}{\partial z} = e\,(n - N_D), \tag{5.2}$$

where $e < 0$ is the electron charge, n (N_D) is the electron (ionized donor) density, j_z is the vertical current density along the z (growth) direction, j_x is the lateral current density, and $\mathbf{F}$ denotes the electric field.

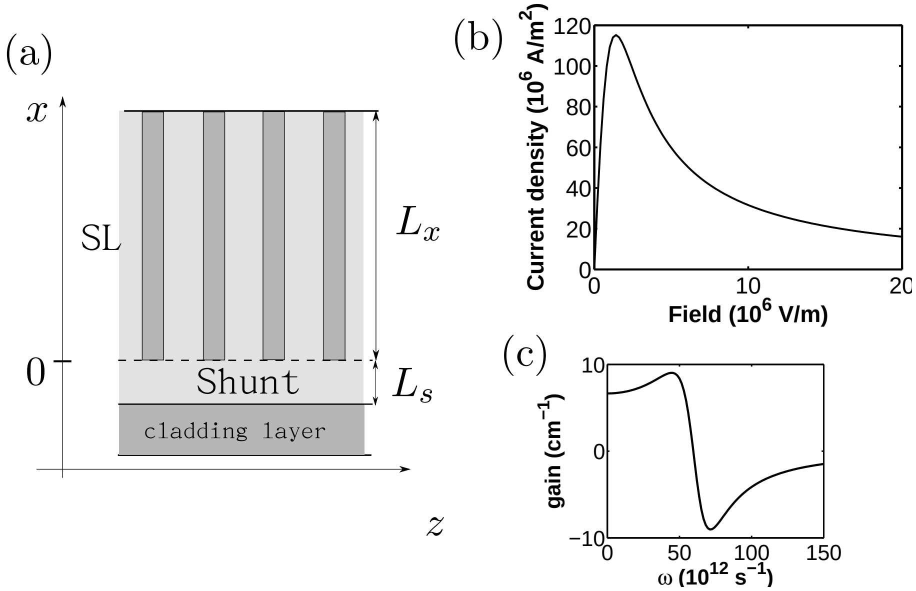

FIGURE 5.1: (a) Schematic of the device structure: light shaded area denotes quantum wells and the shunt and dark shaded area denotes barriers and the shunt clapping layer. (b) The $J - F$ characteristic and (c) gain profile for Structure 1.

In chapter 2, we have shown the local drift velocity $v(F_z)$

$$v(F_z) = \frac{2v_M F_s}{1+F_s^2}\,, \qquad F_s = F_z/F_M, \tag{5.3}$$

where F_z denotes the z component of the electric field. Thus the vertical current inside the superlattice is

$$j_z = e\,v(F_z)\,n - eD_{\parallel}(F_z)\,\frac{\partial n}{\partial z}, \tag{5.4}$$

where $D_{\parallel}$ is field-dependent diffusion constant

$$D_{\parallel}(F_z) = \frac{k_B T}{e}\mu_z = \frac{2k_B T v_M}{eF_M(1+F_s^2)}. \tag{5.5}$$

The drift part of the current follows a curve shown in Fig. 5.1(b). The negative differential conductivity in this current-field $(J-F)$ characteristic is associated with spacio-temporal instability. Moving field domains and charge monopole or dipole waves form, causing current self-oscillation. These have been well studied in Gunn diodes and unshunted strongly-coupled superlattices.[38] At the emitter, the tunneling current is Ohmic with contact conductivity σ:

$$j_z(z=0) = \sigma F_z(z=0). \tag{5.6}$$

The lateral current is also of drift-diffusion form:

$$j_x = e\,\mu\,nF_x - e\frac{\partial(D_\perp n)}{\partial x}, \tag{5.7}$$

where F_x denotes the x component of the electric field.

Using the same numerical method developed in Chapter 4, the shunt occupies one row of grid points in the simulation and has the same doping density as the superlattice. The charge continuity equation is similar, but the drift part of the vertical current is linear in F_z:

$$j_z^{(s)} = e\,\mu_s\,nF_z - e\frac{\partial(D_s n)}{\partial z}, \tag{5.8}$$

where $\mu_s = \mu$ and $D_s = D_\perp = D$ if the quantum wells and the shunt are made of the same material with bulk diffusion constant $D = k_B T\mu/e$.

Similar to the shunted weakly-coupled superlattices, the system has multiple time scales: The dynamics in the shunt and in the lateral direction $\epsilon_0\epsilon_r/(e\mu N_D) \approx 5$ fs for Structure 1 below is much faster than vertical dynamics in the strongly-coupled superlattice (10 ps to 10 ns). Therefore, the implicit method developed in Chapter 4 is also used.

For the structures studied here, we set the critical electric field value to $F_M = 1.4 \times 10^6$ V/m, achievable at room temperature in InAs/AlSb superlattices.[93] The value of peak drift velocity v_M is variable and depends on well and barrier widths of the superlattice.[38, 49] We bias the structures in the NDC region, with an average field $U/l = 6.67 \times 10^6$ V/m, where the total applied voltage $U = 12$ V is held constant and $l = 1.8$ μm is the length of the superlattice in z direction. We find that excess charge associated with accumulation or depletion layers in the superlattice moves laterally into the shunt mainly through diffusion,[97] so the diffusion constant $D_\perp$ needs to be sufficiently high for the field to be stabilized. Since $D_\perp = \frac{k_BT}{e}\mu$, we can enhance the diffusion process by working at room temperature, $T = 300$ K. We assume a mobility $\mu = 2$ m^2/Vs, achievable using InAs quantum wells.[98, 99, 100]

We have found that the excess charge associated with accumulation or depletion layers in the superlattice move into the shunt mainly through diffusion,[97] so the diffusion constant $D_\perp$ in the lateral direction needs to be sufficiently high for the field to be stabilized. Since $D_\perp = \frac{k_BT}{e}\mu$, to enhance the diffusion process, we set the temperature at room temperature, $T = 300$ K and the mobility $\mu = 2$ (m^2/Vs), which is achievable using InAs quantum wells.[98, 99, 100]

The parameters for the structures are listed in Table. I. There are two sets of N_D and v_M, corresponding to different current density and absorption (gain). The gain can be calculated through a semiclassical model at room temperature:[101]

$$g = -\frac{ed}{n_r\epsilon_0 c}\frac{j_{dc}(eFd + \hbar\omega) - j_{dc}(eFd - \hbar\omega)}{2\hbar\omega}. \tag{5.9}$$

The $J-F$ characteristic and gain for Structures 1-3 and 6 are shown in Fig.5.1(b),(c). The maximum value of the gain spectrum is about 9 (cm^{-1}) for these structures, while it is about 35 (cm^{-1}) for Structures 4 and 5.

	L_x (μm)	N_D (10^{23}m^{-3})	v_M (10^3m/s)	σ ($ev_M N_D/F_M$)
Structure 1	7	0.8	9	1
Structure 2	6	0.8	9	1
Structure 3	5	0.8	9	1
Structure 4	5	1.4	20	1
Structure 5	2.5	1.4	20	1
Structure 6	5	0.8	9	0.3

Table 5.1: Parameters used for the shunted strongly-coupled superlattice.

5.3 Results

The structure is biased at U with a uniform charge configuration $n = N_D$ everywhere as initial condition. The left column of Fig. 5.2 shows snapshots of field and charge configuration at $x = L_x$ and the right column shows snapshots of the electron configuration n for the whole structure after the system reaches static state or steady oscillation. The rows are for Structure 1, 2 and 3 respectively, which have different L_x, but are otherwise identical. Structure 1 has a wide lateral size and clearly demonstrates spatio-temporal instability. There is a static charge accumulation layer (CAL) near the emitter. At downstream (closer to the collector), alternating charge accumulation and depletion layers (CDLs) form, move downstream, disappear at the collector and reappear inside the superlattice. For wider superlattices, the transient process before the system reaches the steady state is very long. Multiple CALs and CDLs (dipole layers) are also found in the shunted weakly-coupled superlattice,[97] while only single dipole layer or monopole layer occurs in the superlattice without shunt.

As the lateral size becomes smaller, a region with relatively uniform field of strength as high as U/l start to emerge behind the CAL and CDL at the emitter, c.f., Structure 2 in Fig. 5.2(c),(d). As the lateral size becomes smaller than certain characteristic value, the field profile becomes static and uniform, shown in Fig. 5.2(e),(f). Near the emitter, the field and charge configuration are nonuniform. The amplitude of this spatial fluctuation decreases quickly and, downstream to this region, the field and charge configuration becomes uniform and the total charge density $n - N_D = 0$. The field in the uniform region is 6.7×10^6 (V/m), almost equal to the average value U/l.

The gain in Eq. 5.9 can be increased by increasing the doping density N_D or the peak drift velocity v_M. However, this also increases the vertical current in the superlattice and the field configuration becomes more difficult to stabilize, i.e., L_x needs to be smaller. So there is a trade-off between L_x and N_D, v_M. Comparing Structure 3 with Structure 4, we see that both have the same lateral size but Structure 4 oscillates similar to Structure 1, see Fig. 5.3(a). For this parameter set of superlattice, a uniform field appears for a much narrower superlattice with L_x approximately up to 2.5 μm, see Structure 5 in Fig 5.3(b).

In previous works, the contact conductivity σ was found to affect dynamical behavior for both weakly- and strongly-coupled superlattice.[44, 97, 33] Here we compare Structure 3 with Structure 6. Structure 6 has a much smaller σ. Figure 5.3(c),(d) show that a smaller σ decreases the spatial fluctuation of the upstream configuration but does not change the *healing* length, defined as the length of the nonuniform configuration region.

The shunt dissipates power without any optical gain, so to increase the wall-plug efficiency, the current flowing in the shunt should be kept as low as possible. Since NDC in the total current needs to be suppressed, given L_x, a *necessary* condition is that the conductance of the shunt only needs to be high enough for this goal.

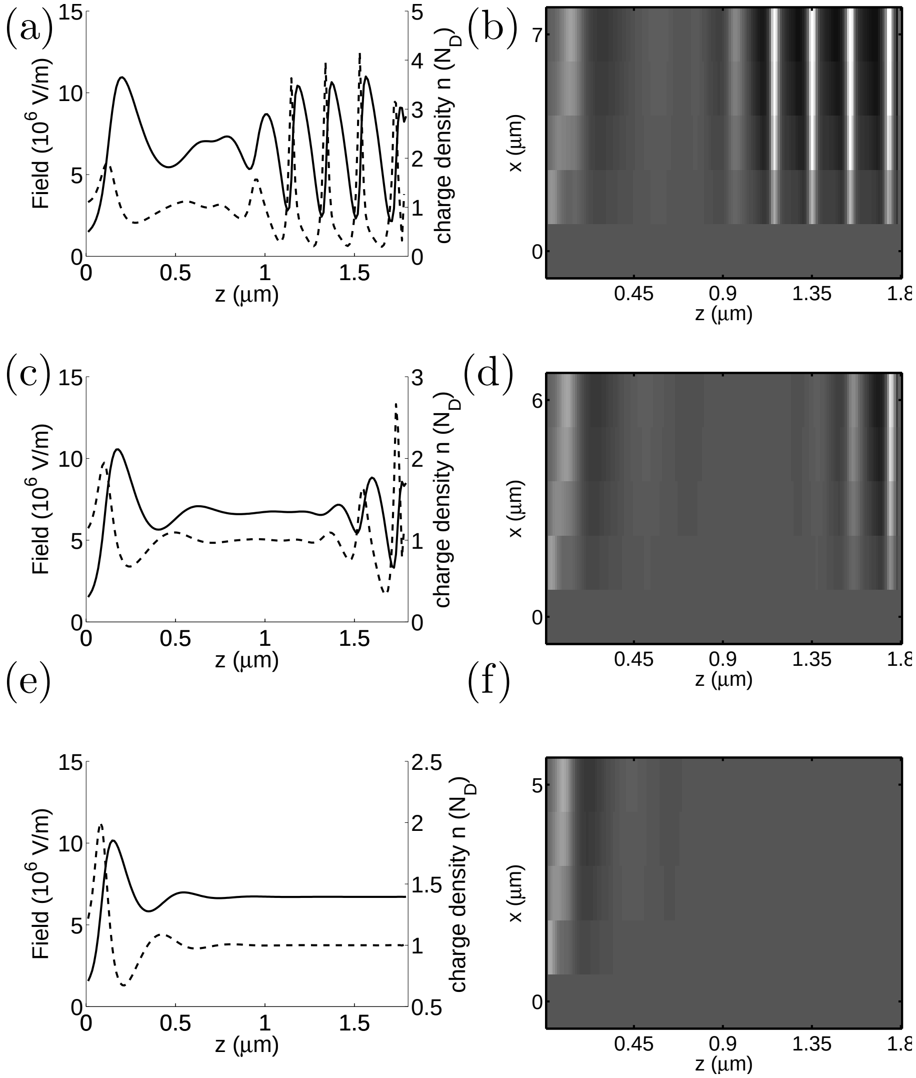

FIGURE 5.2: Snapshots of field (solid line) and electron density (dash line) configuration at $x = L_x$ (left column) and electron density distribution of the whole structure (right column) for (a),(b) Structure 1, (c),(d) Structure 2, (e), (f) Structure 3.

This is found to be a good estimate of the threshold width of the shunt. For the shunt to work, the maximum magnitude of negative differential conductance of the superlattice should be smaller than the conductance in the shunt: $\mu\, N_s\, L_s > g_m N_D\, L_x$ or

$$L_s > g_m L_x/\mu, \tag{5.10}$$

where $g_m = \max(|\partial v(F)/\partial F|)$ is the maximum of the absolute value of the NDC.

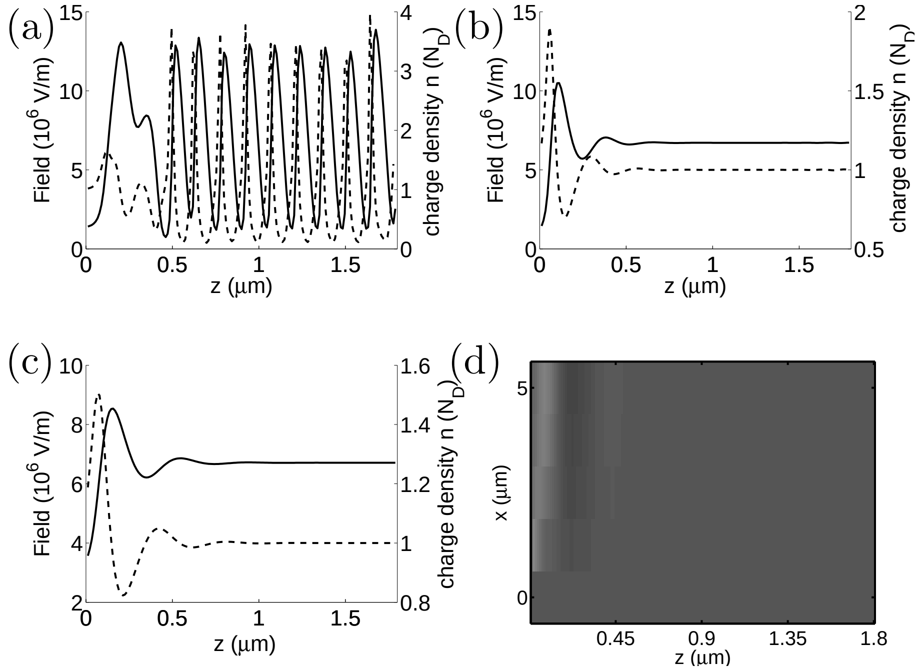

FIGURE 5.3: Snapshots of field (solid line) and electron density (dash line) configuration at $x = L_x$ for (a) Structure 4, (b) Structure 5, (c) Structure 6 and electron density distribution of the whole structure for (d) Structure 6.

Here, the doping density in the shunt N_s is equal to that in the superlattice N_D. For Structure 3, $L_s > 4$ (nm) using Eq. 5.10. Simulation shows that the threshold value of L_s is between 4 and 5 (nm). This length is even smaller than the period of the superlattice and quantum confinement will be significant in the shunt with this width.

5.4 Discussion

We have argued that the lateral diffusion is critical for the stabilizing the superlattice. Since the mobility D is proportional to $T\mu$, both T and μ need to be as high as possible. We also know that μ increases as T decreases, but the decrease of T has more impact on diffusion. For example, for bulk InAs, $\mu \approx 3$ m^{2}V^{-1}s^{-1} for $T = 300$ K and $\mu \approx 4$ m^{2}V^{-1}s^{-1} for $T = 77$ K. So we choose InAs for its high μ at room temperature. InAs belongs to a different group of III-V semiconductors, called the 6.1

Å family, whose band diagram is shown in Fig. 5.4. However, the mobility decreases steeply as the width of the quantum well decreases for narrow wells (≤ 10 nm) due to interface roughness scattering. This sets a lower limit for the width of quantum wells in the shunted superlattice for THz radiation.

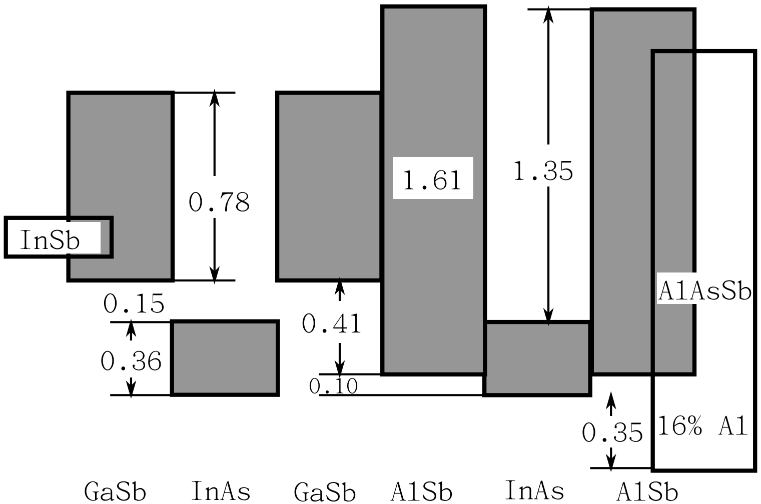

FIGURE 5.4: The energy band lineups of the 6.1 Å family semiconductor.[102]

In conclusion, we have numerically demonstrated that a strongly-coupled superlattice can have uniform field biased in the NDC region stabilized by a shunting side layer, thus enabling a device scheme that has positive gain in the THz regime. As the lateral size, the peak velocity v_M or doping density N_D becomes larger, the system becomes more difficult to stabilize and eventually loses stability to moving field domains. The diffusion in the lateral direction is essential for the stability and should be kept as large as possible. The contact conductivity does not have much impact on this stabilization scheme. The width of the shunt also needs to be large enough to suppress the NDC in the superlattice and to avoid quantum confinement effects.

6

Stochastic switching in weakly-coupled superlattices

In previous chapters, we studied deterministic processes in superlattices with different parameters and designs. We have seen that static field domains cause bistability in the overall electrical current level. In this chapter, we switch to another interesting topic, yet still relevant to NDC, stochastic switching between co-existing metastable states in superlattices. Intuitively, one of two states in the bistable region becomes ”less and less stable” near the end of the bistable region. In the presence of noise, the system can leave the less stable state and switch to the more stable state. The model for a superlattice with shot noise will be developed in this chapter and the switching process will be numerically simulated. Two major questions will be investigated: the statistics of the switching time and switching path.

6.1 Stochastic switching between bistable states

In this section, we will review the theories of stochastic processes, stochastic switching for a double well potential and the saddle node bifurcation. These are the major theories necessary for understanding the stochastic current switching in superlattices. More details on these topics can be found in Ref. [30].

6.1.1 Background and the Wiener process

Up to the end of the nineteenth century, classical mechanics from Newtonian mechanics to Lagrangian and Hamiltonian mechanics use deterministic differential equations to model natural processes. This kind of modeling and solutions are referred to as deterministic processes whose initial conditions determine the state of the system at any time in the future with absolute certainty.

However, this is not so, firstly, because in the microscopic regime, quantum mechanics tells us that the state of microscopic particles can only be determined probabilistically. Secondly, even in the macroscopic regime, probability theory is applied in statistical mechanics which explains uncertain processes such as fluctuation and diffusion.

For example, small pollen grains suspended in a fluid are found to wander irregularly, which is called Brownian Motion, named after a botanist Robert Brown who was the first to systematically investigate this phenomena. In mathematics, this is called the Wiener process. A Wiener process W_t is defined by the following properties:

1. $W_0 = 0$,
2. W_t is continuous,
3. Any increments of W_t in time $\Delta W = W_t - W_s$ has a normal distribution $N(0, t-s)$.

The third property also tells us that the variance of ΔW is

$$\langle \Delta W^2 \rangle = \Delta t = t - s. \tag{6.1}$$

6.1.2 *Langevin equation*

Stochastic processes can be modeled by incorporating random terms into differential equations. Such stochastic differential equations are called Langevin equations. The simple Langevin equation can often be written in the following form

$$\frac{dx}{dt} = A(x,t) + b(x,t)\xi(t), \tag{6.2}$$

where x is the dynamical variable to be solved, $A(x,t)$ and $b(x,t)$ are known functions of x and time t and $\xi(t)$ is the fluctuating random term which obeys

$$\langle \xi(t)\xi(t')\rangle = \delta(t-t'). \tag{6.3}$$

This kind of ideal fluctuation is called white noise which has no autocorrelation at different times. It can be shown that the integral of white noise ξ in time is the Wiener process[30], i.e.,

$$\int_0^t \xi(t')dt' = W(t), \tag{6.4}$$

or,

$$\xi dt' = dW. \tag{6.5}$$

Now we can rewrite Eq. 6.2 as

$$dx(t) = A[x(t),t]dt + \sqrt{B[x(t),t]}dW(t), \tag{6.6}$$

where $\sqrt{B[x(t),t]} = b(x(t),t)$.

The solution to Eq. 6.2, or equivalently Eq. 6.6, is a stochastic integral equation

$$x(t) - x(0) = \int_0^t A(x(s),s)ds + \int_0^t b(x(s),s)dW(s). \tag{6.7}$$

Since W is the Wiener process, the random variable $x(t)$ will be different for each realization.

6.1.3 Fokker-Planck equation

The Langevin equation describes the dynamical variable x directly. Another approach to stochastic processes is to ask the probability distribution of x at time t. This is described by the master equation if the state x of the system is discrete or Fokker-Planck equation if x is continuous. The Fokker-Planck equation (FPE) has the forward and the backward version.

The one dimensional forward FPE has the form:

$$\partial_t p(x,t|x_0,t_0) = -\partial_x[A(x,t)p(x,t|x_0,t_0)] + \frac{1}{2}\partial_x^2[B(x,t)p(x,t|x_0,t_0)], \tag{6.8}$$

which describes the *conditional probability* $p(x,t|x_0,t_0)$ of x at t given that the initial value $x = x_0$ at $t = t_0$, i.e., the initial condition is

$$p(x,t_0|x_0,t_0) = \delta(x - x_0) \tag{6.9}$$

and $t > t_0$.

It turns out that the backward FPE is more suitable for dealing with first passage time problems. It has the form:

$$\partial_t p(x',t'|x,t) = -A(x,t)\partial_x p(x',t'|x,t) - \frac{1}{2}B(x,t)\partial_x^2 p(x',t'|x,t), \tag{6.10}$$

which describes the *conditional probability* $p(x',t'|x,t)$ of x at t given that the *final* value $x = x'$ at $t = t'$, i.e., the *final* condition is

$$p(x',t'|x,t') = \delta(x - x') \tag{6.11}$$

and $t < t'$.

A major difference between the forward and the backward FPE is that the factors A and B as functions of the variables of interest, x and t, are inside the derivative in the forward case while outside the derivative in the backward case. Also the sign before the second derivatives are opposite for the two cases.

The magic of FPE is that both the forward and the backward cases describe the Langevin equation, Eq. 6.6, and the factors A and B are exactly the ones in Eq. 6.6[30]. So the FPE and the Langevin equation describe the same process from different point of views.

6.1.4 First passage time for a double well potential

Now assume that x is the coordinate of a particle which follows Eq. 6.6, thus Eq. 6.10 is also true for x. The particle is initially at x in the interval (a, b) at time $t = 0$. The probability that at time t the particle is still in (a, b) is

$$\int_a^b dx' p(x', t|x, 0) \equiv G(x, t). \tag{6.12}$$

With proper boundary conditions, this is also the probability that the time the particle leaves (a, b), $T \geq t$, i.e.,

$$\text{Prob}(T \geq t) = \int_a^b dx' p(x', t|x, 0). \tag{6.13}$$

For homogeneous processes (factors A and B are independent of t) whose probability approaches a stationary value $p(x, t) \to p_s(x)$ as $t \to \infty$ or as initial time $t_0 \to -\infty$, i.e., the process can be shifted in time, we can write

$$p(x', t|x, 0) = p(x', 0|x, -t) \tag{6.14}$$

and the backward FPE for $p(x', 0|x, -t)$ can be written for $p(x', t|x, 0)$ as

$$\partial_t p(x', t|x, 0) = A(x)\partial_x p(x', t|x, 0) + \frac{1}{2}B(x)\partial_x^2 p(x', t|x, 0). \tag{6.15}$$

Integrating the backward FPE with respect to x', one obtains

$$\partial_t G(x, t) = A(x)\partial_x G(x, t) + \frac{1}{2}B(x)\partial_x^2 G(x, t). \tag{6.16}$$

The mean first passage time $T(x) = \langle T \rangle$ is given by

$$T(x) = -\int_0^\infty t\ \partial_t G(x,t) dt. \tag{6.17}$$

Noting that

$$\int_0^\infty \partial_t G(x,t) dt = G(x,\infty) - G(x,0) = -1, \tag{6.18}$$

integrating Eq. 6.16 with respect to time t yields

$$A(x)\partial_x T(x) + \frac{1}{2}B(x)\partial_x^2 T(x) = -1. \tag{6.19}$$

Equation 6.19 is the equation for the mean first passage time to leave the interval (a,b) from x. It can be solved directly by integration. If a is reflecting and b is absorbing, i.e,

$$\partial_x G(a,t) = 0, \tag{6.20a}$$

$$G(b,t) = 0. \tag{6.20b}$$

So the boundary condition is $T(b) = 0$ and $\partial_x T(a) = 0$.

Now let's consider the particle moving in a double well potential shown in Fig. 6.1 according to the Langevin equation

$$\frac{dx}{dt} = -U' + \sqrt{2D}\xi(t), \tag{6.21}$$

or the corresponding FPE is

$$\partial_t p(x,t) = \partial_x[U'(x)p(x,t)] + D\partial_x^2 p(x,t). \tag{6.22}$$

The left boundary at $a \to -\infty$ is reflecting. Solving Eq. 6.19 with boundary conditions Eq. 6.20, ones obtains

$$T(x_1 \to b) = \frac{1}{D}\int_{x_1}^b dy \exp[U(y)/D] \int_{-\infty}^y \exp[-U(z)/D] dz, \tag{6.23}$$

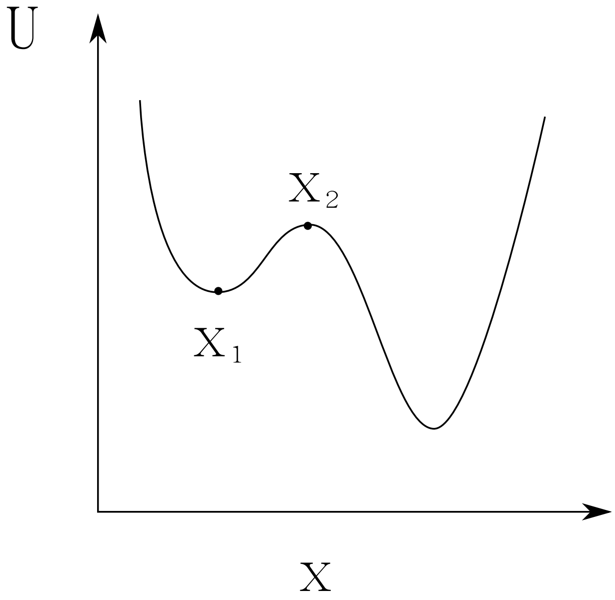

FIGURE 6.1: Double well potential

where $b > x_2$. If the potential barrier $U(x_2)$ is large compared to D, then the exponent $\exp(U(y)/D)$ sharply peaks at $y = x_2$, so a small domain near x_2 contributes to the integral $\int_{x_1}^{b} dy \exp[U(y)/D]$. For y near x_2, the integral $\int_{-\infty}^{y} \exp[-U(z)/D]dz$ is almost a constant. So Eq. 6.23 can be written as

$$T(x_1 \to b) \approx \frac{1}{D} \int_{x_1}^{b} dy \exp[U(y)/D] \int_{-\infty}^{x_2} \exp[-U(z)/D]dz. \tag{6.24}$$

Now it becomes a product of two integral rather than a two dimensional integral. The potential can be expanded locally near x_1 as

$$U(x) \approx U(x_1) + \frac{1}{2}\left(\frac{x - x_1}{a_1}\right)^2 \tag{6.25}$$

and near x_2

$$U(x) \approx U(x_2) - \frac{1}{2}\left(\frac{x - x_2}{a_2}\right)^2 \tag{6.26}$$

The first integral is dominated at x_2, so plug Eq. 6.26 into it and raise x_1 and b to $-\infty$ and ∞, respectively. The second integral is dominated at x_1, so plug Eq. 6.25

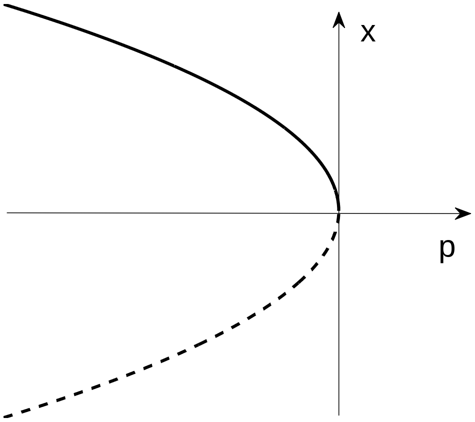

FIGURE 6.2: Illustration of saddle node bifurcation. The fixed points of Eq. 6.29 are plotted versus parameter p.

into it and raise x_2 to ∞. Then one obtains

$$T(x_1 \to b) \approx 2a_1a_2\pi \exp\{[U(x_2) - U(x_1)]/D\}. \tag{6.27}$$

6.1.5 Saddle node bifurcation

For an ordinary differential equation system:

$$\dot{\mathbf{x}} = f(\mathbf{x}, \mathbf{p}) \tag{6.28}$$

where $\mathbf{x}$ is a vector whose evolution in time follows the above equation and $\mathbf{p}$ is one or more control parameters. The behavior of the system, e.g., stable or unstable fixed points or limit cycles, may be qualitatively changed by varying the control parameter(s), which is called a bifurcation.

The saddle node bifurcation is one of simplest and most common bifurcations, where a stable fixed point and an unstable fixed point collide and annihilate each other. This can be written in the simplest normal form

$$\dot{x} = -x^2 - p. \tag{6.29}$$

Then the stable and unstable fixed points are plotted versus control parameter p in Fig. 6.2. We can see that for $p < 0$ there are two fixed points, one stable and one unstable. At $p = 0$, there is only one fixed point. For $p > 0$, there are no fixed points. This behavior can also occur in high dimensional systems, which can be reduced to a relatively simple normal form with the help of the center manifold theorem[103].

6.2 Sequential tunneling model with shot noise

In electronic devices, noises always accompany electrical currents, causing fluctuation and uncertainty. There are different kinds of noises, such as thermal noise (also called Johnson noise) and shot noise[104]. Thermal noise is due to the thermal motion of free electrons. Its intensity decreases as the temperature drops. At low temperature, shot noise dominates in superlattices.

The electric current in superlattices is formed by the tunneling of electrons through barriers. Due to the discrete nature of electrons, the tunneling of electrons constitutes a series of independent, random events. To be specific, this is a Poisson process with average rate $\bar{I}/e$, where $\bar{I}$ is the average current. So the current can be written as

$$I(t) = e \sum_j \delta(t - t_j) \tag{6.30}$$

where t_j are the times when the tunneling of electron occurs. The autocorrelation of current is defined as

$$R(t') = \lim_{T\to\infty} \frac{1}{T} \int_0^T dt\ I(t)I(t + t'), \tag{6.31}$$

so the autocorrelation of Eq. 6.30 is

$$\begin{aligned} R(t') &= \lim_{T\to\infty} \frac{e^2}{T} \sum_j \int_0^T dt\ \delta(t-t_j)\delta(t-t_j+t') \\ &= \lim_{T\to\infty} \frac{e^2}{T} \sum_j \delta(t') \\ &= e\bar{I}\delta(t'). \end{aligned} \tag{6.32}$$

In the last step, we used the fact that as $T \to \infty$, the summation $\sum_j \to T\bar{I}/e$.

The Fourier transformation of $I(t)$ is

$$I'(\omega) = \int_0^T dt\ e^{-i\omega t} I(t). \tag{6.33}$$

Then the spectrum is defined by

$$S(\omega) = \lim_{T\to\infty} \frac{1}{2\pi T} |I'(\omega)|^2. \tag{6.34}$$

It is easy to see that the spectrum is the Fourier transformation of autocorrelation

$$S(\omega) = \frac{1}{2\pi} \int_{-\infty}^{\infty} e^{-i\omega t} R(t)\ dt, \tag{6.35}$$

or,

$$R(t) = \int_{-\infty}^{\infty} e^{i\omega t} S(\omega)\ d\omega. \tag{6.36}$$

This is the well known Wiener-Khinchin theorem[30]. So the spectrum of shot noise is

$$S(\omega) = 2e\bar{I}. \tag{6.37}$$

Adding a noise term to the superlattice model yields:

$$J(t) = \varepsilon \frac{dF_i}{dt} + J_{i\to i+1} + J^{(r)}_{i\to i+1}(t). \tag{6.38}$$

From Eq. 6.32, the noise current has autocorrelation

$$\begin{aligned}\langle I^{(r)}_{i\to i+1}(t) I^{(r)}_{j\to j+1}(t')\rangle &= \langle S\cdot J^{(r)}_{i\to i+1}(t) S\cdot J^{(r)}_{j\to j+1}(t')\rangle &(6.39)\\ &= eI_{i\to i+1}\delta(t-t')\delta_{ij}, &(6.40)\end{aligned}$$

where S is the cross sectional size of the superlattice. So,

$$\begin{aligned}\langle J^{(r)}_{i\to i+1}(t) J^{(r)}_{j\to j+1}(t')\rangle &= \frac{eI_{i\to i+1}\delta(t-t')\delta_{ij}}{S^2} &(6.41)\\ &= \frac{eJ_{i\to i+1}\delta(t-t')\delta_{ij}}{S} &(6.42)\\ &= B_i^2\langle \xi_i(t)\xi_j(t')\rangle &(6.43)\end{aligned}$$

where $B_i^2 = \frac{eJ_{i\to i+1}}{S}$ and $\langle \xi_i(t)\xi_j(t')\rangle = \delta_{ij}\delta(t-t')$. It is important to note the shot noise term becomes relatively more important as the device cross section S decreases. This means that fluctuation effects will be accentuated in SL samples with small cross section. Most work recorded in this Chapter will use a sample size with diameter 60μm, except for the following single noise source.

Thus

$$J(t) = \varepsilon\frac{dF_i}{dt} + J_{i\to i+1} + B_i\xi_i(t), \quad i = 0, ..., N. \tag{6.44}$$

Summing Eq. 6.44 over all periods yields

$$(N+1)J(t) = \frac{\varepsilon dV}{l\ dt} + \sum_{i=0}^{N}(J_{i\to i+1} + B_i\xi_i(t)), \tag{6.45}$$

and plug it back into each equation of Eq. 6.44 yields:

$$\begin{aligned}dF_i &= \frac{1}{(N+1)l}\frac{dV}{dt}dt + \frac{1}{\varepsilon}\left(\frac{1}{N+1}\sum_{j=0}^{N} eJ_{j\to j+1} - eJ_{i\to i+1}\right)dt\\ &\quad + \frac{1}{\varepsilon}\left(\frac{1}{N+1}\sum_{j=0}^{N} B_j\Delta W_j(t) - B_i\Delta W_i\right). &(6.46)\end{aligned}$$

where $W_i = \int_0^t \xi_i \cdot dt'$ are Wiener processes. If we hold the voltage as a constant, the first term on the right hand side vanishes. We simulate the system using Heun's method [105].

The approach here includes spatial variation along only one dimension, i.e., along z-direction. The dynamical variables in the lateral $x - y$ plane are assumed to be uniform. This is only true for very small lateral size superlattice. When the lateral size becomes bigger, fluctuation at different positions in the lateral direction can be different causing laterally nonuniform charge density and field. Drift-diffusion process also occurs in the lateral direction. The deterministic drift-diffusion model of superlattice with lateral dynamics was first studied in Ref. [66] and later investigated with a more complicated structure by me in Ref. [97]. Direct numerical simulation of such structure with noise has never been performed.

6.2.1 Fluctuation due to single noise sources

In reality, shot noise exists at each barrier. However, in simulation, we can turn off noise at any barriers. The single noise effects are shown in Fig. 6.3. To increase the noise effect, we use a smaller cross-sectional area size with diameter 10μm. The noise turned on in the low field domain (at E_{10} in Fig. 6.3) causes fluctuation of E_{36}. Interestingly, the fluctuation of E_{36} due to noise sources in the low field domain is roughly additive. However the noise in the high field domain causes no E_{36} fluctuation. The reason for this behavior is still not clear.

6.3 Scaling behavior of the lifetime of the metastable state

6.3.1 Switching time distribution

In previous works, the deterministic sequential tunneling model for superlattices has successfully produced static current branches in $J - V$ curves. Figure 6.4(a) shows a typical $J - V$ curve with $\sigma = 0.08$ $(\Omega\text{m})^{-1}$ and bistability is clearly seen for up-

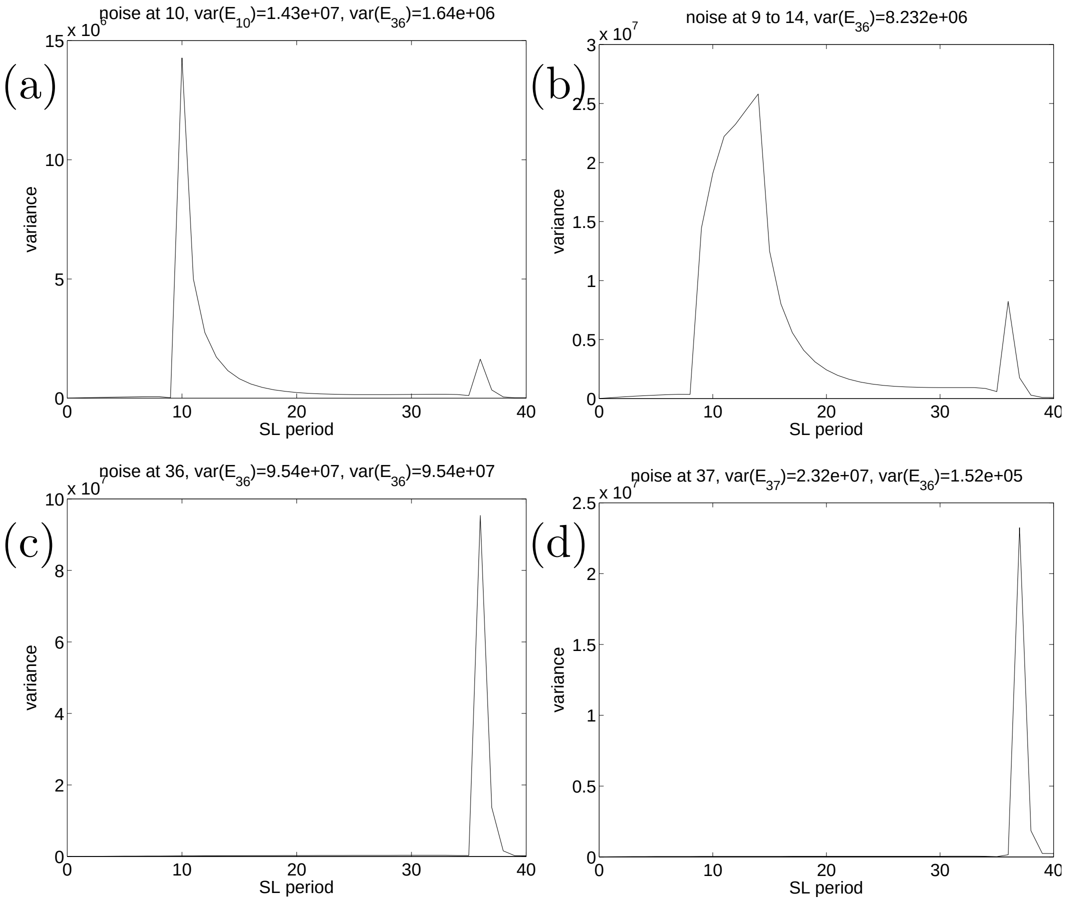

FIGURE 6.3: Fluctuation due to single noise sources. $V = 0.47$ V. Diameter is 10 μm. Shot noise turned on only (a) at 10th well, (b) from 10th to 15th well, (c) at 36th well, (d) at 37th well.

sweep and down-sweep of the applied voltage. Each current branch corresponds to a unique spatial configuration of electric field. The field and charge configuration for $V = 0.47$ V is shown in Fig. 6.4(b), where we see that the accumulation layer is located at the 37th period. The bistability at the end of the current branch means that the accumulation layer can either be in 37th or 36th period for the same applied voltage. We find that $V_{\rm th} = 0.53903\ V$ where $V_{\rm th}$ denotes the voltage corresponding to the end of the 4th current branch, cf. Fig. 6.4(a).

Consider now the initial condition where one starts with the stable field configuration corresponding to $V_0 = 0.47$ V, where there is no bistability, and then switches

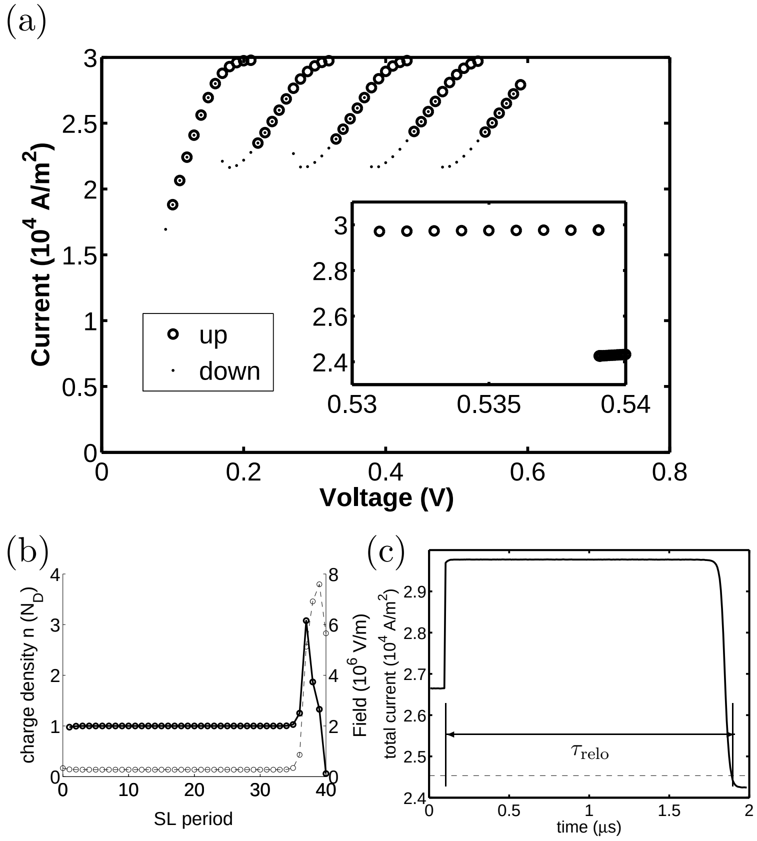

FIGURE 6.4: (a) The deterministic $J-V$ curve for superlattice with contact conductivity $\sigma = 0.08$ $(\Omega\text{m})^{-1}$ and other parameters defined in Ref [44]. (b) The field (solid line) and the charge density (dash line) configuration for $V = 0.47$ V. (c) The current trace for a typical pulsed switching process.

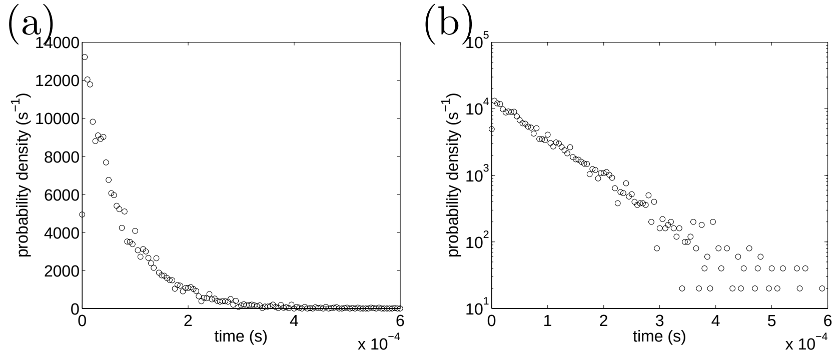

FIGURE 6.5: Switching time distribution at $V = 0.5388$ V. a) Linear scale. b) Logarithmic scale.

abruptly to the voltage to V near the end of the *same* current branch. If there is no noise, the system relaxes deterministically to the upper branch and remains there. However, if we add shot noise to the tunneling current, the current stays on the upper branch for a period of time τ_{relo} and then switches to the lower branch which is globally stable. The switching time τ_{relo} is a type of first passage time (FPT) and, in this paper, we refer to it as the lifetime of the upper branch. Figure. 6.4c shows a typical current trace in response to a step function in applied voltage. The initial upward jump of the current is due to the jump of voltage from V_0 to V. After this, the current is nearly constant until the system reaches a saddle point at which point the current makes a smooth but relatively rapid transition to the low current states. During the switching process, the accumulation layer moves backward by one period of the superlattice. We refer to this initial state preparation scheme with an initial jump of applied voltage as the *pulsed IC*, and note that this approach is easily realized in experiments.

The distribution of τ_{relo} for $V = 0.5388$ V is shown in Fig 6.5, and it clearly has an exponential tail. This suggests that the switching process is well approximated as a Poisson process. As V gets closer to V_{th}, the distribution becomes a skewed Gaussian distribution and the *mean* switching time becomes shorter. Figure 6.6 shows the switching time distribution for $V = 0.5392$V and 0.54 V. It can be seen that the switching time distribution is still skewed when V is beyond the end of the current branch. It becomes a normal distribution when V becomes even larger.

If one simulates an ensemble of identically prepared systems with different noise realizations, one can use this to generate histograms of charge density in the 37th well n_{37} at various instances of time after the initial pulse. We find that for a FPT distribution with exponential tail, the histogram is clearly bimodal, and for normal FPT distribution, the histogram is unimodal. Histograms are plotted in Figs. 6.6c,d for V=0.5392 and 0.54 V, respectively. As the final voltage passes significantly

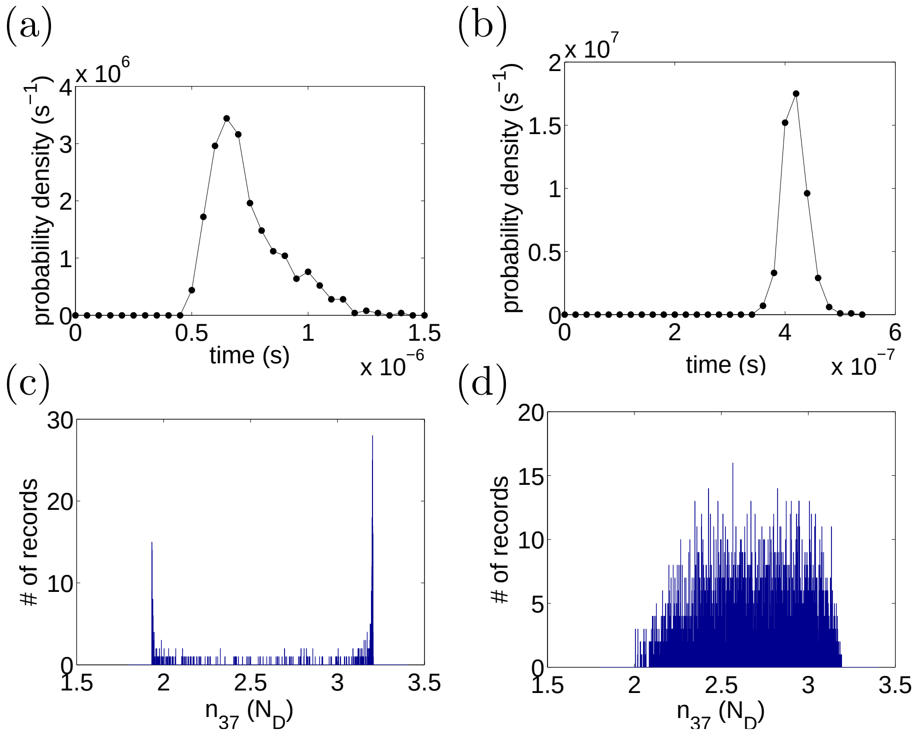

FIGURE 6.6: Switching time distribution at a) $V = 0.5392$ V, b) $V = 0.54$ V. snapshots of histogram of charge density in 37 th well, n_{37}: c) $V = 0.5392$ V at 0.4410 (μs), d) $V = 0.54$ V at 0.2278 (μs)

beyond the end of the current branch, the distribution tends to a Gaussian form.

6.3.2 3/2 scaling law

It has been shown that the mean first passage time from one stable fixed point to the other in a one-dimensional double well potential is proportional to $\exp(\Delta U/D)$ [30] a result that is sometimes called the Kramer formula. Here, ΔU is the height of the potential barrier and D is the noise intensity or diffusion constant. For $V < V_{\mathrm{th}}$, there exist bistable states and there may exist a potential barrier in the direction of the reaction coordinate s illustrated in Fig. 6.7. When V is close to V_{th}, the potential near the metastable state s_1 can be written in the following form to the 3rd order of s:

$$U(s;V) = K\left(-\frac{s^3}{3} + A(V)\,s\right), \tag{6.47}$$

where $K > 0$ is a constant and the variable $A(V)$ can be expanded near V_{th} as

$$A(V) = A(V_{\text{th}}) + A'(V_{\text{th}})(V - V_{\text{th}}) + O(V - V_{\text{th}})^2. \tag{6.48}$$

To find the fixed point for a given V, set $dU/(K\,dr) = -s^2 + A = 0$ and $s = \pm\sqrt{A}$. When the saddle-node bifurcation occurs at V_{th}, the two fixed points s_1 and s_2 collide and only one fixed point $s = 0$ is left. So $A(V_{\text{th}}) = 0$. For $V < V_{\text{th}}$, there exist two fixed points, so $A'(V_{\text{th}}) = -\beta < 0$. Then the metastable state is $s_1 = -\sqrt{A}$ and the saddle point is $s_2 = \sqrt{A}$. Subsequently, for $V > V_{\text{th}}$, there is no fixed point. When $V < V_{\text{th}}$, we can find the potential barrier

$$\Delta U = U(s_2) - U(s_1) = K\frac{4}{3}A^{3/2}. \tag{6.49}$$

Substituting $A(V) = \beta(V_{\text{th}} - V)$ into the above equation, the mean first passage time $\tau \propto \exp(\Delta U/D)$ now becomes

$$\tau \propto \exp\left(\frac{4K\beta^{3/2}}{3D}(V_{\text{th}} - V)^{3/2}\right). \tag{6.50}$$

Or simply,

$$\tau \propto \exp\left(\frac{1}{D_V}(V_{\text{th}} - V)^{3/2}\right). \tag{6.51}$$

From the derivation, we can see that this is only true for $V_{\text{th}} - V$ small. Meanwhile, the original relationship Eq. 6.27 $\tau \propto \exp(\Delta U/D)$ is only true for $\Delta U \gg D$,which requires $V_{\text{th}} - V$ not too small. For $V_{\text{th}} - V$ not too large, the cubic potential approximation will fail. So $V_{\text{th}} - V$ can not be too small or too large. Also, when deriving the relationship $\tau \propto \exp(\Delta U/D)$ itself, a few approximations have been made, see Sec. 6.1.4. Finally, the calculated mean switching time is a Monte Carlo estimate with non-zero variance for a finite number of trials. These factors all may contribute to the result that the exponent α is not exactly 1.5.

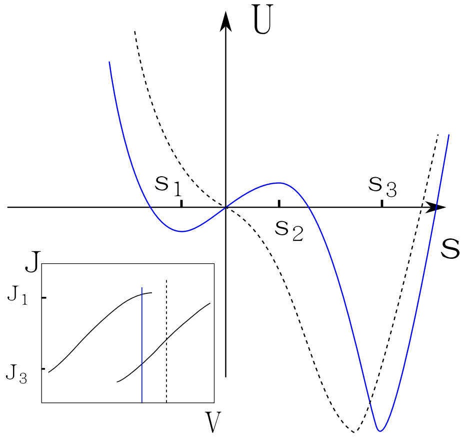

FIGURE 6.7: Schematic of the potential for the saddle-node bifurcation for $V < V_{\mathrm{th}}$ (red solid line) and $V > V_{\mathrm{th}}$ (black dashed line).

6.3.3 The statistical model

After we obtain the distribution for the first passage time distribution, it is easy to calculate the sample mean first passage time τ and its standard deviation s_d for applied voltage V. Figure. 6.8 shows τ vs. V using the pulsed scheme described in Sec. 6.3.1. For comparison, we also plotted the simple fitting of linear and quadratic relationship. The fitting is only applied to the five largest τ value points, i.e., the leftmost five points in Fig. 6.8. The reason not to include the points closer to V_{th} is that when deriving the scaling behavior, the effective potential barrier is large compared to effective noise, i.e., the control parameter of the bifurcation is not too close to its threshold value.

It has been shown that for a one-dimensional double barrier structure in which lateral dynamics is neglected, the mean first passage time behaves as $\log \tau \propto (V_{\mathrm{th}} - V)^{3/2}$. From Fig. 6.8, it is difficult to tell if the exponent is 1.5. So we need to resort to more rigorous statistical methods to fit the simulated τ vs. V. According to central limit theorem, the sample mean τ_{obs} of simulated first passage time τ_{relo} for each V follows a normal distribution $N(\tau(V), \sigma^2(V))$ and the variance $\sigma^2(V) = \sigma^2_{\mathrm{relo}}(V)/n$, where $\sigma^2_{\mathrm{relo}}(V)$ is the variance of τ_{relo} and can be estimated by its standard deviation

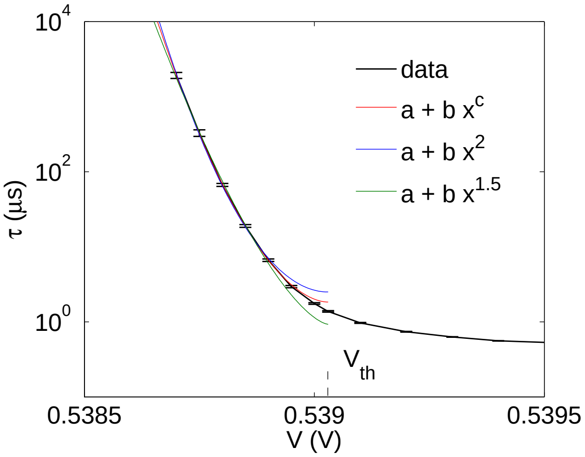

FIGURE 6.8: Mean switching time vs. applied voltage using pulsed scheme. A preliminary fitting for the left five points is performed by setting $y = \log \tau$ and $x = V_{\text{th}} - V$.

s_d^2 and n is the number of trials. So we assume the relationship between τ and other parameters is as follows:

$$\tau_{\text{obs}} = \tau_0 \, e^{\frac{1}{D}(V_{\text{th}}-V)^{\alpha}} + \varepsilon(V), \tag{6.52}$$

where τ_{obs} is the simulated mean first passage time, τ_0, D and α are the parameters to be fitted and $\varepsilon(V) = s^2/n$ is normal noise whose variance depends on the applied voltage V.

6.3.4 Bayesian nonlinear curve fitting

Frequentists use known data to calculate the statistics which estimate the unknown but fixed parameters by minimizing likelihood or some other critieria. The distribution of the statistic over all possible random samples is called sampling distribution which is used to make confidence inference. Bayesian statistics treats the unknown parameters as random variables and their distributions are conditioned on the data. This is based on the Bayes rule:

$$P(A|B) = \frac{P(B|A)P(B)}{P(A)}. \tag{6.53}$$

Now the distribution of the unknown parameter θ can be viewed as knowledge of their uncertainty. Such a knowledge prior to the analysis of the data can be quantified as the prior distribution $\pi_0(\theta)$. The distribution of the random variable x conditioned on parameter θ is called likelihood $p(x|\theta)$. The knowledge of the parameter given data is called posterior distribution $\pi(\theta|x)$. According to Bayes' rule,

$$\pi(\theta|x) = p(\theta|x) = \frac{p(x|\theta)p(\theta)}{\int p(x|\theta)p(\theta)d\theta}. \tag{6.54}$$

This is the probability of the parameters conditioned on the observed data, i.e., the data updates the knowledge of the parameter.

Since the data are calculated for a discrete set of V values, we add subscript i and rewrite Eq. 6.52:

$$\tau_i = \tau_0 \, e^{\frac{1}{D}(V_{\text{th}}-V_i)^\alpha} + \varepsilon_i \tag{6.55}$$

where ε_i is normal noise $N(0, s_i^2/n_i)$. The set of unknown parameters to be determined by fitting is denoted by $\theta = \{\tau_0, D, \alpha\}$. Equation. 6.55 says that τ_i is random variable having normal distribution $N(\tau_0 \; e^{\frac{1}{D}(V_{\text{th}}-V_i)^\alpha}, s_i^2/n_i)$. We adopt a Bayesian approach, treating the parameters $\theta = \{\tau_0, D, \alpha\}$ as random variables. Let $\tau = \{\tau_1, \tau_2, ..., \tau_n\}$ and denote $f(\tau;\theta)$ by the joint distribution of τ and θ, which can be written as

$$f(\tau;\theta) = f(\tau|\theta)\pi_0(\theta) = \pi(\theta|\tau)f(\tau). \tag{6.56}$$

In the above equation, $f(\tau|\theta)$ is the conditional distribution of the data (τ) given θ. When viewed as a function of θ, $f(\tau|\theta)$ is called the likelihood $L((\tau_{obs}, V); \alpha, D, \tau_0)$:

$$L((\tau_{obs}, V); \alpha, D, \tau_0) \equiv f(\tau|\theta) = \prod_{i=1}^{n} N(\tau_i; \tau_0 e^{\frac{1}{D}(V_{\text{th}}-V_i)^\alpha}, s_i^2/n_i) \tag{6.57}$$

$\pi_0(\theta)$ denotes the prior distribution on θ, which can be used to incorporate prior knowledge about the parameters. Here we use a flat noninformative prior distribution:

$$\pi_0(\alpha, D, \tau_0) = \pi_0(\alpha)\pi_0(D)\pi_0(\tau_0) = \begin{cases} 1 & \text{for } \alpha > 0 \text{ and } D > 0 \text{ and } \tau > 0 \\ 0 & \text{for } \alpha < 0 \text{ or } D < 0 \text{ or } \tau < 0 \end{cases} \tag{6.58}$$

Then $\pi(\theta, \tau)$ is called the posterior distribution, meaning the distribution of θ given the observed data τ. So

$$\pi(\theta|\tau) = \frac{f(\tau|\theta)\pi_0(\theta)}{f(\tau)} \propto L((\tau_{obs}, V); \alpha, D, \tau_0, s_i^2/n_i), \tag{6.59}$$

Therefore we can evaluate the posterior distribution $\pi(\alpha, D, \tau_0)$ for any value of the unknown parameters α, D, τ_0 by calculating $L((\tau_{obs}, V); \alpha, D, \tau_0, s_i^2/n_i)$ (Eq. 6.57). Normalization and marginalization are performed by numerical integration.

The posterior distributions are plotted in Fig. 6.9. The exponent α is centered at 1.82 and the 95% Bayesian highest probability density (HPD) for α is $[1.64, 2.02]$. This means that 95% of the chance α is in the interval $[1.64, 2.02]$ and it is highly unlikely that α is 1.5. The probability that $\alpha \leq 1.5$ is 5.1×10^{-4}. This suggests that the sudden switching of the applied voltage at the beginning has significant influence on the switching time.

To eliminate the effect of the sudden change of the applied voltage, we use the metastable state of the deterministic system as initial condition and keep the corresponding voltage as a constant. We refer to this scheme as *metastable* scheme. The switching time is measured right after the starting of the simulation. The data points are shown in Fig. 6.10. Again, the leftmost five data points are fitted. The distribution of α is shown in Fig. 6.11. It can been seen that α is centered at 1.63 with a HPD $[1.49, 1.78]$. The Probability that $\alpha \leq 1.5$ is 0.04. So we can see that it is still unlikely that $\alpha = 1.5$.

Although it is prohibitive to calculate even longer switching times due to exponentially increasing computation time, do more data points with relatively short

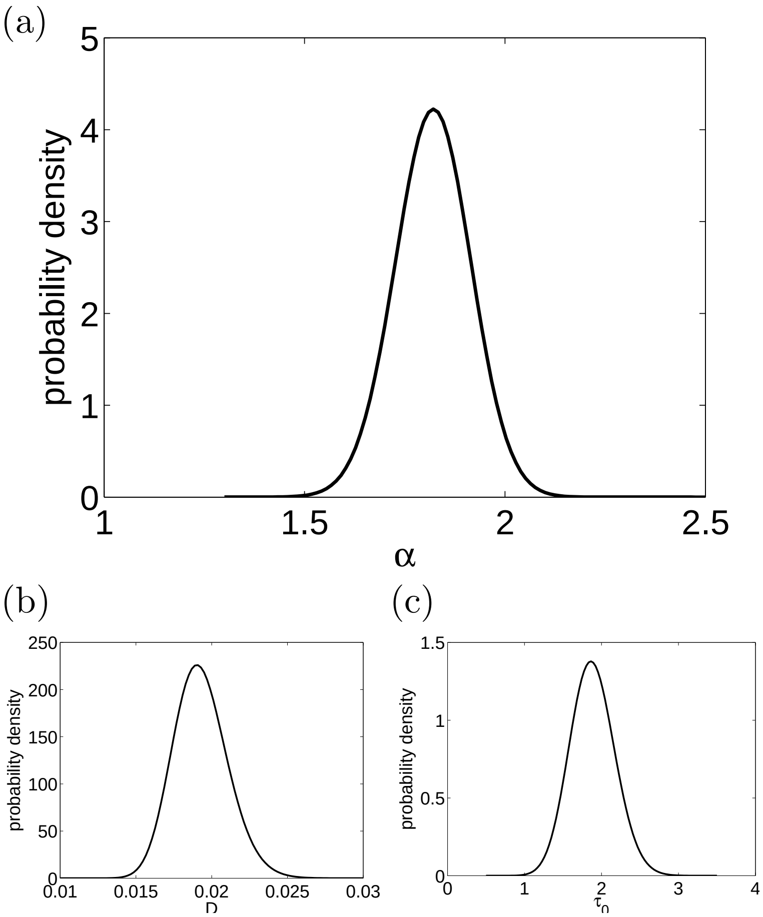

FIGURE 6.9: The posterior distributions for parameters (a) α, (b) D, (c) τ_0 for pulsed scheme by direct integration.

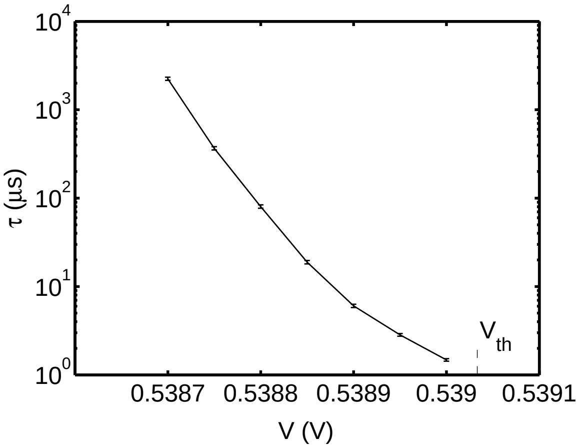

FIGURE 6.10: Mean switching time for metastable scheme.

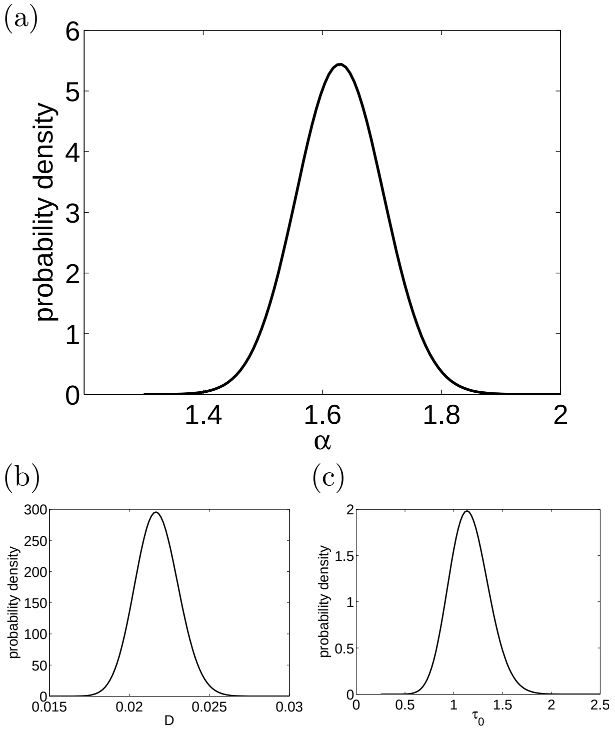

FIGURE 6.11: The posterior distributions for parameters (a) α, (b) D, (c) τ_0 for metastable scheme by direct integration.

mean switching time improve the results? Four more data points are added in the metastable method, shown in Fig. 6.12. The posterior distributions are shown in Fig. 6.13. α is centered at 1.67 with HPD $[1.56, 1.80]$. The probability that $\alpha \leq 1.5$ is 0.0028. This confirms the result that α is unlikely equal to 1.5.

Although four more data points were added, the variance of α remains large. The marginal two dimensional posterior distributions are plotted in Fig. 6.14. It can be seen that the parameters have strong pairwise correlation, which means that the parameters are confounded. This is a property of this statistical model and cannot be improved by adding more data points within the available range of V.

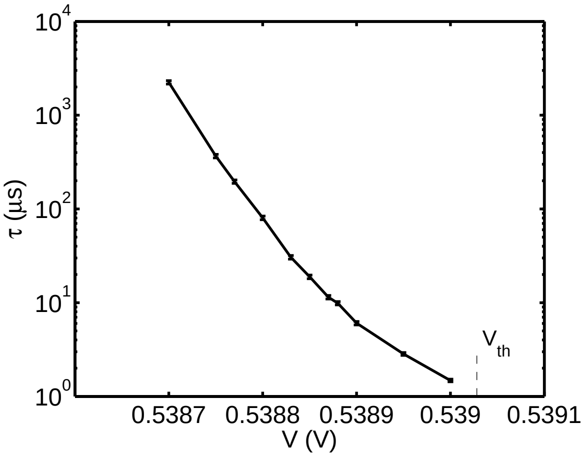

FIGURE 6.12: Mean switching time for metastable scheme with more data points.

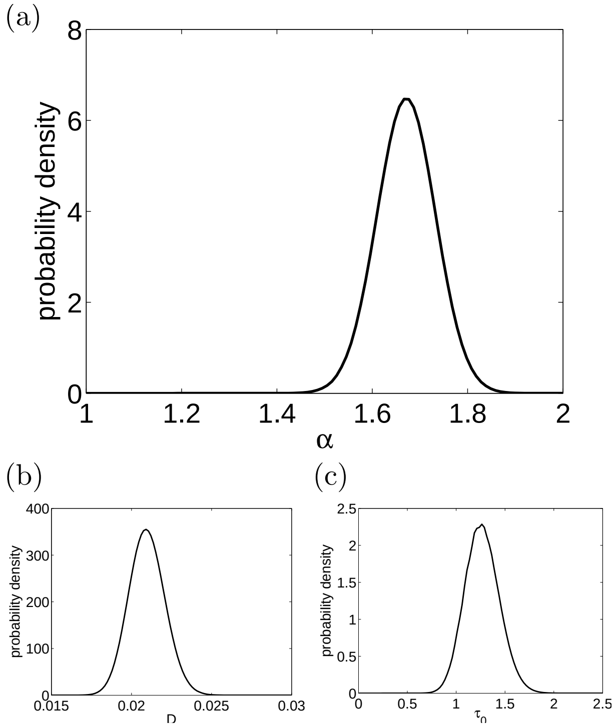

FIGURE 6.13: The posterior distributions for parameters (a) α, (b) D, (c) τ_0 for metastable scheme with nine points by direct integration.

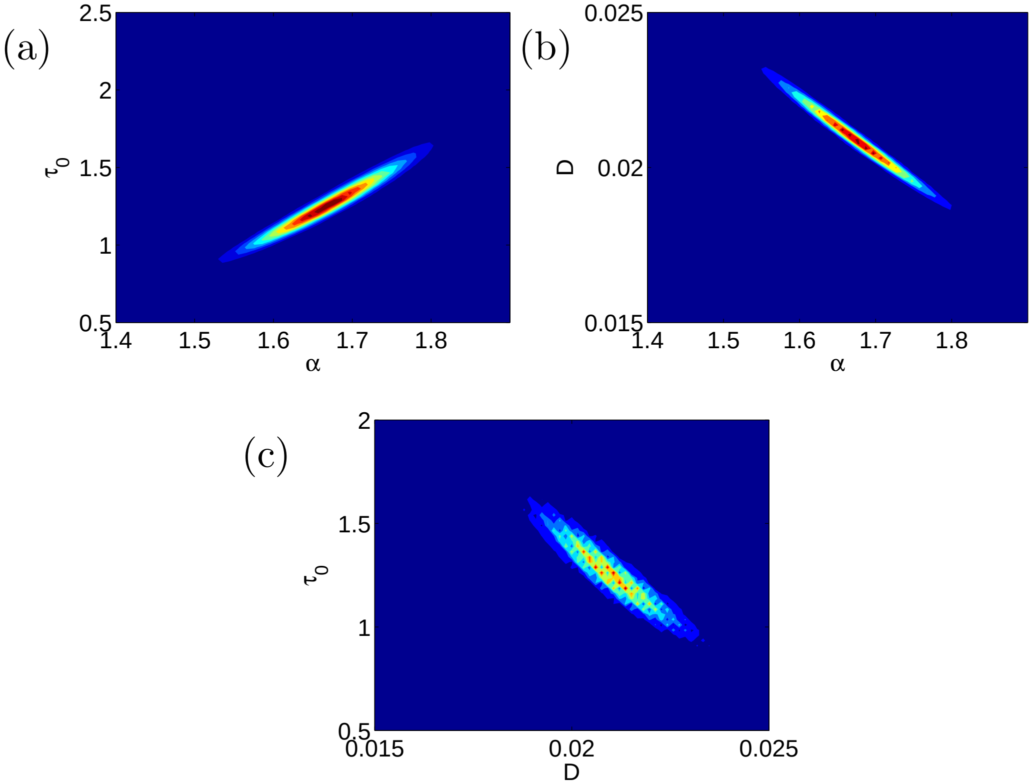

FIGURE 6.14: The marginal posterior distributions for parameters (a) α, (b) D, (c) τ_0 for metastable scheme with nine points by direct integration.

6.4 Projection onto saddle-node trajectory

The scaling behavior clearly demonstrates that the biased voltage affects the switching probability. When the biased voltage decreases from the threshold voltage, the metastable state becomes more and more stable and the switching is less and less likely to occur. In a one-dimensional model, this corresponds to the increase of the potential barrier that separates the two stable fixed points. Superlattices are high dimensional systems. Can we still find some quantity that characterize the switching? Here a local effective potential will be developed.

The deterministic part of field model Eq. 6.46 has the form:

$$d\mathbf{F} = \mathbf{G}(\mathbf{F})dt \tag{6.60}$$

We know that on the current branch there is a stable fixed point $\mathbf{F}^0$ such that $\mathbf{G}(\mathbf{F}^0) = \mathbf{0}$. Then we can find the Jacobian matrix evaluated at $\mathbf{F}^0$, $D\mathbf{G}(\mathbf{F}^0) = \{\partial G_i/\partial F_j\}$. Diagonalizing this matrix gives us the manifolds of the system.

The Jacobian matrix has elements $a_{ij} = \partial G_i/\partial F_j$. Summation along each column equals $\sum_i a_{ij} = \frac{\partial(\sum_i G_i)}{\partial F_j} = \frac{\partial d(\sum_i F_i)/dt}{\partial F_j} = 0$ under the constant total applied voltage. If the eigenvector $\mathbf{v} = (v_1, v_2, ..., v_{41})$ has eigenvalue λ such that $D\mathbf{G} \cdot \mathbf{v} = \lambda \mathbf{v}$. or

$$\begin{pmatrix} a_{11}v_1 + a_{12}v_2 + ... \\ a_{21}v_1 + a_{22}v_2 + ... \\ . \\ . \end{pmatrix} = \lambda \begin{pmatrix} v_1 \\ v_2 \\ . \\ . \end{pmatrix} \tag{6.61}$$

The summation of all the components of the vector on the left hand side equals $\sum_j (\sum_i a_{ij}) v_j = 0$ since $\sum_i a_{ij} = 0$ for each j. This yields the property of the eigenvector that $\lambda \sum_i v_i = 0$, or $\sum_i v_i = 0$ unless $\lambda = 0$.

A typical eigenvalue spectrum is shown in Fig. 6.15a. All the real parts of the eigenvalues are smaller than zero, except $\lambda_0 = 0$. The eigenvalue λ_1 is the one has the largest non-zero real part. The eigenvectors $\mathbf{w}$ of the λ_0 and $\mathbf{v}$ of λ_1 are shown in Fig. 6.15b. The summation of the coefficients are $\sum_i v_i = 0$ and $\sum_i w_i \neq 0$. Since the system can only move in the manifold (hyperplane) $\mathcal{C} = \{\mathbf{F} | \sum_i F_i = U\}$, this means that $\mathbf{w}$ is perpendicular to $\mathcal{C}$ and moving along $\mathbf{w}$ can only be achieved by changing total applied voltage U. The fact that the summation of the components of the other eigenvectors equals to zero means that these eigenvectors are in the manifold $\mathcal{C}$ and moving along any combination of them is allowed. Also notice that the component of E_{36} is very large in both $\mathbf{w}$ and $\mathbf{v}$.

We explore the phase space along $\mathbf{v}$, the corresponding has the largest non-zero real value. The algorithm is described below: move the fields to a new position along $\mathbf{v}$ by a small amount ϵ, i.e., $\mathbf{F}' = \mathbf{F} + \epsilon \mathbf{v}$. Calculate the Jacobian matrix at the new position $D\mathbf{G}(\mathbf{F}')$, diagonalize it and update $\mathbf{v}$ and λ_1. Then move the fields to the

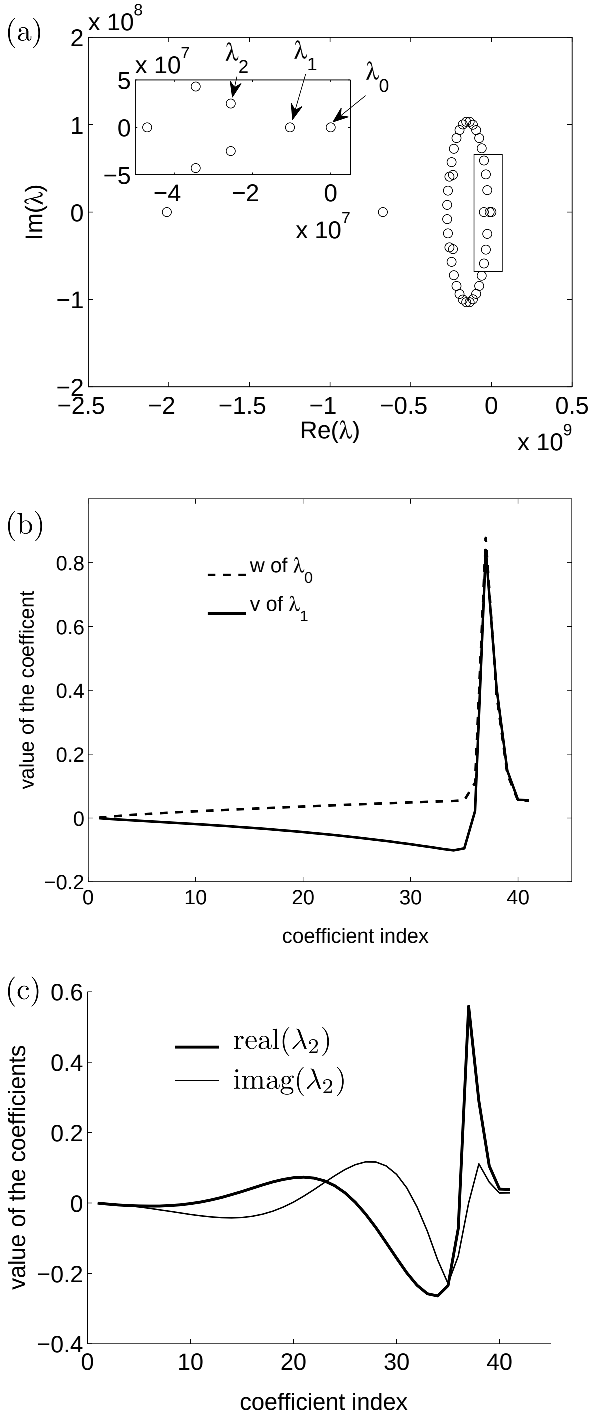

FIGURE 6.15: a) Eigenvalue spectrum of Jacobian matrix $D\mathbf{G}$ at metastable fixed point $\mathbf{F}^0$ and total applied voltage $V = 0.5389$ V. The inset is the blowup of the region enclosed by the rectangle. b) eigenvector of λ_0 and λ_1. c) eigenvector λ_2

next position along the new $\mathbf{v}$ by ϵ and repeat the above steps. As we carry out this algorithm, we use $s > 0$ to denote the distance that we moved. Then λ_1 is a function of s, $\lambda_1 = \lambda_1(s)$. We now create a one-dimensional system for s,

$$\dot{s} = f(s) \tag{6.62}$$

where $f'(s) = \lambda_1(s)$ with $f(0) = 0$. So $f(s) = \int_0^s \lambda(s')ds'$. With $f(s)$ determined, we can find the effective potential (Lyapunov function) $U(s) = -\int_0^s f(s')ds'$. The computed effective potential U for $V = 0.5389$ V is shown in Fig. 6.16a. We can see that the potential first increases and then decreases, forming a barrier with height ΔU and ΔU is a function of applied voltage V. In Fig. 6.16b, we plot mean first passage time $\log(\tau)$ vs. ΔU. The straight line indicates that τ has the form

$$\tau = A\mathrm{e}^{\Delta U/D} \tag{6.63}$$

or,

$$\ln \tau = \ln A + \Delta U/D \tag{6.64}$$

Fitting the straight line, we find $1/D = 4.58 \times 10^{-15}$, or $D = 2.19 \times 10^{14}$ ($\mathrm{V}^2\mathrm{m}^{-2}\mathrm{s}^{-1}$).

The plot of operational points Fig. 6.17 shows some insight into the switching mechanism and the eigenvector $\mathbf{v}$. The curves in Fig. 6.17 are the tunneling current $J_{i\to i+1}$ vs. field F_i with n_i and n_{i+1} of the actual profile of the deterministic fixed point of the system. The dots denotes the operation points, i.e., the tunneling current $J_{i\to i+1}$ with actual values of F_i, n_i and n_{i+1}.

It can be seen that when the applied voltage is far from the end of the current branch, e.g., $V = 0.47$ V in Fig. 6.17b, all the operation points are in the positive differential conductivity regions. However, when V is near the end of the current branch, F_{36} is in the NDC region, shown in the inset of Fig. 6.17a. However, at the end of the current branch, the operation point for the $J_{36\to 37}$ is already in the NDC region which causes instability. This is consistent with the large component of E_{36} in the eigenvector.

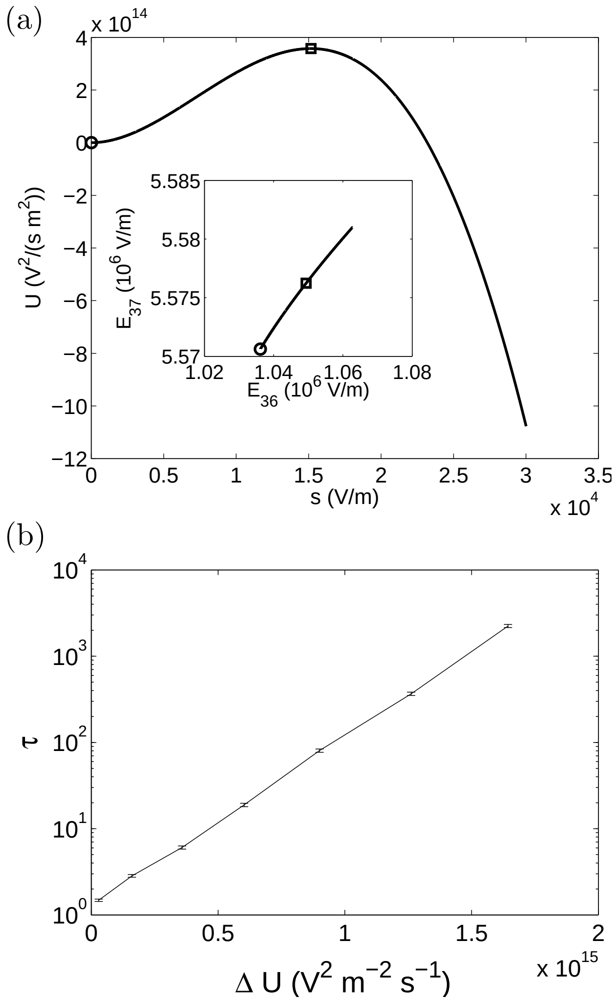

FIGURE 6.16: a) the effective potential U for $V = 0.5389$ V. The inset is the projection of the eigenpath onto subspace E_{36} and E_{37}, with the circle denoting the starting point and the square denoting the saddle point. b) mean first passage time τ vs. potential barrier height ΔU.

6.5 Analysis of the ensemble

For an arbitrary system

$$\frac{d\mathbf{x}}{dt} = f(\mathbf{x}) \tag{6.65}$$

with fixed point $\mathbf{x} = \mathbf{x}_1$. If the particle starts from the fixed point $\mathbf{x}_1$, then the distribution of the particle coordinate over a period of time is a delta function $\delta(\mathbf{x} - \mathbf{x}_1)$. As noise is added to the system, the particle wanders around $\mathbf{x}_1$ and the distribution

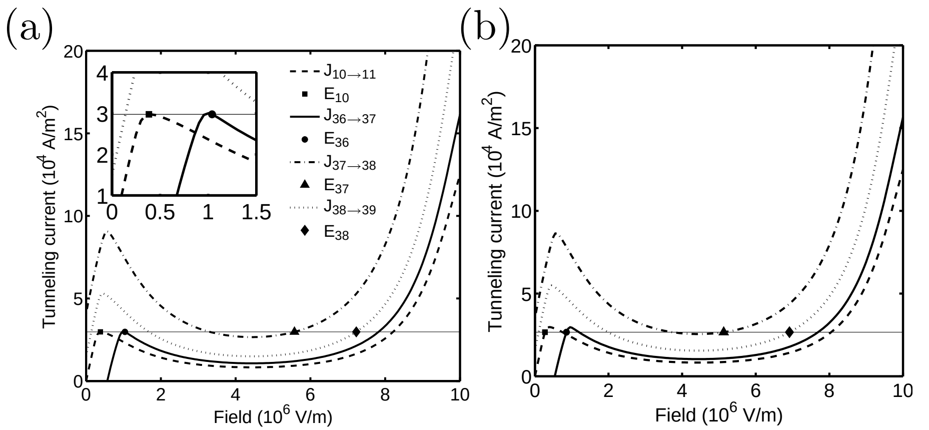

FIGURE 6.17: Operation points at $V = 0.539$V (left) and 0.47V (right)

is no longer a delta function. If the particle overcomes the attraction of $\mathbf{x}_1$ and moves to another fixed point $\mathbf{x}_2$, a trajectory connecting $\mathbf{x}_1$ and $\mathbf{x}_2$ forms in the phase space. Since there is randomness in the whole process, each switching process traces out a different trajectory. An ensemble of trajectories of many trials can be recorded.

For the switching process in superlattices, the dynamical variable $F_i(t)$ is 41 dimensional for $N = 40$. Figure 6.18 is the histogram in the subspace of F_{36} and F_{37}. In Fig. 6.18b, the histogram is plotted as a contour plot. The white curve is the eigenvector path obtained in Sec. 6.4. The circle and the square mark the stable fixed point and saddle point respectively.

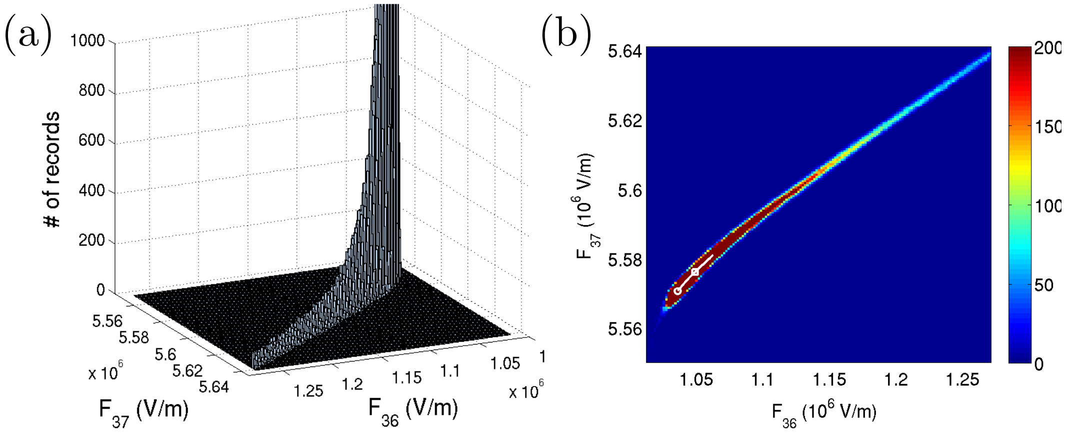

FIGURE 6.18: a) Histogram of F_{36}, F_{37} b) Contour plot of the histogram of F_{36}, F_{37}

The trajectories fluctuate around a path called most probable path along which the particle is most often observed. From the histogram, we can find the most probable path by locating the maximum of the histogram along the swamp of the trajectories. This is shown in Fig. 6.19 as the blue curve. Chan *et. al.* showed that the distribution of trajectories is a normal distribution centered at the most probable path.

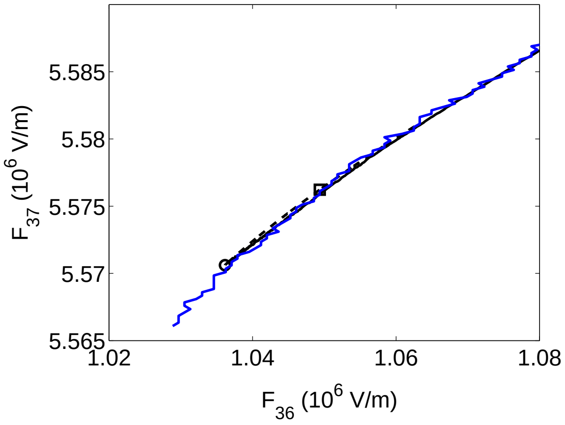

FIGURE 6.19: Solid line is the ensemble mean. Dashed line is the eigenvector path. Blue line is the most probable path.

In Fig. 6.19, an ensemble mean path is also plotted as the solid line. This is obtained by first aligning the trajectories in time when the switching occurs, shown in Fig. 6.20. Then calculate the mean value of F_i over the ensemble at each time step. The most probable path, the ensemble mean and the eigenvector path (the dash line) almost overlap in Fig. 6.19.

6.5.1 Multivariate statistics

Usually, the statistical tools are applied to a scalar response. The data in t-test, ANOVA and the response in linear regression are all one dimensional. In practice, multivariate data are very common. Simultaneous variables are measured on a single sampling unit, forming a high dimensional data set. So each observation can be

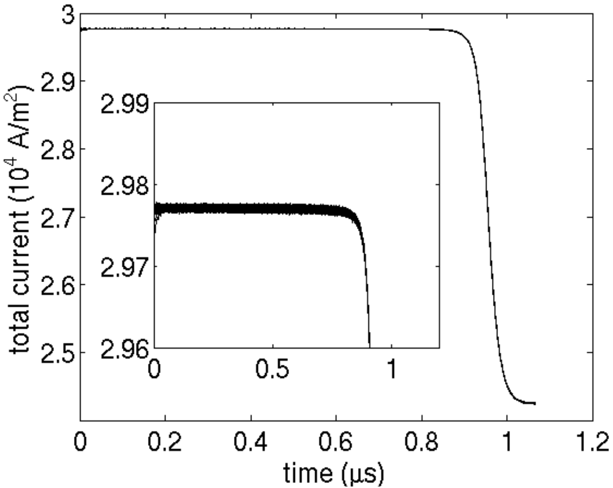

FIGURE 6.20: Alignment of the switching processes.

represented by a p dimensional vector $\mathbf{y}$. If there are n observations in a sample, then the data can be denoted by $\mathbf{y}_1, \mathbf{y}_2, ...\mathbf{y}_n$, where

$$\mathbf{y}_i = \begin{pmatrix} y_{i1} \\ y_{i2} \\ . \\ . \\ y_{ip} \end{pmatrix}. \tag{6.66}$$

The data matrix $\mathbf{Y}$ is a spread sheet with each row as a sampling unit and each column as a dimension, i.e.,

$$\mathbf{Y} = \begin{pmatrix} \mathbf{y}_1^T \\ \mathbf{y}_2^T \\ . \\ . \\ \mathbf{y}_n^T \end{pmatrix}. \tag{6.67}$$

Some statistics of univairate data can be extended to multivariate case. The sample mean $\bar{\mathbf{y}}$ is the vector of sample mean of each dimension, i.e.,

$$\bar{\mathbf{y}} = \frac{1}{n}\sum_{i=1}^{n} \mathbf{y}_i = \begin{pmatrix} \bar{y}_1 \\ \bar{y}_2 \\ . \\ . \\ \bar{y}_p \end{pmatrix}, \tag{6.68}$$

where $\bar{y}_j = \sum_{i=1}^{n} y_{ij}/n$. Similarly, the population mean can be defined as the expectation value of the sample mean:

$$\mu = E(\mathbf{y}) = E(\bar{\mathbf{y}}) = \begin{pmatrix} E(y_1) \\ E(y_2) \\ . \\ . \\ E(y_p) \end{pmatrix} = \begin{pmatrix} \mu_1 \\ \mu_2 \\ . \\ . \\ \mu_p \end{pmatrix}. \tag{6.69}$$

In univariate statistics, all kinds of variance play a critical role in many inference tools. The counterpart of variance in multivariate statistics is the covariance matrix. The sample covariance matrix $\mathbf{S} = (s_{jk})$ is a p by p matrix defined as

$$\mathbf{S} = (s_{jk}) = \begin{pmatrix} s_{11} & s_{12} & . & . & s_{1p} \\ s_{21} & s_{22} & . & . & s_{2p} \\ . & . & . & . & . \\ . & . & . & . & . \\ s_{p1} & s_{p2} & . & . & s_{pp} \end{pmatrix}, \tag{6.70}$$

where the diagonal elements s_{jj} are the sample variance of each dimension, i.e., $s_{jj} = s_j^2 = \sum_{i=1}^{n}(y_{ij} - \bar{y}_j)^2/(n-1)$ and s_{jk} is the covariance between jth and kth variables, i.e., $s_{jk} = \sum_{i=1}^{n}(y_{ij} - \bar{y}_j)(y_{ik} - \bar{y}_k)/(n-1)$. The sample covariance matrix can also be written in vector $\mathbf{y}$ as

$$\mathbf{S} = \frac{1}{n-1}\sum_{i=1}^{n}(\mathbf{y}_i - \bar{\mathbf{y}})(\mathbf{y}_i - \bar{\mathbf{y}})^T \tag{6.71}$$

$$= \frac{1}{n-1}\left(\sum_{i=1}^{n}\mathbf{y}_i\mathbf{y}_i^T - n\bar{\mathbf{y}}\bar{\mathbf{y}}^T\right). \tag{6.72}$$

Similarly, the population covariance matrix is also a p by p matrix

$$\mathbf{\Sigma} = (\sigma_{jk}) = \begin{pmatrix} \sigma_{11} & \sigma_{12} & . & . & \sigma_{1p} \\ \sigma_{21} & \sigma_{22} & . & . & \sigma_{2p} \\ . & . & . & . & . \\ . & . & . & . & . \\ \sigma_{p1} & \sigma_{p2} & . & . & \sigma_{pp} \end{pmatrix}, \tag{6.73}$$

where $\sigma_{jk} = E(s_{jk})$ and be written as

$$\mathbf{\Sigma} = \mathrm{cov}(\mathbf{y}) = E[(\mathbf{y} - \mu)(\mathbf{y} - \mu)^T] = E(\mathbf{y}\mathbf{y}^T) - \mu\mu, \tag{6.74}$$

or

$$E(\mathbf{S}) = \mathbf{\Sigma}. \tag{6.75}$$

We can also define the sample correlation matrix as

$$\mathbf{R} = (r_{jk}) = \begin{pmatrix} 1 & r_{12} & . & . & r_{1p} \\ r_{21} & 1 & . & . & r_{2p} \\ . & . & . & . & . \\ . & . & . & . & . \\ r_{p1} & r_{p2} & . & . & 1 \end{pmatrix}, \tag{6.76}$$

where

$$r_{jk} = \frac{s_{jk}}{\sqrt{s_{jj}s_{kk}}} = \frac{s_{jk}}{s_j s_k}. \tag{6.77}$$

The univariate variance characterizes the dispersion of data in one dimension. Likewise, one meaning of the covariance matrix is the dispersion of data in high dimensional space. For a high dimensional ellipsoid, called *hyperellipsoid*, $(\mathbf{y} - \bar{\mathbf{y}})^T\mathbf{S}^{-1}(\mathbf{y} - \bar{\mathbf{y}}) = a^2$ that just contains all data $\mathbf{y}_i$, the volume is proportional to $|\mathbf{S}|^{-1/2}$. The determinent $|\mathbf{S}| = \lambda_1\lambda_2 \cdots \lambda_p$ is called generalized sample variance, where λ_i are eigenvalues of $\mathbf{S}$. If some eigenvalues are zero or near zero, then the variables are linearly dependent and there is redundancy in the data, thus some dimensions can be removed. Another way to characterize the total variance is the trace $\mathrm{tr}(\mathbf{S})$.

The covariance matrix is extremely useful in multivariate statistics. For example, when we test if the mean vector $\mu = \mu_0$, the statistical distance $d^2 = (\bar{\mathbf{y}} - \mu)^T \left(\frac{\mathbf{S}}{n}\right)^{-1} (\bar{\mathbf{y}} - \mu)$ is useful rather than the Euclidean distance $(\bar{\mathbf{y}} - \mu)^T(\bar{\mathbf{y}} - \mu)$. This is T^2 test: $T^2 = d^2$. In multivariate analysis of variance (MANOVA), covariance matrices within groups and between groups are calculated and compared similar to univariate analysis of variance (ANOVA).

In univariate statistics, if the data is multiplied by a scalar, i.e., $z = ay$, then $\mathrm{var}(z) = \mathrm{var}(ay) = a^2\mathrm{var}(y) = a^2\sigma^2$. The sample variance of z is then $s_z^2 = a^2s^2$. In multivariate statistics, the inner product of $\mathbf{y}$ and a constant vector $\mathbf{a}$: $z = \mathbf{a}^T\mathbf{y}$ has sample variance $s_z^2 = \mathbf{a}^T\mathbf{S}\mathbf{a}$. The sample covariance between z and another inner product $w = \mathbf{b}^T\mathbf{y}$ is $s_{zw}^2 = \mathbf{a}^T\mathbf{S}\mathbf{b}$. So if there are k such inner products forming a new multivariate data set:

$$\mathbf{z} = \begin{pmatrix} \mathbf{a}_1^T\mathbf{y} \\ \mathbf{a}_2^T\mathbf{y} \\ . \\ . \\ \mathbf{a}_k^T\mathbf{y} \end{pmatrix} = \mathbf{A}^T\mathbf{y}, \tag{6.78}$$

the covariance matrix of $\mathbf{z}$ is

$$\mathbf{S}_z = A^T\mathbf{S}A. \tag{6.79}$$

6.5.2 Introduction to PCA

After the previous discussion of the covariance matrix, it is easy to understand principal component analysis[106]. The hyperellipsoid $(\mathbf{y} - \bar{\mathbf{y}})^T\mathbf{S}^{-1}(\mathbf{y} - \bar{\mathbf{y}}) = a^2$ has principal axes which are the eigenvectors $\mathbf{a}_i$ of the matrix $\mathbf{S}$ and can be obtained by diagonalizing $\mathbf{S}$. So $\mathbf{S}\mathbf{a}_i = \lambda_i\mathbf{a}_i$. It can also be written as $\mathbf{SA} = \mathbf{AD}$, where $\mathbf{A} = (\mathbf{a}_1, \mathbf{a}_2, ..., \mathbf{a}_p)$ and diagonal matrix $\mathbf{D} = \mathrm{diag}(\lambda_1, ..., \lambda_p)$. Since $\mathbf{A}$ is an orthogonal matrix, $\mathbf{A}^{-1} = \mathbf{A}^T$. Any centered data point $\mathbf{y}$ having distance d^2: $\mathbf{y}^T\mathbf{S}^{-1}\mathbf{y} = d^2$ can be written as $d^2 = \mathbf{y}^T\mathbf{A}\mathbf{A}^{-1}\mathbf{S}^{-1}\mathbf{A}\mathbf{A}^{-1}\mathbf{y} = \mathbf{z}^T\mathbf{D}^{-1}\mathbf{z}$ where $\mathbf{y}$ has been transformed to $\mathbf{z}$ by $\mathbf{z} = \mathbf{A}^T\mathbf{y}$. According to Eq. 6.79, the diagonal matrix $\mathbf{D} = A^T\mathbf{S}A$ is the covariance matrix of the new variables $\mathbf{z}$.

This means that when the data is transformed to a new coordinate system whose basis is the eigenvectors $\mathbf{a}_i$ of the covariance matrix $\mathbf{S}$, the variance of the data along direction $\mathbf{a}_i$ is $s_{z_i}^2 = \lambda_i$. The components $z_1, z_2, ..., z_p$ of the transformed variable $\mathbf{z}$ are called principal components, or simply pc. Their values of individual observations are called z-scores. The first pc z_1 with the largest eigenvalue λ_1 corresponds to the longest axis of the ellipsoid which accounts for the biggest portion of the variance of the data. The pc's with rank ordered eigenvalues accounts for decreasing portion of the variance of the data. Some pc's can be neglected if their eigenvalues are very small, leading to reduction of dimension. This means that the actual dimension of the system is smaller than p.

6.5.3 Results

From the histogram in Fig. 6.18, we can imagine that the trajectories form a narrow tube around the most probable path in phase space when switching. If we pick a narrow time window within which the trajectories do not have much curvature, then the trajectories almost form a cylinder. If the dispersion of the trajectories is smaller than the length of the trajectories, then the variation of the dynamical variables occurs mostly along the height of the cylinder. Principal component analysis should be able to capture this.

To test this idea, we first align the switching processes as in Fig. 6.20. In Fig. 6.21, two narrow time windows t_1 and t_2 are chosen. The numerically generated discrete data of the trajectories within these two time windows will be studied by PCA. For t_2 in Fig. 6.21, there is a clear trajectory in phase space. The first principal component (pc) at t_1 and t_2 are shown in Fig. 6.22. We can see that the first pc of t_2 is close to the eigenvector $\mathbf{v}$ of λ_1, which means that the movement of the system in phase space does not change its direction very much. This is why the histogram in Fig. 6.18 looks like a straight line. The histogram of projection of the trajectory onto the first and second pc at t_2, i.e., the z-score z_1 and z_2 at t_2 is plotted in Fig. 6.24. The distribution of z_1 is almost uniform and that of z_2 is almost normal. This means that the trajectories does move along the direction of the first pc and the form a narrow tube. The z-score z_1 at t_1 is normal. This means that there is no definitive trajectory in phase space and the PCA method fails to capture a major direction.

Since the eigenvectors and eigenvalues are calculated from an ensemble, that is, a sample, to check if they are a good estimate of the eigenvectors and eigenvalues from the populations of switching processes, we also calculate the eigenvectors and eigenvalues from a subset of the ensemble. This is plotted in Fig. 6.23. We can see that the results converge as the number of trials increases.

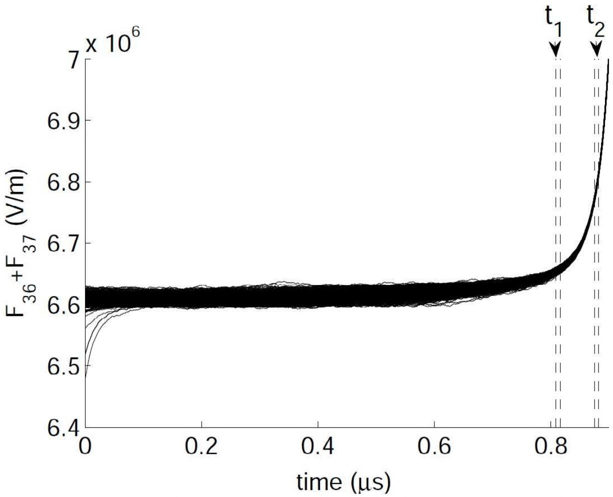

FIGURE 6.21: The two time windows to apply PCA.

The eigenvalues are plotted in Fig. 6.26 which are called scree graphs. The scree plots in Fig. 6.26b shows that the largest eigenvalue corresponding to the first pc at t_2 is a dominant component of the variance while the largest eigenvalue at t_1 is much less dominant. The component of $\lambda_1/\sum\lambda_i = 16.8\%$ for t_1 and 84.5% for t_2. However, in Fig. 6.22, we can see that the first pc at t_1 also has a high peak at E_{37}. This captures the fact that E_{36} has a large variance, shown in Fig. 6.27.

To take into account of different values of variance of E_i, principal component analysis can be applied to the correlation matrix rather than the covariance matrix. The eigenvalues of the correlation matrix are plotted in Fig. 6.26c, d. We can see that

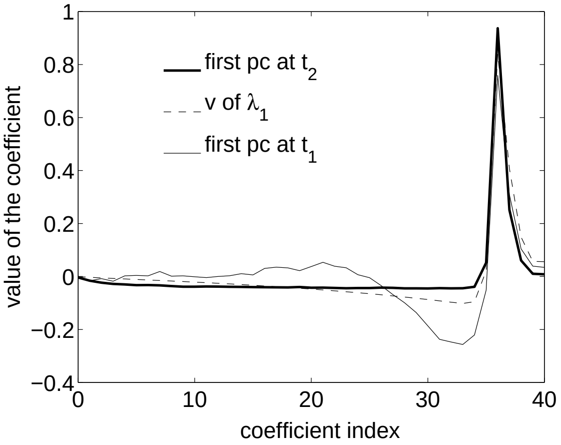

FIGURE 6.22: The first principal components at t_1 and t_2

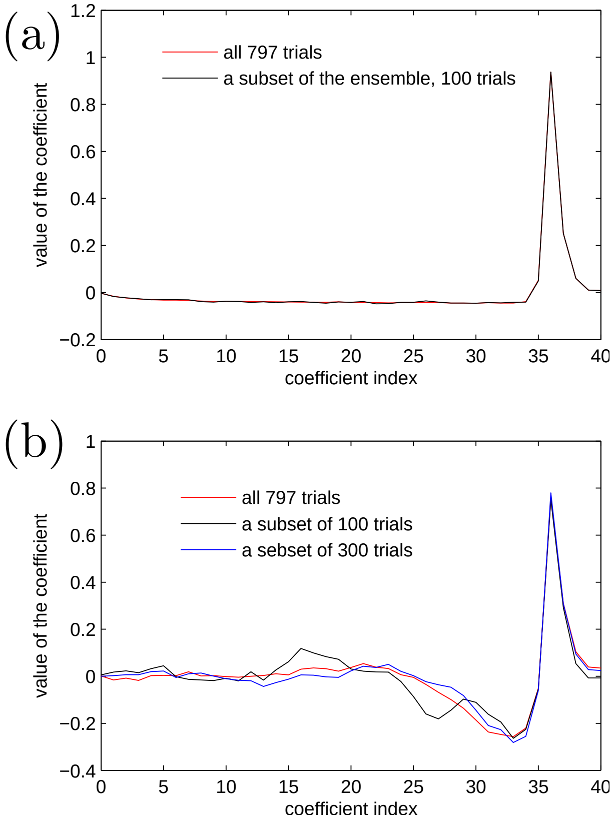

FIGURE 6.23: The first principal components for sub-ensembles at a) t_2 and b) t_1.

the first pc still dominates at t_2. we can see the first pc of the correlation matrix in Fig. 6.28 and the first pc of the covariance matrix in Fig. 6.22 have the same structure. For example, the first pc of the correlation matrix also peaks at E_{36} at t_2,

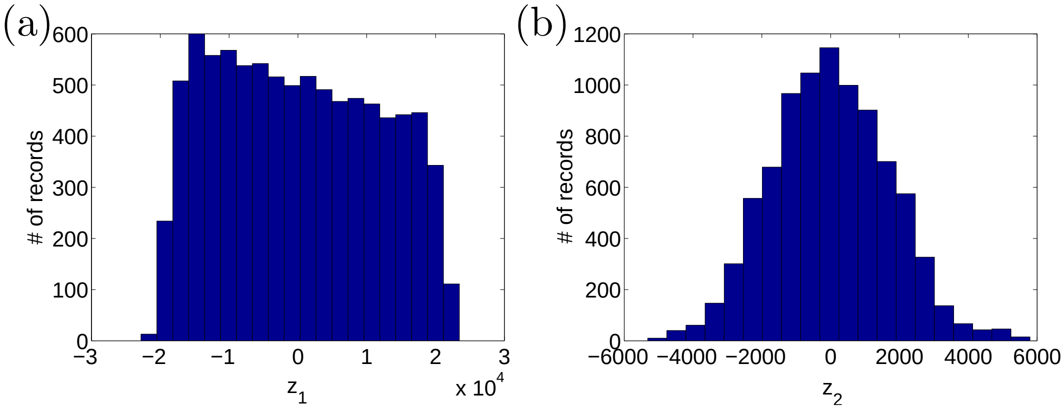

FIGURE 6.24: Histogram of z-scores on the a) first and b) second principal component at t_2.

but the component of E_{36} is much lower than that in the covariance matrix. This is due to the fact that pca on correlation matrix is on the scaled the data $(y_i - \bar{y}_i)/s_i$. The big variance of E_{36} has been divided off, so the big peak of E_{36} in the first pc is brought down significantly in the correlation matrix case. Since the data have been scaled to their variance, the spatial structure has been changed, so the first pc in this case is not the applicable in the Euclidean space.

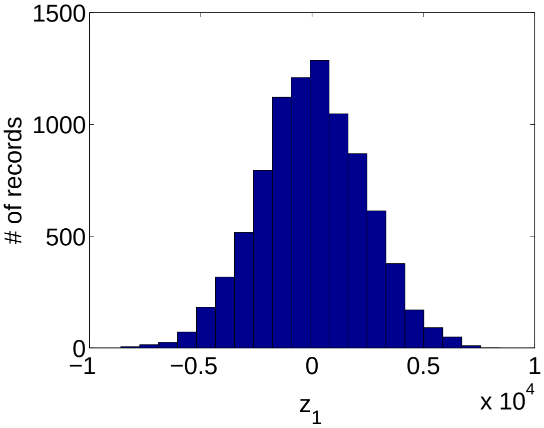

FIGURE 6.25: Histogram of z-scores on the first at t_1.

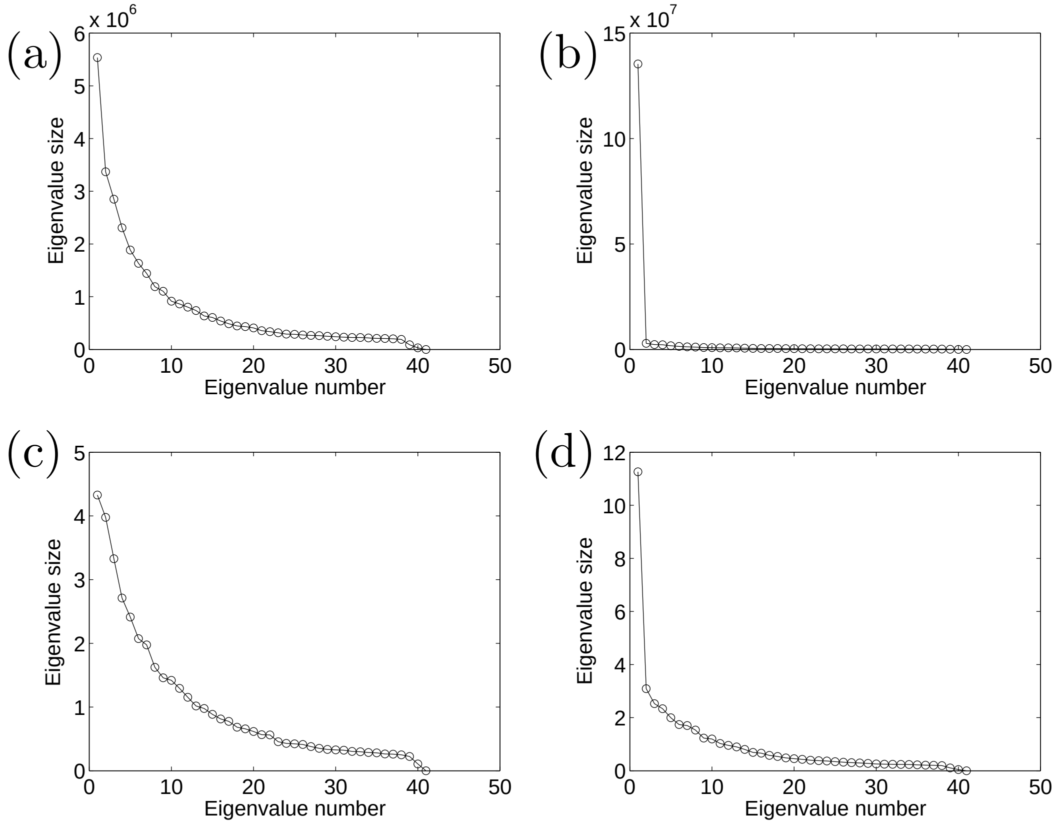

FIGURE 6.26: Eigenvalues of PCA on covariance matrix for a) t_1 and b) t_2. Eigenvalues of PCA on correlation matrix for a) t_1 and b) t_2.

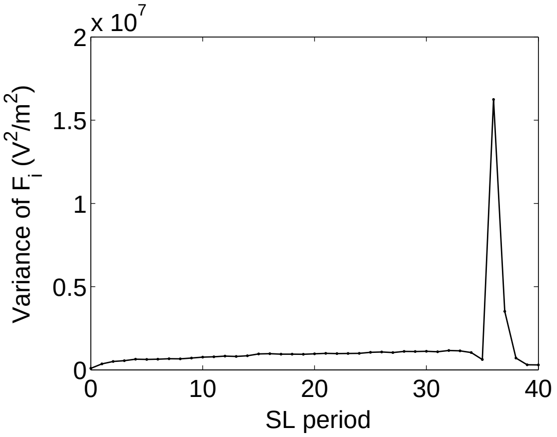

FIGURE 6.27: Variance of F_i

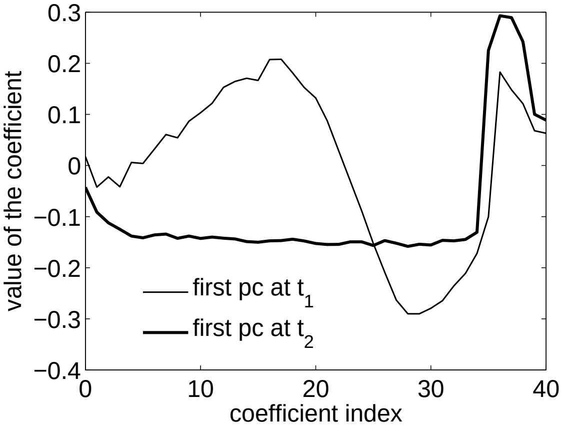

FIGURE 6.28: pc of correlation matrix

7

The tunnel diode model

Up until now, we have been studying superlattices. The nonlinear property NDC in superlattices is the fundamental reason for the rich dynamics in previous chapters. In this chapter, we study a different system which also possesses NDC, a circuit of tunnel diodes connected series. We will compare this system with the superlattice and study the similarity and difference between the two systems. This is motivated in part by asking the question: what are the minimal ingredients necessary for a spatially periodic electronic system to exhibit stable current branches and bistability in current-voltage curves?

7.1 The tunnel diode circuit

The tunnel diode or Esaki diode was invented by Leo Esaki in 1957 and earned him Nobel prize for the electron tunneling effect in these devices [18]. A tunnel diode is a p-n junction between two degenerately doped semiconductors. In degenerately doped n-type semiconductors, the electron density is so high such that the Fermi level lies within the conduction band. Similarly, for p-type semiconductors, the Fermi level lies within the valence band. Such a p-n junction is illustrated in Fig. 7.1. A distinct feature of this structure is overlapping of the valence band on the p side and the conduction band on the n side. It is this feature that causes the unique tunneling behavior of the tunnel diode. When a small forward bias V is applied, E_{F_n} raises by qV with respective to E_{F_p} and the electrons under E_{F_n} on the n side can tunnel through the band gap, occupying the empty states in the valence band on the p side. This is illustrated in Fig. 7.1(a). As the bias increases, more electrons participate in the tunneling process. The current increases as well until the bias increases to a point where the electrons in conduction band on n side starts to pass by the valence band on p side and direct tunneling process drop significantly. So the current decreases as the bias increases, which is the now-familiar phenomenon of negative differential conductance (NDC). This is illustrated in Fig. 7.1(c). As the bias further increases beyond the NDC region, the diffusion current starts to dominate the forward current as a normal p-n junction and the current increases again.

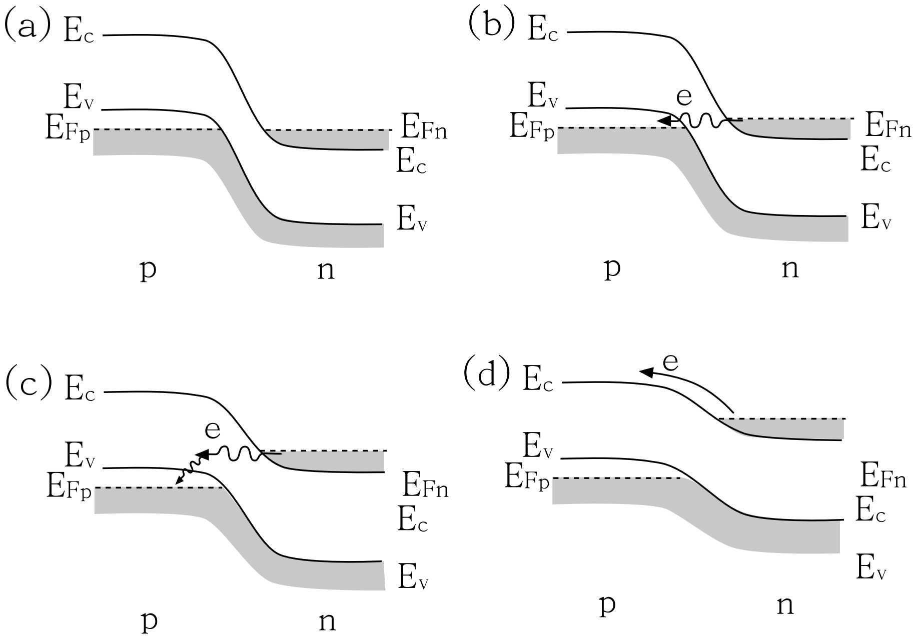

FIGURE 7.1: Band diagram for tunnel diodes under (a) zero bias, (b) small forward bias, (c) increased forward bias in NDC region, (d) high forward bias.

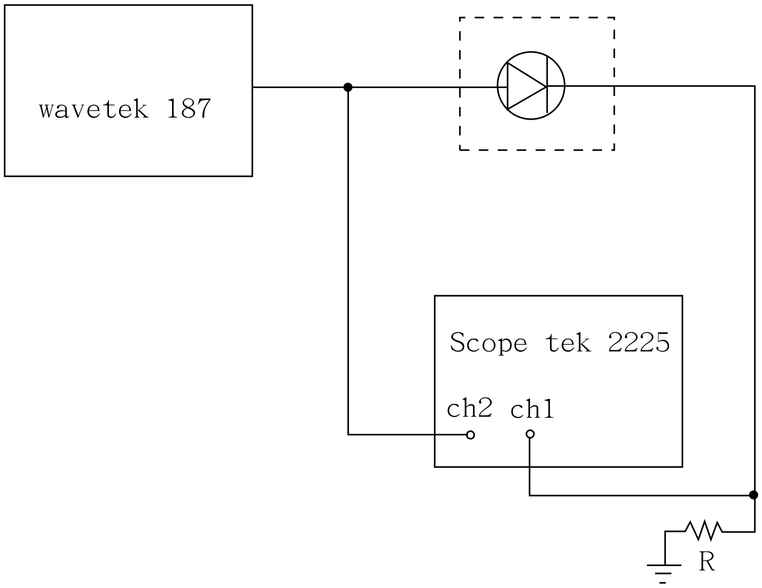

FIGURE 7.2: Schematic of circuit measuring $I-V$ curve of tunnel diode. $R = 52.6$ Ω.

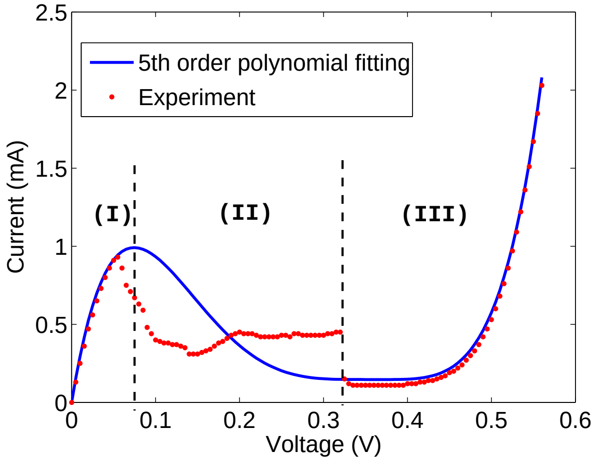

FIGURE 7.3: The $I-V$ curve of tunnel diode (model 1N3712) is measured and then fit by a 5th order polynomial.

We have measured the current versus voltage for a single diode using the circuit shown in Fig. 7.2. The measured $I-V$ curve is shown in Fig. 7.3. Notice that this measured $I-V$ curve is not the intrinsic tunneling current versus applied voltage across the p-n junction. A real tunnel diode has parasitic capacitance and inductance due to packaging, which can cause Hopf bifurcation, i.e., oscillation, and hysteresis in the NDC region [19] for DC bias. It is difficult to measure the true intrinsic IV curve due to the onset of temporal instabilities [94]. However, the increasing part of the current, i.e., region I and III in Fig. 7.3 is still close to the intrinsic IV curve of the tunnel diode. In the simulation below, we use a fifth order polynomial to describe the intrinsic IV curve, which is qualitatively the same, shown in Fig. 7.3.

We also built and measured a circuit composed of tunnel diodes connected series shown in Fig. 7.4. Again, we measure the total current versus applied voltage using the same approach as the single diode case in Fig. 7.2. Figure 7.5 shows the measured IV curve for eight diodes connected in series with no external parallel capacitors. Surprisingly, the total IV curve is not the same as a single diode IV curve. Instead, current branches similar to those of superlattices are clearly seen and hysteresis is also present in this system. In rest of the chapter, we will build a simplified model to studied this system.

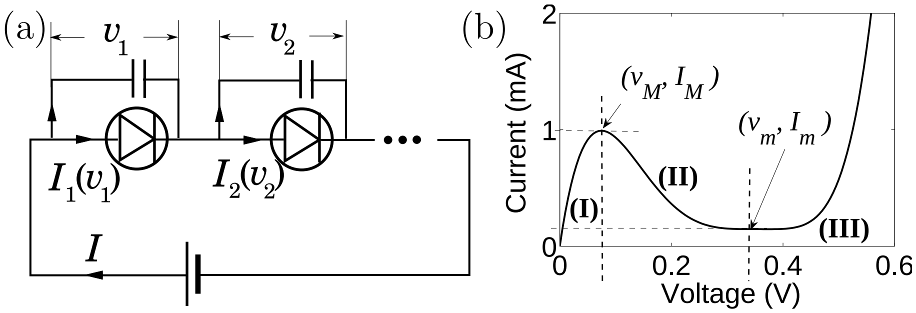

FIGURE 7.4: (a) Nonlinear element array model. Negative differential resistance elements are connected in series with parallel capacitance associated to each element. (b) The $I-V$ curve for a typical element. Region (II) is the NDR region.

7.2 The tunnel diode model

Why are current branches observed in this system? We address this question by introducing a nonlinear circuit model consisting of a voltage-biased series arrays

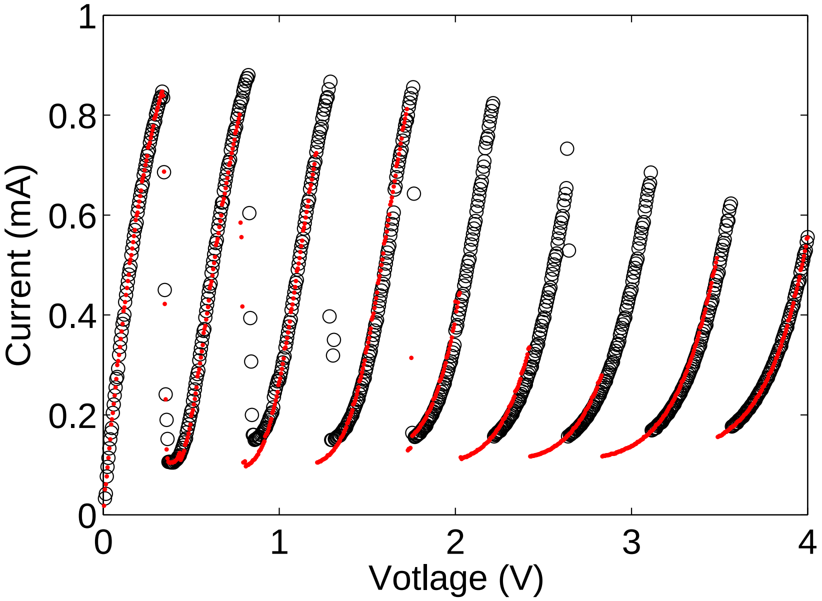

FIGURE 7.5: Measured $I-V$ curve of eight tunnel diode (model 1N3712) connected in series. (Black circuit points: upsweep of voltage. Red dot points: downsweep of voltage.)

of N ideal negative differential resistance elements, each connected in parallel to a capacitance as shown in Fig. 7.4a. We find that heterogeneity in the element properties leads to a form of *coherence in the physical currents that flow through individual elements*, and manifested by the presence of multiple branches in current-voltage curves and a non-uniform distribution of voltages across individual elements. This model provides a simple example of a system in which organized patterns are induced by noise - a type of behavior reported for more complex systems, e.g., chaotic oscillators and reaction-diffusion models,[107] as well as arrays of chaotic oscillators [108].

Each element is assumed to have an intrinsic $I-V$ curve of the form $I_i(v_i)$ with a typical example shown in Fig. 7.4b. The total electrical current is

$$I = I_i(v_i) + C_i\dot{v}_i, \tag{7.1}$$

for $i = 1, 2, ...N$, where v_i denotes the voltage across the i-th element and C_i is the parallel capacitance associated with the i-th element. The total applied voltage to the array is $V = \sum_{j=1}^{N} v_j$. Dividing both sides of Eq. (7.1) by C_i and summing over i allows to express the total current as

$$I = C_{tot}\dot{V} + C_{tot}\sum_{i=1}^{N} I_i/C_i, \tag{7.2}$$

where $C_{tot}^{-1} \equiv \sum_{i=1}^{N} C_i^{-1}$ denotes the total equivalent series capacitance. Relabeling the summation in Eq. (7.2) as over j and substituting the result back into Eq. (7.1), the circuit model equations can be written in the following form:

$$\dot{v_i} = \frac{C_{tot}}{C_i}\dot{V} + \sum_{j=1}^{N} K_{ij}(I_j(v_j) - I_i(v_i)), \tag{7.3}$$

where $K_{ij} = \frac{C_{tot}}{C_i C_j}$. Equation (7.3) has the form of an N-dimensional dynamical system subject to a constraint on the total voltage. The constraint is built into the structure of the model, as seen by summing Eq. (7.3) over all i and using the symmetry property $K_{ij} = K_{ji}$.

In this paper, we focus on the case of *linear ramping* (with ramp time T) in the total applied voltage V, so that V increases linearly between values 0 and NV_{max} and $\dot{V} = N\frac{V_{max}}{T} \equiv N\alpha$. The first term in Eq. (7.3) describes the effect of changing total applied voltage, while the second term describes a global coupling between individual circuit elements. The coupling term displays either positive or negative feedback depending on the state of each element. It is interesting to compare our model with the generalized Kuramoto model[109] as:

$$\dot{\theta}_i = \omega_i + \sum_{j=1}^{N} K_{ij}\sin(\theta_j - \theta_i). \tag{7.4}$$

This model arises in studies of synchronization in systems of many nonlinearly coupled oscillators. They all have a set of intrinsic frequencies and a sum of all coupling terms in the form of $K_{ij}f(x_i - x_j)$. The fundamental difference lies in the coupling function f which describes how elements are coupled to each other. In the Kuramoto model, elements are always attracted to each other and tend to have same phase. When $\theta_i < \theta_j$, the sine function is positive and this causes θ_i to catch up with θ_j. When $\theta_j < \theta_i$, the sin function is negative which causes θ_i to slow down to θ_j. However, this attraction is not always true for the tunnel diode model. The function $J(v)$ has three branches, with the second branch as the NDC region. If v_i and v_j are both on the first or the third branch then it's easy to see that $J_i(v_i) - J_j(v_j)$ has the same effect as the sin function, that is v_i and v_m attract each other. If they are both on the second branch, then they repel each other, see Figs. 7.6. This is the same effect as if the coupling constant K in the Kuramoto model is negative.

What happens when some diodes are on the first branch and some are on the unstable second branch? The first possible situation is captured in Fig. 7.6 where $J_i(v_i) > J_j(v_j)$. Both will move in the direction toward lower current. The i-th diode is "chasing" the j-th one. The slope of the IV curve determines how fast they move. But eventually, the i-th will catch up with j-th because the slope of the second branch tends to zero. If the i-th has caught up with j-th and they have the same current, any noise will tear them slightly apart, then another case in Fig. 7.6 might happen. Both will move upward to bigger current. This process ends up with same current soon if both are not near the peak because the first branch is steeper than the second, thus the j-th catches up with the i-th quickly.

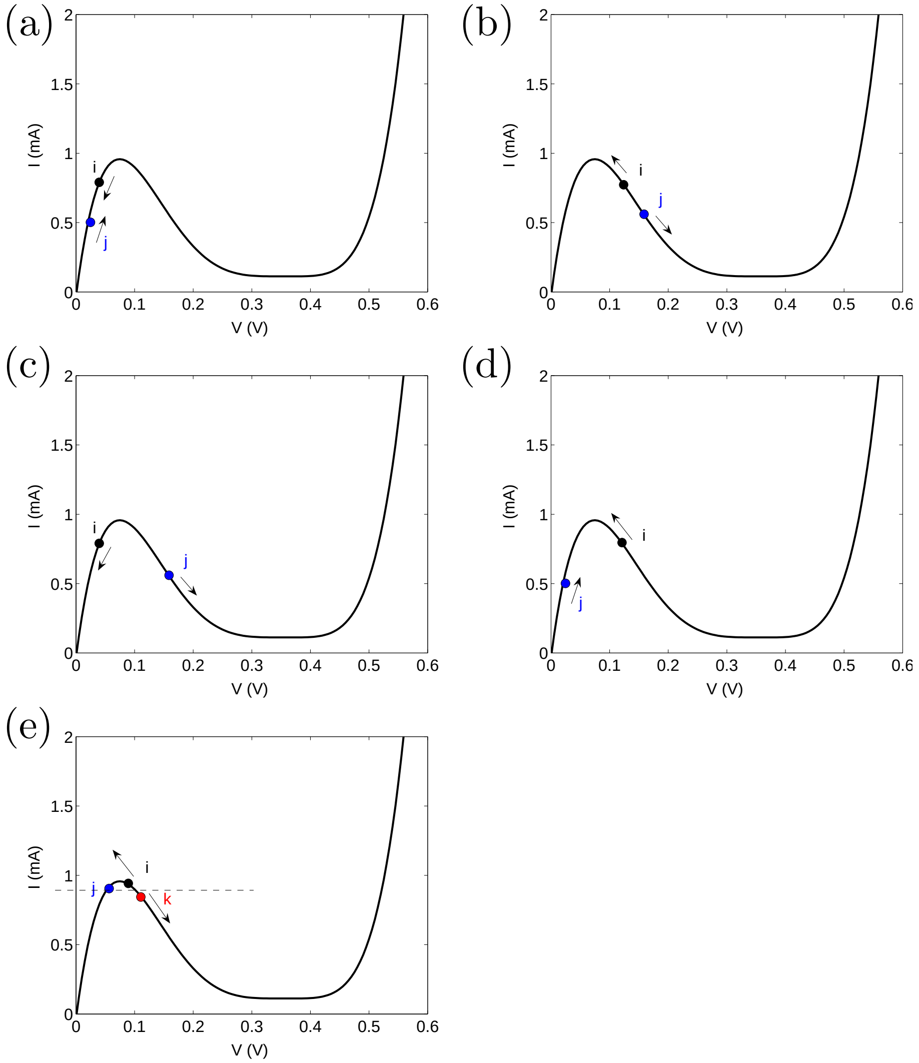

FIGURE 7.6: Coupling mechanism of the tunnel diode circuit model

7.3 Results

7.3.1 Current branches

If all the elements are identical, that is, no variance in capacitances and no variance in intrinsic $I-V$ characteristics, the simulated $I-V$ curve for the TD circuit will be a single curve with the same shape as a single tunnel diode under ramping condition, no current branches observed. While this seems numerically stable, we have not yet calculated stability analytically. When variance in capacitances is introduced into the model, $C_i = C_0 + \delta C \times r_i, i = 1, 2, ..., N,$, where δC is the relative maximum value of the fluctuation, r_i's are independent random numbers evenly distributed in [0,1], we began to see current branches. Fig. 7.7 is simulation of $I - V$ curves with current branches for $\delta C = 0.01$. We will mostly focus on upramping, steady increase in applied voltage. Figures 7.8 show voltage across each diodes changing with time. We also found that the voltage across the diode with smallest capacitance (5.6 nF) goes up to the higher branch of the $I - V$ characteristic first. So we can order the capacitance to imitate a field domain configuration as occurs in superlattices. $C_i = C_0 - \delta C i/10, i = 1, 2, ..., N,$.

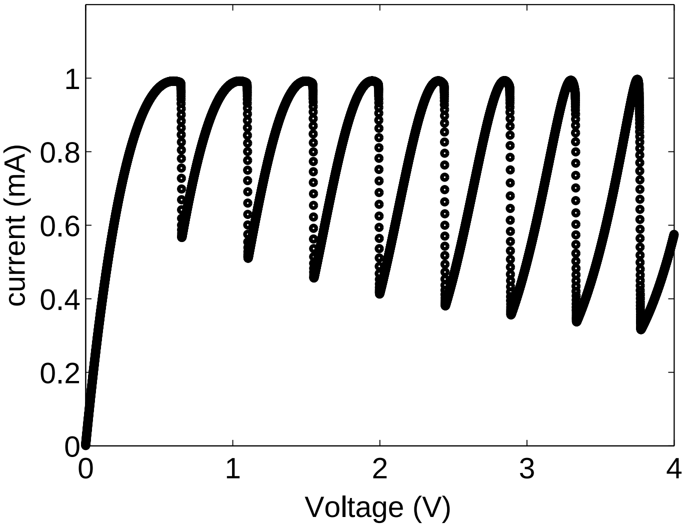

FIGURE 7.7: $I - V$ curve of eight tunnel diode model with variance in capacitances: $\delta C = 0.01$

Another way to have current branches is to introduce fluctuation to $I - V$ characteristics.

$$J_i = J_0(1 + dJ \times \epsilon_i), \tag{7.5}$$

where ϵ_i's are N independent standard normally distributed random numbers and $dJ = 0.1$, which is a typical value for real diodes. And the imitation of field domain by ordering capacitors is destroyed and voltages become disordered again when the variance in I-V is introduced. So it seems that I-V variance has a more significant effect than a 1% variance in the 5.6nF capacitances.

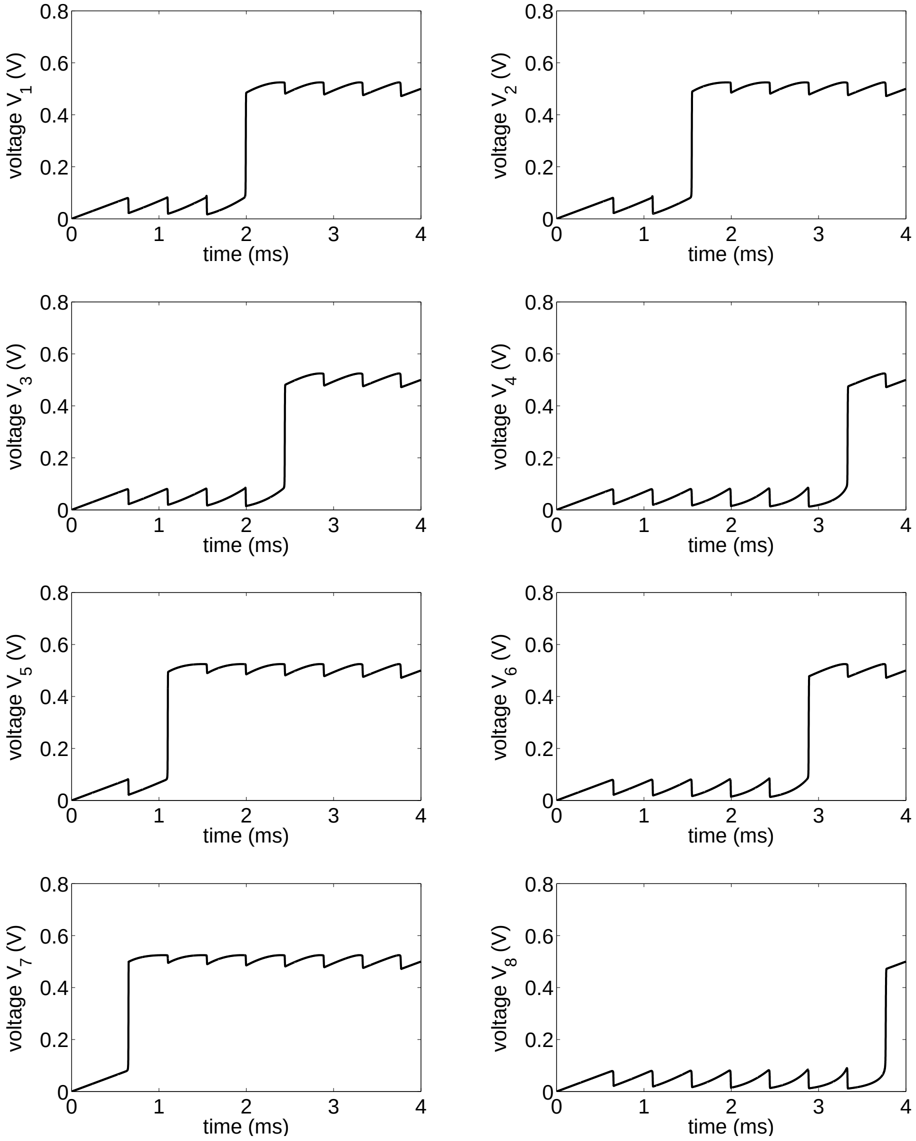

FIGURE 7.8: Voltage evolution of each element in the eight tunnel diode model with variance in capacitances: $\delta C = 0.01$

7.3.2 Field inhomogeneity parameter

In analogy with studies of the synchronization properties of the Kuramoto model, it is possible to define a parameter which is analogous to the synchronization order parameter.[109] If the coupling term in Eq. (7.3) is neglected, one finds an *uncoupled* state in which the element voltages increase independently. Starting from the initial condition $v_i^{(0)}(0) = 0$ for all i, typical for experimental systems [33, 110, 111], the voltage of each element is given by $v_i^{(0)} = V \times C_{tot}/C_i$. Since the C_i have a small dispersion, the uncoupled state is associated with a field profile that is nearly uniform. When the coupling term is nonzero, the system deviates from the uncoupled state and the field profile becomes non-uniform. This behavior is usefully characterized by introducing a *field inhomogeneity parameter* r_{max} defined by:

$$r_{max} = \max\{r(t) : 0 < t < T\}, \tag{7.6}$$

where

$$r(t) = \frac{1}{N}\sum_{j=1}^{N}\left(\frac{v_j - v_j^{(0)}}{v_j^{(0)}}\right)^2. \tag{7.7}$$

The quantity $r(t)$ expresses the time-dependent level of field nonuniformity in the system for ramp time T, while r_{max} gives the maximal degree of nonuniformity during the entire ramping process and associates a single value to the entire process. For the uncoupled state, r_{max} tends to zero; however, when the effect of the coupling term is large, r_{max} assumes a value of order 1.

If the total voltage is held constant, the system always relaxes to a state exhibiting current coherence. This corresponds to a stable fixed point of the system with $\dot{V} = 0$. If the average applied voltage, V/N, falls in the NDR region of the single element $I - V$ curve, there are *multiple* fixed points corresponding to distinct arrangements of individual element voltages. For a completely homogeneous system, such that all elements are *identical*, i.e., $C_i = C$ and $I_i(v) = I_0(v)$ for all i, these fixed points are highly degenerate corresponding to the same overall device current [112]. When the homogeneous system is subjected to a ramped voltage, starting from the initial state $v_i(t = 0) = 0$ for all i, the element voltages remain identical throughout the ramp process, i.e., $v_i(t) = V(t)/N$, and the overall $I - V$ curve has a similar shape to that of a single element. The use of *non-uniform* initial conditions is equivalent to the introduction of heterogeneity to the system.

When heterogeneity is introduced into the system current branches emerge in the static limit as shown in the $I-V$ curve of Fig. 7.9a. The variance in the element $I-V$ characteristics is expressed as $I_i(v_i) = I_0(v_i)(1 + \epsilon_i)$, where the ϵ_i's are independent and identically distributed (i.i.d.) random numbers, distributed normally with mean zero and standard deviation σ_I, i.e., $\sigma_I^2 \equiv \frac{1}{N} \sum_{i=1}^{N} \epsilon_i^2$. We use a Gaussian distribution on [-1,1] and have found that the coherence behavior is not sensitive to the detailed form of distribution. We have also explored the effect of capacitance variation and variation due to electrical noise in individual elements, and find that the qualitative behavior is the same as that observed when the only variance is in the element $I - V$ curves.

When the ramp time T is *large*, the system exhibits well-defined current branches in the static $I - V$ curves, shown in Fig. 7.9a for $N = 8$. As the total voltage ramps higher, the elements jump rapidly from Region I to III one by one, and the parameter r_{max} takes a value of order 1, indicative of a highly non-uniform distribution of element voltages. Figure 7.9b shows the corresponding contour plot in which the current level is plotted in gray scale vs. element number i and total voltage V. The presence of current coherence is shown by the clear horizontal bands, indicating that, for all parts of the ramping process, the individual device currents are identical. The degree of this coherence is determined by the relative strength of coupling term in Eq. (7.3). While there is a structural similarity between Eq. (7.3) and the Kuramoto

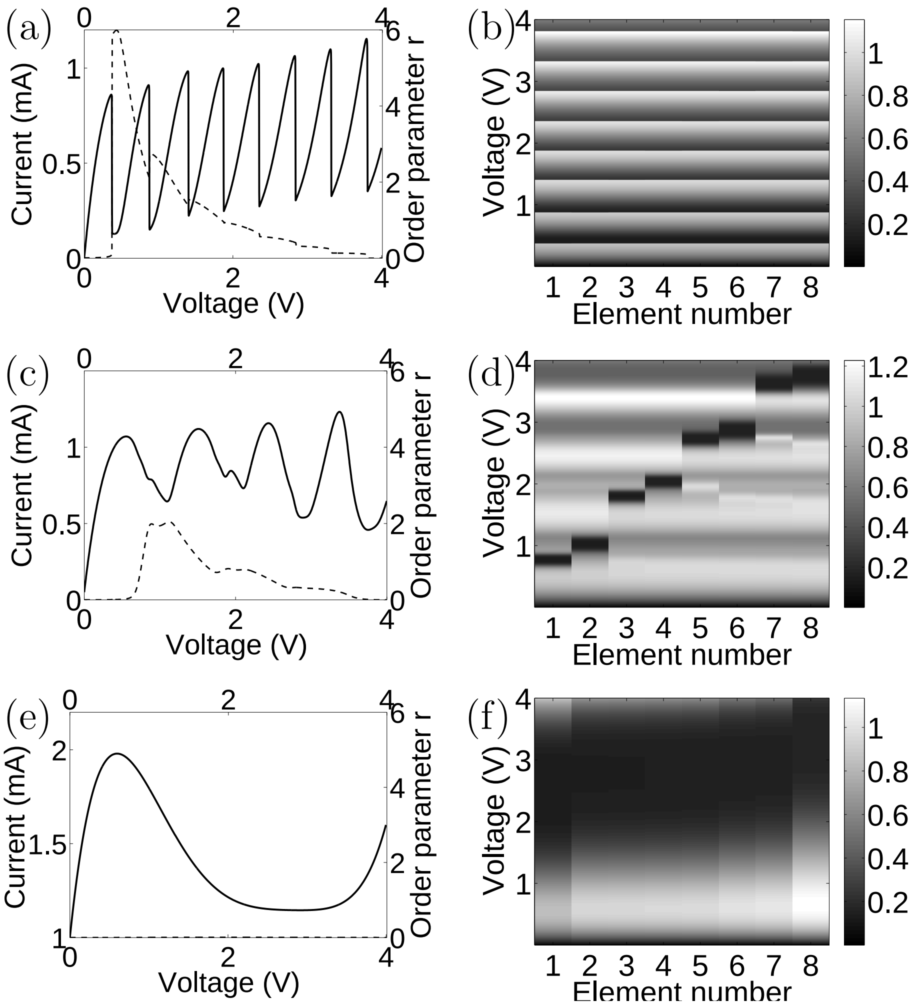

FIGURE 7.9: Current-voltage ($I-V$) curves and coherence contour plots for different ramp times, all with $N = 8$, $C = 200$ nF and $\sigma_I = 0.1$. (a) Fully coherent case: $I - V$ curve with ramp time $T = 500$ ms. Dashed curve shows the parameter $r(t)$. (b) Coherence contour plot for $T = 500$ ms (gray scale in units mA). (c) $I-V$ curve for the partially coherent case with $T = 2$ ms. (d) Coherence contour plot for $T = 2$ ms. (e) $I-V$ curve for the incoherent case with $T = 0.1$ ms. (f) Coherence contour plot for $T = 0.1$ ms.

oscillator model, it should be noted that the circuit model presented here does *not* describe temporal synchronization in the currents $I_j(t)$.

As the ramp time decreases, the elements show only partial coherence, see Fig. 7.9c. In this case, more than one element can jump to Region III at the same time.

The field distribution deviates less from the uniform state, the current branches are rounded and smaller in number and amplitude, and the abrupt jumps between current branches disappear. A similar rounding of experimental current branches versus ramping rate has been reported in weakly-coupled GaAs/AlAs semiconductor superlattices [46]. The r_{max} value also decreases from its large T value. Figure 7.9d shows the corresponding contour plot in which the presence of partial coherence is indicated by a background of horizontal bands, interrupted by localized dark areas that correspond to the passage of individual or pairs of elements through Region II.

For fast ramping, the elements do not cohere and they pass through the NDR region simultaneously (Fig. 7.9e). The r_{max} parameter approaches zero, implying that the system behavior is very close to the uncoupled state. The $I - V$ curve of the full array follows closely that of an individual element, $I_0(v)$. The contour plot, Fig. 7.9f, shows smooth behavior and horizontal features are absent. We have also considered ramping from different initial states as well as more elaborate circuit array models - e.g., including small series inductance and parallel capacitance with each nonlinear element - and find a similar overall behavior as reported above.

Plotting the value of r_{max} versus ramp time T for several different N values in Fig. 7.9a indicates that the transition from uncoupled to coherent behavior is a smooth transition with an onset that is *independent* of system size N. For large ramp time, r_{max} approaches an asymptotic value that is N-dependent. As $N \rightarrow \infty$, $r_{max} \rightarrow 2.85$, a value that depends only on the single element function $I_0(v)$. For the parameters used here, the transition from uncoupled to coherent behavior occurs as the ramp time increases from ~ 100 μs to ~ 10 ms, a timescale range that is significantly greater than the zero-bias characteristic RC time constant associated with an individual element, i.e., $\tau = CdI_0/dv\ |_{v=0} \simeq 2\ \mu$s.

To better understand this behavior, we investigate the effect of perturbations

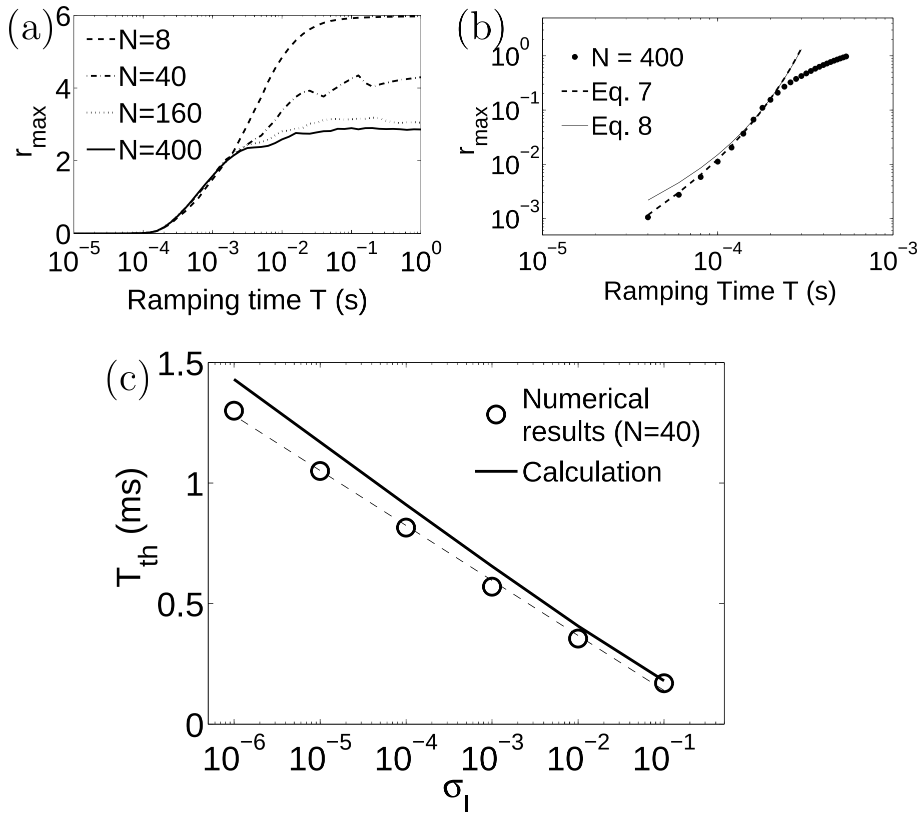

FIGURE 7.10: (a) The parameter r_{max} versus ramp time T for indicated values of N. Each curve is an average of ten different statistical configurations of the $I_i(v_i)$ curves with $C = 200$ nF and $\sigma_I = 0.1$. (b) Closed circles give r_{max} vs. T near the *characteristic* value for $N = 400$. The solid curve is a first-order calculation using Eqs. (7.6) and (7.15), while the dashed curve is based on Eq. (7.16). (c) T_{th} versus σ_I, comparing analytical prediction with simulation for $N = 40$.

about the uncoupled state of the form

$$v_i = v_i^{(0)} + \delta v_i \equiv v + \delta v_i, \tag{7.8}$$

where $v_i^{(0)}(t) = \alpha t$ denotes the uncoupled state solution. Substituting this form into the dynamical model, Eq. (7.3), to leading order we can write:

$$\dot{\delta v_i} = \frac{1}{Nc}\{I_0(\alpha t)\sum_{j=1}^{N}(\epsilon_j - \epsilon_i) + I_0'(\alpha t)\sum_{j=1}^{N}(\delta v_j - \delta v_i) + I_0'(\alpha t)\sum_{j=1}^{N}[\epsilon_j\delta v_j - \epsilon_i\delta v_i]\}. \tag{7.9}$$

Note that the third term is higher order.

For extremely fast ramping (α very large), δv_i is very small, so the second term can be neglected. Using $\sum_{j=1}^{N} \epsilon_j = 0$ and the voltage constraint $\sum_{j=1}^{N} \delta v_j = 0$, we write

$$\dot{\delta v_i} = -\frac{\epsilon_i}{c} I_0(\alpha t). \tag{7.10}$$

Integrating this equation, we have

$$\delta v_i(t) = -\frac{\epsilon_i}{c} \int_0^t I_0(\alpha t')dt' = -\frac{\epsilon_i}{c\,\alpha} \int_0^v I_0(v')dv' \equiv -\frac{\epsilon_i}{c\,\alpha} P(v). \tag{7.11}$$

According to the definition of order parameter,

$$r(v) = \frac{1}{N} \sum_{i=1}^{N} \frac{(\delta v_i)^2}{(v_i^{(0)})^2} = \left(\frac{1}{N} \sum_{i=1}^{N} \epsilon_i^2 \right) \left(\frac{P(v)}{c\,\alpha\,v} \right)^2 = \left(\frac{\sigma_I P(v)}{c\,V_{max}\,v} \right)^2 T^2. \tag{7.12}$$

So

$$r_{max} = \frac{\sigma_I^2 T^2}{c^2 V_{max}^2} \max(P(v)/v)^2. \tag{7.13}$$

Eq. 7.13 shows that r_{max} scales as T^2 for small values of T.

For somewhat smaller α (i.e., larger ramping time T) the second term of Eq. 7.9 cannot be neglected and we write

$$\dot{\delta v_i} = -\frac{I_0(\alpha t)}{c}\epsilon_i - \frac{I_0'(\alpha t)}{c}\delta v_i. \tag{7.14}$$

This equation can be solved explicitly as

$$\delta v_i = -\frac{\epsilon_i}{C\alpha}\, \mathrm{e}^{-\frac{I_0(v)}{C\alpha}} \int_0^v I_0(v')\, \mathrm{e}^{\frac{I_0(v')}{C\,\alpha}} dv', \tag{7.15}$$

with the initial conditions $\delta v_i(0) = 0$ for all i.

For large values of α, the two exponentials in Eq. (7.15) are approximated by unity, and it immediately follows that $r_{max} \propto T^2$ where the coefficient of proportionality is independent of N; this is confirmed in Fig. 7.10a. For somewhat smaller α values and provided the local maximum of the element $I-V$ curve is sufficiently sharp, Eq. (7.15) can be evaluated using a saddle point method to write $\delta v_i \approx \frac{\epsilon_i I_M \sqrt{\pi}}{\sqrt{\beta c \alpha}} \mathrm{e}^{\frac{I_M - I_0(v)}{C\alpha}}$, where $\beta = -\frac{I''(v)}{2} \mid_{v_M} > 0$. Inserting this result back into the definition of $r(t)$, cf. Eq. (7.6), gives $r(v) = \frac{\pi \sigma_I^2 I_M^2 T}{\beta C V_{max} v^2} \mathrm{e}^{\frac{2(I_M - I_0(v))}{C\alpha}}$. Noting that the exponential term takes a maximum value if we set $v = v_m$, so that $I_M - I_0(v) = I_M - I_m \equiv \Delta I$, where v_m and I_m are the voltage and current coordinates of the local *minimum* in the element $I-V$ characteristic, cf. Fig. 7.4b, we see that r takes its maximum value over the whole ramp process, so that

$$r_{max} = \frac{\pi \sigma_I^2 I_M^2 T}{\beta C V_{max} v_m^2} \mathrm{e}^{\frac{2\Delta I}{C\alpha}}. \tag{7.16}$$

Figure 7.10b plots the values of r_{max} calculated from both Eqs. (7.15) and (7.16) and compares them with the numerical results for $N = 400$, demonstrating that there is a range of ramp times (around 10^{-4} seconds) for which the asymptotic expression, Eq. (7.16) follows closely the transition to coherence behavior. In order to develop an analytic criterion for the onset of coherence behavior, we define a characteristic value of ramp time T_{th} lying in this range. Denoting the corresponding characteristic value of r_{max} by r_{th}, we have $\ln r_{th} = 2\ln \sigma_I + \ln\left(\frac{\pi I_M^2}{C\beta v_m^2}\right) - \ln\alpha + \frac{2\Delta I}{\alpha C}$. Solving for T_{th}, we can write

$$T_{th} = -\frac{C\,V_{max}}{\Delta I} \ln \sigma_I + K, \tag{7.17}$$

where $K = \frac{CV_{max}}{\Delta I}\left(\frac{1}{2}\ln\frac{r_{th}\beta C V_{max} v_m^2}{\pi I_M^2} - \frac{1}{2}\ln T_{th}\right)$ is slowly varying. Equation (7.17) shows explicitly the dependences of T_{th} on element heterogeneity (i.e., σ_I) as well as the single element NDR behavior. Interestingly, the pre-factor of the $\ln \sigma_I$ term, calculated to be $\frac{C\,V_{max}}{\Delta I} \simeq 1.18 \times 10^{-4}$ s, has the form of an RC time with an effective resistance that depends only on the total current drop in the NDR region, ΔI. Figure 7.10c plots T_{th} versus the variance level (with the specific choice $r_{th} = 0.1$)

and shows good agreement with numerical data for $N = 40$.

7.4 Connection between the weakly-coupled superlattice and the tunnel diode array

If we ignore the diffusion term in the superlattice model (see, for example, Eq. 2.29 from Chapter 2), we have the approximate tunneling equations:

$$J_{i\to i+1} = ev^{(f)}(F_i)n_i/l, \tag{7.18}$$

where l is the period of the superlattice so that the density n_i/l and the current J are three dimensional quantities. This approximation is valid for F_i of the order of the first resonant value or larger [33]. This approximate expression has been used in some previous work [113]. Meanwhile, the Poisson equation relates the charge density with the field values:

$$F_i - F_{i-1} = \frac{e}{\varepsilon}(n_i - N_D), \qquad i = 1, ..., N. \tag{7.19}$$

Inserting it into the Eq. 7.18 yields

$$\begin{aligned} J_{i\to i+1} &= \frac{v^{(f)}(F_i)}{l}[\epsilon(F_i - F_{i-1}) + eN_D] \\ &= \frac{eN_D v^{(f)}(F_i)}{l}\left[\frac{\epsilon}{eN_D}(F_i - F_{i-1}) + 1\right]. \end{aligned} \tag{7.20}$$

In this equation, we can see that the current depends on the fields in the present and the previous periods. Note that this coupling is inherently more complex than for the tunnel diode model, Eq. 7.3. It is this difference that explains, for example, why the superlattice exhibits formation of connected low- and high-field domains, whereas in the tunnel diode array such domain formation does not occur. Interestingly, we see that the superlattice model approaches the tunnel diode model when the quantum well doping level N_D is very large. In other words, the value of the field in the previous period is feed forward into the present one.

We have also used these insights to design an analog circuit using tunnel diodes that could be used to simulate the superlattice. This is shown in Fig. 7.11, which is the schematic of a possible circuit simulating the superlattice structure.

The box in Fig. 7.11 with input x and y and output $x \cdot y$ denotes a circuit element that takes in the voltages across the previous and the present elements and calculate the difference between them (e.g. using differential amplifier) and then multiply it with the voltage across the small resister r connected in series with the tunnel diode. This result is then used to generate a current of value $(v_i - v_{i-1}) \cdot I_i(v_i) \cdot r/R$ by the current source. Such a circuit element could be implemented by commercially available analog amplifier circuits or ADC processors (micro-controllers). The current is then feed back into the circuit. So the current through each period is

$$\mathcal{I}_i = (1 + (v_i - v_{i-1}) \cdot r/R) \cdot I_i(v_i) \tag{7.21}$$

Comparing this equation with Eq. 7.20, one immediately sees that by tuning the resister R, the coefficient r/R can simulate the effect of doping density ϵ/eN_D in Eq. 7.20.

The first resister serves as the ohmic boundary condition in the superlattice.

$$\mathcal{I}_1 = \frac{v_1}{R_c} \tag{7.22}$$

The collector boundary probably is not necessary because it does not play a key role in the superlattice model. If needed, it can be implemented as

$$J_{N\to N+1} = \sigma F_N \left[\frac{\epsilon}{eN_D}(F_N - F_{N-1}) + 1 \right]. \tag{7.23}$$

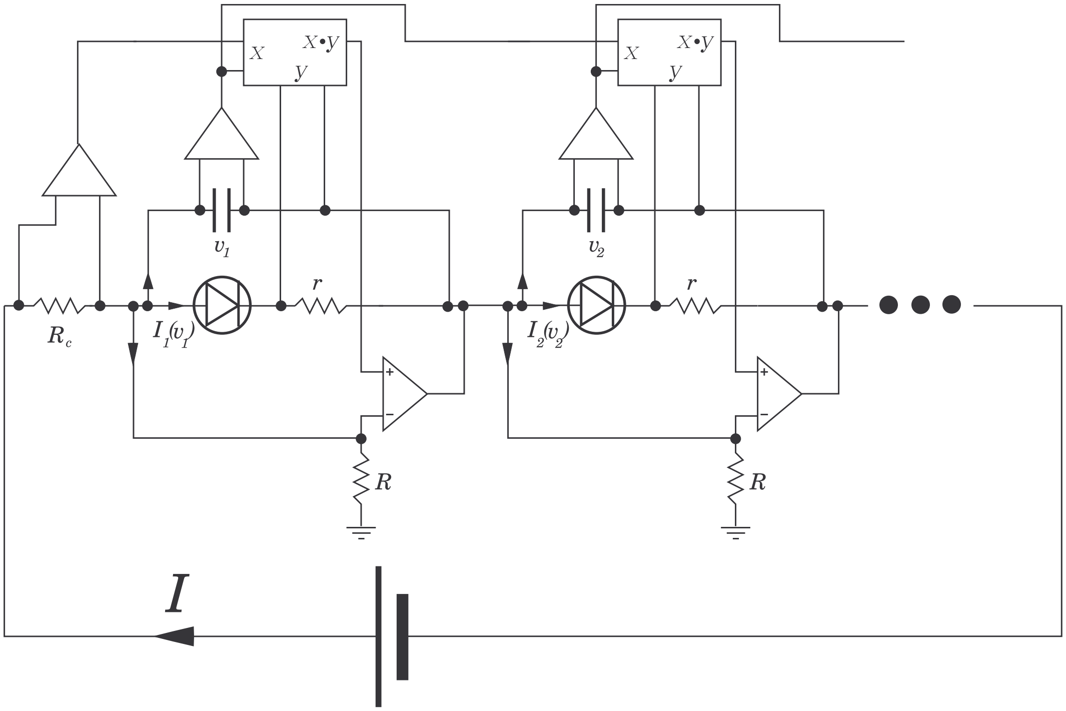

FIGURE 7.11: Circuit schematic of a circuit based on tunnel diodes to simulate the superlattice.

7.5 Conclusion

We have shown that negative differential resistance and element heterogeneity are key sources for the observation of non-uniform field distributions and multiple current branches in the electrical conduction properties of a series array of nonlinear circuit elements. Specifically, we have shown how the system approaches a state of full current coherence as the element variance level and voltage ramp rate are varied. Generally, this globally-coupled model provides a particularly simple example of how element heterogeneity can *enhance* collective behavior in a complex system. The numerical and analytical results that can be obtained from this model may provide useful insight for understanding similar self-organizing behaviors that are found for a range of more complex electronic systems, for example, semiconductor superlattices and quantum cascade laser structures [33, 110, 15]. In practical devices it is often desirable to have an electric field configuration that is as uniform as possible. The model introduced here may be useful in developing new control strategies for stabilizing such configurations.

8

Summary

As we have seen in this thesis, negative differential conductivity (NDC) gives rise to rich dynamics in spatially extended systems. It causes spatio-temporal charge instability in an electronic transport system driven far from equilibrium. A host of interesting phenomena emerge, such as static field domains, moving fronts and bistability. From a scientific perspective, studying these systems enriches our knowledge of the behavior of in far-from-equilibrium systems, a major puzzle that needs to be solved and is relevant to many natural and social phenomena. From a technological perspective, the semiconductor superlattice is the foundation of many devices such as multi-quantum well photodecters and the quantum cascade laser and itself is proposed to generate THz emission. Understanding the effect of NDC will help us in building successful advanced devices.

Different mechanisms can cause NDC. We have focused here on the discrete model of the sequential resonant tunneling in the weakly-coupled superlattice and the continuum model on the miniband transport in the strongly-coupled superlattice. Moreover, we have gone beyond these well-established models and investigated shunted structures in this thesis.

In Chapter 3, we study the effect of the contact on the weakly-coupled superlattice along the vertical direction. The contact controls the amount of electrons injected into the system, thus playing a similar role as the doping level. Moreover, different transient responses are found with different contact conductivity and voltage steps. In order to suppress the spatio-temporal charge instability, we add a parallel shunt to the weakly-coupled superlattice in Chapter 4. Accordingly, the lateral direction is incorporated into the system. The results show that the shunt can stabilize a uniform field biased in the NDC region in the superlattice with relatively small lateral size and high quality connection between the shunt and the superlattice. However, as either the lateral size becomes larger or the connection quality deteriorates, the system loses stability and different types of bifurcation are found between different behaviors of the system. After the role of the shunt is confirmed, we move on to study if the shunt can work for a strongly-coupled superlattice which may serve as a THz gain medium in Chapter. 5. Taking into consideration of devices, more realistic parameters of the materials are used. Simulation results show that the shunt can stabilize the high field in NDC with gain in THz range. However, in this case, a much narrower superlattice is allowed and the device is best operated at room-temperature to achieve sufficient diffusion in the lateral direction. Of course, room temperature operation is a big advantage for practical devices.

In Chapter. 6, we switch to a different topic, the behavior of stochastic switching between bistable static states caused by NDC in the weakly-coupled superlattices. A stochastic differential equation system incorporating shot noise is numerically integrated. The stochastic switching from a metastable state to a globally stable state is successfully simulated and the mean switching time is fit to $\exp(|V - V_{th}|^{\alpha})$ and α is unlikely to be 1.5 which is predicted for a one-dimensional system. Another key subject, the switching path, is also studied using a linear decomposition method at the metastable state, leading to an effective potential. Principal component analysis suggests a most probable path for part of trajectories beyond the saddle point.

In Chapter. 7, we have studied another system, a circuit of tunnel diodes connected in series. We find that although the $I-V$ curve shows similar current branches due to NDC of each tunnel diode as those in the superlattice, field domains do not form due to the lack of next neighbor coupling in the superlattice system. Ramping of the total applied voltage can significantly change the shape of the $I-V$ curve and the evolution of the voltage across each diode element.

Up until now, we have studied a broad range of topics related to NDC in spatially extended systems. Here we list a few questions and possibilities for future research:

We used a simple ohmic contact as the boundary condition. Although we used a 3D Fermi gas model at the injecting contact to calculated equivalent contact conductivity, how can we use a more microscopically detailed model that can include, for example, band bending to describe the contact? How can we design the contact to have either similar or substantially different behavior? How might different types of contacts than those assumed here, affect predictions on the dynamics of relocation or stability properties of the spatially-uniform electric field state?

In the shunt models, we assumed that the connection between the shunt and the superlattice can have high quality. While this can likely be achieved by a sophisticated in-situ growth technique such as cleaved edge overgrowth, it would interesting to study other common technique such as evaporation of a thin metallic layer as shunt. In the latter case, one wants to understand how does the geometry at the interface between the shunt and the quantum well affect the electron states and, thus, the connection? Of course, the shunt model we proposed here is still in an early stage, and significant research has to be done down the road in order to realize practical devices.

In the stochastic work, we assumed lateral uniformity of the charge density in each SL quantum well. However, what happens when the size becomes large enough such that this is no longer true guaranteed, i.e., when the lateral size is much greater than the in-plane mean free path. While such a scenario has been considered for single quantum well structures by Tretiakov et al., the extension to the SL is a challenging and open question. Questions to consider in a study of the role of lateral dynamics include correlation of noises between different positions in the same well and multiple timescales.

Bibliography

[1] M. Cross and H. Greenside. *Pattern Formation and Dynamics in Nonequilibrium Systems.* Cambridge University Press, Cambridge, 2009.

[2] S. Jakubith, H. H. Rotermund, W. Engel, A. von Oertzen, and G. Ertl. Spatiotemporal concentration patterns in a surface reaction: Propagating and standing waves, rotating spirals, and turbulence. *Phys. Rev. Lett.*, 65:3013, 1990.

[3] K. L. Thompson, K. M. S. Bajaj, and G. Ahlers. Traveling concentric-roll patterns in Rayleigh-Bénard convection with modulated rotation. *Phys. Rev. E*, 65:046218, 2002.

[4] A. G. Merzhanov and E. N. Rumanov. Physics of reaction waves. *Rev. Mod. Phys.*, 71:1173, 1999.

[5] G. Falkovich, K. Gawedzki, and M. Vergassola. Particles and fields in fluid turbulence. *Rev. Mod. Phys.*, 73:913, 2001.

[6] E. M. Izhikevich. *Dynamical Systems in Neuroscience: The Geometry of Excitability and Bursting.* MIT Press, 2009.

[7] J. von Hardenberg, E. Meron, M. Shachak, and Y. Zarmi. Diversity of vegetation patterns and desertification. *Phys. Rev. Lett.*, 87:198101, 2001.

[8] P. Bak, C. Tang, and K. Wiesenfeld. Self-organized criticality: An explanation of the 1/f noise. *Phys. Rev. Lett.*, 59:381, 1987.

[9] S. Boccaletti, J. Kurths, G. Osipov, D. L. Valladares, and C. S. Zhou. The synchronization of chaotic systems. *Physics Reports*, 366:1, 2002.

[10] A. Pikovsky, M. Rosenblum, and J. Kurths. *Synchronization: a universial concept in nonlinear sciences.* Cambridge University Press, Cambridge, 2001.

[11] S. Boccaletti, V. Latora, Y. Moreno, M. Chavez, and D.-U. Hwang. Complex networks: Structure and dynamics. *Physics Reports*, 424:175, 2006.

[12] J. H. Miller and S. E. Page. *Complex adaptive systems: an introduction to computational models of social life.* Princeton University Press, Princeton, 2007.

[13] D. J. Watts and S. H. Strogatz. Collective dynamics of 'small-world' networks. *Nature*, 393:440, 1998.

[14] A. Barabasi and R. Albert. Emergence of scaling in random networks. *Science*, 286:509, 1999.

[15] E. Scholl. *Nonlinear spatio-temporal dynamics and chaos in semiconductors.* Cambridge University Press, Cambridge, 2001.

[16] A. Wacker and E. Scholl. Oscillatory instability in the heterostructure hot-electron diode. *Appl. Phys. Lett.*, 59:1702, 1991.

[17] V. J. Goldman, D. C. Tsui, and J. E. Cunningham. Observation of intrinsic bistability in resonant-tunneling structure. *Phys. Rev. Lett.*, 58:1236, 1987.

[18] L. Esaki. New phenomenon in narrow germanium p-n junctions. *Phys. Rev.*, 109:603, 1958.

[19] C. R. Wallis and S. W. Teitsworth. Hopf bifurcations and hysteresis in resonant tunneling diode circuits. *J. Appl. Phys.*, 76:4443, 1994.

[20] B. G. Streetman and S. K. Banerjee. *Solid State Electronic Devices.* Prentice Hall, Cambridge, 6th edition, 2005.

[21] J. B. Gunn. Microwave oscillation of current in III-V semiconductors. *Solid State Commun.*, 1:88, 1963.

[22] M. E. Levinshtein and M. S. Shur. The Gunn effect (review). *Soviet Physics - Semiconductors*, 5:9, 1972.

[23] L. Esaki and R. Tsu. Superlattice and negative differential conductivity in semiconductors. *IBM J. Res. Develop*, 14:61, 1970.

[24] E. Schomburg, K. Hofbeck, J. Grenzer, T. Blomeier, A. A. Ignatov, K. F. Renk, D. G. Pavel'ev, Yu. Koschurinov, V. Ustinov, A. Zhukov, S. Ivanov, and P. S. Kop'ev. Millimeter wave oscillator based on a quasiplanar superlattice electronic device. *Appl. Phys. Lett.*, 71:401, 1997.

[25] T. A. Fulton and L. N. Dunkleberger. Lifetime of zero-voltage state in Josephson tunnel juntions. *Phys. Rev. B*, 9:4760, 1974.

[26] H. B. Chan, M. I. Dykman, and C. Stambaugh. Paths of fluctuation induced switching. *Phys. Rev. Lett.*, 100:130602, 2008.

[27] P. Mehta, R. Mukhopadhyay, and N. S. Wingreen. Exponential sensitivity of noise-driven switching in genetic networks. *Phys. Biol.*, 5:026005, 2008.

[28] W. K. den Otter. Thermodynamic integration of the free energy along a reaction coordinate in cartesina coordinates. *J. Chem. Phys.*, 112:7283, 2000.

[29] R. B. Best and G. Hummer. Reaction coordinates and rates from transition paths. *PNAS*, 102:6732, 2005.

[30] C. W. Gardiner. *Handbook of Stochastic Methods*. Springer, New York, 1985.

[31] D. Wales. *Energy Landscapes*. Cambridge Univeristy Press, New York, 2004.

[32] A. Wacker. Semiconductor superlattices: a model system for nonlinear transport. *Phys. Rep.*, 357:1, 2002.

[33] L. L. Bonilla and H. T. Grahn. Non-linear dynamics of semiconductor superlattices. *Rep. Prog. Phys*, 68:577, 2005.

[34] M. D. Ventra. *Electrical transport in nanoscale systems*. Cambridge University Press, Cambridge, 2008.

[35] G. D. Mahan. *Many-Particle Physics*. Plenum Press, New York, 1990.

[36] L. L. Bonilla and S. W. Teitsworth. *Nonlinear wave methods for charge transport*. Wiley, 2010.

[37] J. H. Davies. *The Physics of Low-dimensional Semiconductors: An Introduction*. Cambridge University Press, Cambridge, 1997.

[38] E. Schomburg, T. Blomeier, , K. Hofbeck, J. Grenzer, I. Lingott, A. A. Ignatov, K. F. Renk, D. G. Pavel'ev, Yu. Koschurinov, B. Ya. Melzer, V. Ustinov, S.V. Ivanov, A. Zhukov, and P. S. Kop'ev. Current oscillation in superlattices with different miniband widths. *Phys. Rev. B*, 58:4035, 1998.

[39] G. Platero and R. Aguado. Photon-assisted transport in semiconductor nanostructures. *Phys. Rep.*, 395:1, 2004.

[40] R. Aguado, G. Platero, M. Moscoso, and L. L. Bonilla. Microscopic model for sequential tunneling in semiconductor multiple quantum wells. *Phys. Rev. B*, 55:16053, 1997.

[41] M. Jonson. Quantum-mechanical resonant tunneling in the presence of a boson field. *Phys. Rev. B*, 39:5924, 1989.

[42] J. Bardeen. Tunneling from a many-particle point of view. *Phys. Rev. Lett.*, 6:57, 1961.

[43] L. L. Bonilla. Theory of nonlinear charge transport, wave propagation, and self-oscillations in semiconductor superlattices. *J. Phys.: Cond. Matter*, 14:R341, 2002.

[44] H. Xu and S. Teitsworth. Dependence of electric field domain relocation dynamics on contact conductivity in semiconductor superlattices. *Phys. Rev. B*, 76:235302, 2007.

[45] A. Amann, A. Wacker, L. L. Bonilla, and E. Schöll. Dynamic scenarios of multistable switching in semiconductor superlattices. *Phys. Rev. E*, 63:066207, 2001.

[46] M. Rogozia, S.W. Teitsworth, H.T. Grahn, and K.H. Ploog. Relocation dynamics of domain boundaries in semiconductor superlattices. *Phys. Rev. B*, 65:205303, 2002.

[47] L. L. Bonilla, R. Escobedo, and G. Dell'Acqua. Voltage switching and domain relocation in semiconductor superlattices. *Phys. Rev. B*, 73:115341, 2006.

[48] N. W. Ashcroft and N. D. Mermin. *Solid State Physics.* Brooks Cole, 1976.

[49] A. A. Ignatov and Yu. A. Romanov. Nonlinear electromagnetic properties of semiconductors with a superlattice. *phys. stat. sol. (b)*, 73:327, 1976.

[50] G. Brozak, M. Helm, F. DeRosa, C. H. Perry, M. Koza, R. Bhat, and Jr. S. J. Allen. Thermal saturation of band transport in a superlattice. *Phys. Rev. Lett.*, 64:3164, 1990.

[51] S. A. Ktitorov, G. S. Simin, and V. Y. Sindalovskii. Bragg reflections and the high-frequency conductivity of an electronic solid-state plasma. *Sov. Phys. Solid State*, 13:1872, 1972.

[52] J. R. Tucker. Quantum limited detection in tunnel junction mixers. *IEEE J. Quantum Electron.*, QE-15:1234, 1979.

[53] H. Willenberg, G. H. Dohler, and J. Faist. Intersubband gain in a bloch oscillator and quantum cascade laser. *Phys. Rev. B*, 67:085315, 2003.

[54] L. L. Bonilla, G. Platero, and D. Sánchez. Microscopic derivation of transport coefficients and boundary conditions in discrete drift-diffusion models of weakly coupled superlattices. *Phys. Rev. B*, 62:2786, 2000.

[55] M. Moscoso, J. Galán, and L. L. Bonilla. Bifurcation behavior of a superlattice model. *SIAM J. Appl. Math.*, 60:2029, 2000.

[56] M. Patra, G. Schwarz, and E. Schöll. Bifurcation analysis of stationary and oscillating domains in semiconductor superlattices with doping fluctuations. *Phys. Rev. B*, 57:1824, 1998.

[57] J. Hizanidis, A. Balanov, A. Amann, and E. Schöll. Noise-induced front motion: signature of a global bifurcation. *Phys. Rev. Lett.*, 96:244104, 2006.

[58] H. Schneider, C. Schönbein, R. Rehm, and P. Koidl. Domain pinning in GaAs/AlGaAs quantum well infrared photodetectors. *Appl. Phys. Lett.*, 88:051114, 2006.

[59] F. J. Higuera and L. L. Bonilla. Gunn instability in finite samples of GaAs ii. oscillatory states in long samples. *Physica D*, 57:161, 1992.

[60] H. Kroemer. Nonlinear space-charge domain dynamics in a semiconductor with negative differential mobility. *IEEE Trans. Electron Devices*, 13:27, 1966.

[61] Yuriy Bomze, Huidong Xu, Stephen W. Teitsworth, Rudolf Hey, and Holger T. Grahn. unpublished, 2009

[62] M. Rogozia, S.W. Teitsworth, H.T. Grahn, and K.H. Ploog. Statistics of the domain-boundary relocation time in semiconductor superlattices. *Phys. Rev. B*, 64:041308(R), 2001.

[63] L. L. Bonilla, O. Sánchez, and J. Soler. Nonlinear stochastic discrete drift-diffusion theory of charge fluctuations and domain relocation times in semiconductor superlattices. *Phys. Rev. B*, 65:195308, 2002.

[64] E.S. Daniel, B.K. Gilbert, J.S. Scott, and S.J. Allen. Simulations of electric field domain suppression in a superlattice oscillator device using a distributed circuit model. *IEEE Trans. Electron Devices*, 50:2434, 2003.

[65] E. Schöll. *Nonlinear spatio-temporal dynamics and chaos in semiconductors.* Cambridge University Press, Cambridge, 2001. Nonlinear Science Series, Vol. 10.

[66] A. Amann and E. Schöll. Coupled lateral and vertical electron dynamics in semiconductor superlattices. *Phys. Rev. B*, 72:165319, 2005.

[67] V. Cheianov, P. Rodin, and E. Schöll. Transverse coupling in bistable resonant-tunneling structures. *Phys. Rev. B*, 62:9966, 2000.

[68] L. Pfeiffer, K. W. West, H. L. Stormer, J. P. Eisenstein, K. W. Baldwin, and D. Gershoni. Formation of a high quality two-dimensional eletron gas on cleaved GaAs. *Appl. Phys. Lett.*, 56:1697, 1990.

[69] W. Wegscheider, L. Pfeiffer, and K. West. Current injection GaAs/AlGaAs quantum wire lasers fabricated by cleaved edge overgrowth. *Appl. Phys. Lett.*, 65:2510, 1994.

[70] K. J. Luo, H. T. Grahn, and K. H. Ploog. Relocation time of the domain boundary in weakly coupled GaAs/AlAs superlattices. *Phys. Rev. B*, 57:6838, 1998.

[71] A. Amann, A. Wacker, and E. Schöll. Tripole current oscillations in superlattices. *Physica B*, 314:404, 2002.

[72] A. Amann, J. Schlesner, A. Wacker, and E. Schöll. Chaotic front dynamics in semiconductor superlattices. *Phys. Rev. B*, 65:193313, 2002.

[73] J. Hizanidis, A. G. Balanov, A. Amann, and E. Schöll. Noise-induced oscillations and their control in semiconductor superlattices. *Int. J. Bifur. Chaos*, 16:1701, 2006.

[74] S. H. Strogatz. *Nonlinear Dynamics and Chaos: With Applications to Physics, Biology, Chemistry and Engineering.* Westview Press, New York, 2001.

[75] A. Amann and E. Schöll. Bifurcations in a system of interacting fronts. *J. Stat. Phys*, 119:1069, 2005.

[76] F. Bloch. Über die quanten mechanik der elektronen in kristallgittern. *Z. Phys.*, 52:555, 1928.

[77] C. Zener. A theory of the electrical breakdown of solid dielectrics. *Proc. R. Soc. London, Ser A*, 145:523, 1934.

[78] K. W. Madison, M. C. Fischer, and M. G. Raizen. Observation of the wannier-stark fan and the fractional ladder in an accelerating optical lattice. *Phys. Rev. A*, 60:1767, 1999.

[79] J. Feldmann, K. Leo, J. Shah, D. A. B. Miller, and J. E. Cunningham. Optical investigation of bloch oscillations in a semiconductor superlattice. *Phys. Rev. B*, 46:7252, 1992.

[80] E. E. Mendez, F. Agulló-Rueda, and J. M. Hong. Stark localization in GaAs-GaAlAs superlattices under an electric field. *Phys. Rev. Lett.*, 60:2426, 1988.

[81] T. Yajima and Y. Taira. Spatial optical parametric coupling of picosecond light pulses and transverse relaxation effect in resonant media. *J. Phy. Soc. Jpn.*, 47:1620, 1979.

[82] K. Leo, J. Shah, E. O. Göbel, T. C. Damen, S. Schmitt-Rink, W. Schäfer, and K. Köhler. Coherent oscillations of a wave packet in a semiconductor double-quantum-well structure. *Phys. Rev. Lett.*, 66:201, 1991.

[83] C. Waschke, H. G. Roskos, R. Schwedler, K. Leo, and H. Kurz. Coherent submillimeter-wave emission from bloch osicllations in a semiconductor superlattice. *Phys. Rev. Lett.*, 70:3319, 1993.

[84] R. Martini, G. Klose, H. G. Roskos, and H. Kurz. Superradiant emission from bloch oscillations in semiconductor superlattices. *Phys. Rev. B*, 54:14325, 1996.

[85] B. S. Williams, S. Kumar, Q. Hu, and J. L. Reno. *Opt. Express*, 13:3331, 2005.

[86] special issue thz-gap. *Phil. Trans. Roy. Soc. Lond. A., special issue THz-gap,*, 362:197, 2004.

[87] M. Lee and M. C. Wanke. Searching for a solid-state terahertz technology. *Science*, 316:64, 2007.

[88] T. Hyart, K. N. Alekseev, and E. V. Thuneberg. Bloch gain in dc-ac-driven semiconductor superlattices in the absence of electric domains. *Phys. Rev. B*, 77:165330, 2008.

[89] H. Kroemer. Large-amplitude oscillation dynamics and domain suppression in a superlattice bloch oscillator. *arXiv:cond-mat/0009311*.

[90] T. Hyart, N. V. Alexeeva, J. Mattas, and K. N. Alekseev. Terahertz bloch oscillator with modulated bias. *arXiv:0812.4046*.

[91] T. Hyart, N. V. Alexeeva, A. Leppnen, and K. N. Alekseev. A theory of the electrical breakdown of solid dielectric. *Appl. Phys. Lett.*, 89:132105, 2006.

[92] T. Hyart, A. V. Shorokhov, and K. N. Alekseev. Theory of parametric amplification in superlattices. *Phys. Rev. Lett.*, 98:220404, 2007.

[93] P. G. Savvidis, B. Kolasa, G. Lee, and S. J. Allen. Resonant crossover of terahertz loss to the gain of a bloch oscillating InAs/AlSb superlattice. *Phys. Rev. Lett.*, 92:196802, 2004.

[94] M. Bao and K. L. Wang. Accurately measuring current-voltage characteristics of tunnel diodes. *IEEE Trans. Electron Devices*, 53:2564, 2006.

[95] J. T. Wallmark, L. Varettoni, and H. Ur. The tunnel resistor. *IEEE Trans. Electron Devices*, 10:215, 1963.

[96] T. Feil, H.-P. Tranitz, M. Reinwald, and W. Wegscheider. Electric-field stabilization in a high-density surface superlattice. *Appl. Phys. Lett.*, 87:212112, 2005.

[97] H. Xu, A. Amann, E. Schöll, and S. Teitsworth. Dynamics of electronic transport in a semiconductor superlattice with a shunting side layer. *Phys. Rev. B*, 79:245318, 2009.

[98] C. R. Bolognesi, H. Kroemer, and J. H. English. Well width dependence of electron transport in molecular-beam epitaxially grown InAs/AlSb quantum wells. *J. Vac. Sci. Technol. B*, 10:877, 1992.

[99] K. Ohtani and H. Ohno. InAs/AlSb quantum-cascade lasers operating at 10 um. *Appl. Phys. Lett.*, 82:1003, 2003.

[100] C. H. Möller, O. Kronenwerth, D. Grundler, W. Hansen, Ch. Heyn, and D. Heitmann. Extraordinary magnetoresistance effect in a microstructured metal-semiconductor hybrid structure. *Appl. Phys. Lett.*, 80:3988, 2002.

[101] A. A. Ignatov, E. Schomburg, J. Grenzer, S. Winnerl, and K. F. Renk. Theory of electron transport in a THz-field irradiated semicondutctor superlattice: occurrence of quantized dc voltages and current reponsivity. *Superlattices Microstruct.*, 22:15, 1997.

[102] H. Kroemer. The 6.1 Å family (InAs, GaSb, AlSb) and its heterostructures: a selective review. *Physica E*, 20:196, 2004.

[103] Y. A. Kuznetsov. *Elements of Applied Bifurcation Theory*. Springer, New York, 2004.

[104] G. Vasilescu. *Electronic Noise and Interfering Signals: Principles and Applications*. Springer, New York, 2005.

[105] A. Greiner, W. Strittmatter, and J. Honerkamp. Numerical integration of stochastic differential equations. *J. Stat. Phys.*, 51:95, 1988.

[106] J. E. Jackson. *A User's Guide to Principal components*. Wiley-Interscience, New York, 1991.

[107] F. Sagués, J. M. Sancho, and J. García-Ojalvo. Spatiotemporal order out of noise. *Rev. Mod. Phys.*, 79:829, 2007.

[108] Y. Braiman, J. F. Lindner, and W. L. Ditto. Taming spatiotemporal chaos with disorder. *Nature*, 378:465, 1995.

[109] J. A. Acebron, L. L. Bonilla, C. J. P. Vicente, F. Ritort, and R. Spigler. The kuramoto model: A simple paradigm for synchronization phenomena. *Rev. Mod. Phys.*, 77:137, 2005.

[110] S. L. Lu, L. Schrottke, S. W. Teitsworth, R. Hey, and H. T. Grahn. Formation of electric-field domains in GaAs/$\mathrm{Al}_x\mathrm{Ga}_{1-x}\mathrm{As}$ quantum cascade laser structures. *Phys. Rev. B*, 73:033311, 2006.

[111] W. Pan, S. K. Luo, J. L. Reno, J. A. Simmons, D. Li, and S. K. J. Brueck. Physics of reaction waves. *Appl. Phys. Lett.*, 92:052104, 2008.

[112] J. C. Neu. private communication.

[113] L. L. Bonilla, J. Galán, J. A. Cuesta, F. C. Martínez, and J. M. Molera. Dynamics of electric-field domains and oscillations of the photocurrent in a simple superlattice model. *Phys. Rev. B*, 50:8644, 1994.

[114] S. Kumar, B. S. Williams, S. Kohen, and Q. Hu. Continuous-wave operation of terahertz quantum-cascade lasers above liquid-nitrogen temperature. *Appl. Phys. Lett.*, 84:2494, 2004.

[115] O. A. Tretiakov, T. Gramespacher, and K. A. Matveev. Lifetime of metastable states in resonant tunneling structures. *Phys. Rev. B*, 67:073303, 2003.

Biography

Name:	Huidong Xu
Date of Birth:	September 24, 1982
Place of Birth:	Shanghai, China
Education:	Duke University (2004-2010) PhD in physics, May, 2010 MS in statistics, December, 2009
	Fudan University (2000-2004) BS in physics, June, 2004

Publications:

- Huidong Xu, Stephen W. Teitsworth, *On the possibility of a shunt-stabilized superlattice THz emitter*, Appl. Phys. Lett., **96**, 022101 (2010) .
- Huidong Xu, Andreas Amann, Eckehard Schöll, Stephen W. Teitsworth, *Electronic dynamics in a semiconductor superlattice with a shunting side layer*, Phys. Rev. B, **79**, 245318 (2009).
- Huidong Xu, Stephen W. Teitsworth, *Dependence of electric field domain relocation dynamics on contact conductivity in semiconductor superlattices*, Phys. Rev. B, **76**, 235302 (2007).

Publications in preparation:

- Huidong Xu, Stephen W. Teitsworth, Scott C. Schmidler, *Scaling of lifetime of metastable states in superlattices*, in preparation.

Conference talks:

- Huidong Xu, Scott C. Schmidler, Stephen W. Teitsworth, *Scaling behavior of stochastically varying current switching times in semiconductor superlattices*, March 2010, APS March Meeting.
- Yuriy Bomze, Huidong Xu, Stephen W. Teitsworth, Rudolf Hey, Holger T. Grahn, *Measurement of stochastic current switching in semiconductor superlattices*, March 2010, APS March Meeting.
- Huidong Xu, Stephen W. Teitsworth, *Suppression of electric field domains in semiconductor superlattices with side shunting layer*, March 2009, APS March Meeting.
- Stephen W. Teitsworth, Huidong Xu *Stochastic current switching behavior in semiconductor superlattices*, March 2009, APS March Meeting.
- Kevin J. Brown, Huidong Xu, Stephen W. Teitsworth, *Bifurcations and Averaging in a Series Array of Tunnel Diodes*, 75th Annual Meeting of the APS Southeastern Section.
- Huidong Xu, Stephen W. Teitsworth, *Synchronization behavior in linear arrays of negative differential resistance circuit elements*, March 2008, APS March Meeting.
- Huidong Xu, Stephen W. Teitsworth, *Dependence of electric field domain relocation dynamics on contact conductivity in semiconductor superlattices*, March 2007, APS March Meeting.
- Stephen W. Teitsworth, Huidong Xu, *Dependence of current switching dynamics on contact conductivity in semiconductor superlattices*, March 2006, APS March Meeting.